HAL
open science

Investigation on the corrosion mechanisms of pure magnesium and the effect of friction stir welding (FSW) on the corrosion resistance of aluminium alloy 2524-T3

Maurilio Pereira Gomes

To cite this version:

Maurilio Pereira Gomes. Investigation on the corrosion mechanisms of pure magnesium and the effect of friction stir welding (FSW) on the corrosion resistance of aluminium alloy 2524-T3. Material chemistry. Sorbonne Université; Universidade de São Paulo (Brésil), 2021. English. NNT : 2021SORUS531 . tel-03783498

HAL Id: tel-03783498

https://theses.hal.science/tel-03783498v1

Submitted on 22 Sep 2022

HAL is a multi-disciplinary open access archive for the deposit and dissemination of scientific research documents, whether they are published or not. The documents may come from teaching and research institutions in France or abroad, or from public or private research centers.

L'archive ouverte pluridisciplinaire **HAL**, est destinée au dépôt et à la diffusion de documents scientifiques de niveau recherche, publiés ou non, émanant des établissements d'enseignement et de recherche français ou étrangers, des laboratoires publics ou privés.

INSTITUTO DE PESQUISAS ENERGÉTICAS E NUCLEARES

Autarquia Associada à Universidade de São Paulo

Investigation on the corrosion mechanisms of pure magnesium and the effect of friction stir welding (FSW) on the corrosion resistance of aluminum alloy 2524-T3

MAURILIO PEREIRA GOMES

Thesis presented as part of the requirements for obtaining the degree of Doctor of Science in Nuclear Technology - Materials.

Supervisor: Dr. Isolda Costa

Supervisor: Dr. Vincent Vivier

São Paulo

2021

INSTITUTO DE PESQUISAS ENERGÉTICAS E NUCLEARES
Autarquia Associada à Universidade de São Paulo

Investigation on the corrosion mechanisms of pure magnesium and the effect of friction stir welding (FSW) on the corrosion resistance of aluminum alloy 2524-T3

Corrected Version

MAURILIO PEREIRA GOMES

Thesis presented as part of the requirements for obtaining the degree of Doctor of Science in Nuclear Technology - Materials.

Supervisor: Dr. Isolda Costa
Supervisor: Dr. Vincent Vivier

São Paulo
2021

INSTITUTO DE PESQUISAS ENERGÉTICAS E NUCLEARES
Diretoria de Pesquisa, Desenvolvimento e Ensino
Av. Prof. Lineu Prestes, 2242 – Cidade Universitária CEP: 05.508-000
Fone/Fax (0XX11) 3133-8908
SÃO PAULO – São Paulo – Brasil
http://www.ipen.br

O IPEN é uma Autarquia vinculada à Secretaria de Desenvolvimento, associada à Universidade de São Paulo e gerida técnica e administrativamente pela Comissão Nacional de Energia Nuclear, órgão do Ministério da Ciência, Tecnologia, Inovações e Comunicações.

CATALOGRAPHIC SHEET

ABSTRACT

GOMES, M. P**. Investigation on the corrosion mechanisms of pure magnesium and the effect of friction stir welding (FSW) on the corrosion resistance of aluminum alloy 2524-T3**. 2021. 106 p. Thesis (Doctor degree in Nuclear Technology) Nuclear and Energy Research Institute - IPEN - CNEN/SP. São Paulo.

Friction stir welding (FSW) is a process that has proven to be quite efficient when it comes to joining high-strength aluminum alloys, for instance AA2524-T3. This can be justified by the fact that welding aluminum alloys by FSW technique allows (i) reduction of aircraft weight by eliminating the rivets commonly used and (ii) the use of different aluminum alloys that have low specific density and high mechanical strength. However, even though FSW allows the joining of metallic parts without their effective fusion, which theoretically would result in a defect-free weld bead, the heat resulting from the friction of the welding tool causes significant microstructural changes. In consequence, it results in variations of mechanical properties and corrosion resistance in the welded region. It was evaluated the FSW welding process influence on the corrosion resistance of the joined 2524-T3 aluminum alloy. Different tools have been used, such as: optical and scanning electron microscopy; open circuit potential and electrochemical impedance spectroscopy measurements; and corrosion tests: agar-agar test, intergranular corrosion test, and exfoliation corrosion test. It was proven by different techniques that the thermomechanically/thermal affect zone interface on the retreating side was the most susceptible to corrosion among all investigated zones.

A parallel study was developed regarding the corrosion mechanism of pure magnesium. It has been the subject of a considerable amount of work, and despite its ubiquity and history, it remains controversial. This is mainly due to the presence of the negative difference effect (NDE), which increases hydrogen formation when the magnesium is biased on the anodic domain. We was performed a detailed analysis of the electrochemical impedance spectra obtained for the Mg electrode during immersion in a sodium sulfate solution. A model was proposed which took into account the presence of: (i) a thin oxide film (MgO) which progressively covered the Mg electrode surface, (ii) film-free areas where the Mg dissolution occurs in two consecutive steps, (iii) a thick layer of corrosion products ($Mg(OH)_2$), (iv) an adsorbed intermediate $\mathrm{Mg}^{+}_{\mathrm{ads}}$ which is responsible for the chemical reaction allowing the NDE to be explained. From the impedance data analyses, various parameters were extracted such as the thin oxide film thickness, the resistivity at the metal/oxide film interface and at the oxide film/electrolyte interface, the active surface area as a function of the exposure time to the electrolyte, the thickness of the thick $Mg(OH)_2$ layer and the kinetic constants of the electrochemical reactions.

Keywords: AA2524-T3; Friction stir welding (FSW); Magnesium, Negative difference effect (NDE).

RESUMO

GOMES, M. P. **Investigação dos mecanismos de corrosão do magnésio puro e o efeito da soldagem por fricção e mistura (FSW) na resistência à corrosão da liga de alumínio 2524-T3**. 2021. 106 p. Tese (Doutorado em Tecnologia Nuclear) Instituto de Pesquisas Energéticas e Nucleares - IPEN - CNEN/SP. São Paulo.

A soldagem por fricção e mistura (FSW) é um processo que tem se demonstrado bastante eficiente quando o intuito é unir ligas de alumínio de alta resistência, por exemplo AA2524-T3. Isto é justificado pelo fato da soldagem das ligas de alumínio pela técnica FSW permitir (i) a redução do peso das aeronaves por meio da eliminação de rebites usualmente utilizados e (ii) a utilização de diferentes ligas de alumínio que possuem baixa densidade específica e alta resistência mecânica. Porém, mesmo a FSW possibilitando a junção de partes metálicas sem a sua efetiva fusão, teoricamente resultando na obtenção de um cordão de solda isento de defeitos, o calor resultante do atrito da ferramenta de soldagem causa mudanças microestruturais significativas. Isso, por sua vez, resulta em variações nas propriedades mecânicas e de resistência à corrosão na região soldada. Foi avaliada a influência do processo de soldagem FSW na resistência à corrosão da liga de alumínio 2524-T3 soldada. Foram utilizadas diferentes técnicas, tais como: microscopia óptica e eletrônica de varredura; medidas de potencial de circuito aberto e espectroscopia de impedância eletroquímica; e testes de corrosão: ágar-ágar, corrosão intergranular, e corrosão por esfoliação. Foi comprovado por diferentes técnicas que a interface da zona termomecanicamente/termicamente afetada do lado do retrocesso foi a que apresentou maior susceptibilidade à corrosão entre todas as zonas investigadas.

Um estudo paralelo foi desenvolvido em relação aos mecanismos de corrosão do magnésio puro. Esse tem sido objeto de uma grande quantidade de estudos e, apesar de sua ubiquidade e histórico, ainda é controverso. Isso se deve principalmente à presença do efeito de diferença negativa (do inglês *negative difference effect*, NDE), que resulta no aumento da formação de hidrogênio quando o magnésio é polarizado no domínio anódico. Foi realizada uma análise detalhada dos espectros de impedância eletroquímica obtidos para o eletrodo de Mg durante imersão em solução de sulfato de sódio. Foi proposto um modelo que levou em consideração a presença de: (i) um filme fino de óxido de magnésio (MgO) que cobriu progressivamente a superfície do eletrodo de Mg, (ii) áreas livres de filme de óxido onde ocorre a dissolução do Mg em duas etapas consecutivas, (iii) uma camada espessa de produto de corrosão ($Mg(OH)_2$), (iv) um intermediário adsorvido $\mathrm{Mg}^{+}_{\mathrm{ads}}$ que é responsável pela reação química que permite a explicação do NDE. Das análises dos dados de impedância, vários parâmetros foram extraídos, como a espessura do filme de óxido fino, resistividade na interface metal/óxido e na interface óxido/eletrólito, área de superfície ativa em função do tempo de exposição à solução, espessura da camada espessa de $Mg(OH)_2$ e constantes cinéticas das reações eletroquímicas.

Palavras-chave: AA2524-T3; Soldagem por fricção e mistura (FSW); Magnésio, Efeito da diferença negativa (NDE).

RÉSUMÉ

GOMES, M. P. **Investigation des mécanismes de corrosion du magnésium pur et de l'effet du soudage par friction et mélange (FSW) sur la résistance à la corrosion de l'alliage d'aluminum 2524-T3**. 2021. 106 p. Thèse (Doctorat en technologie nucléaire) Institut de Recherches Energétiques et Nucléaires - IPEN - CNEN/SP. A São Paulo.

Le soudage par friction et mélange (FSW) est un processus qui s'est révélé très efficace lorsqu'il s'agit d'assembler des alliages d'aluminum à haute résistance, par exemple AA2524-T3. Cela peut être justifié par le fait que le soudage des alliages d'aluminum par la technique FSW permet (i) de réduire le poids des avions en éliminant les rivets couramment utilisés et (ii) d'utiliser différents alliages d'aluminum qui ont une faible densité spécifique et une résistance mécanique élevée. Cependant, même si ce type de soudure permet d'assembler des pièces métalliques sans leur fusion effective, ce qui devrait théoriquement se traduire par un cordon de soudure sans défaut, la chaleur résultant du frictionnement de l'outil de soudage provoque d'importantes modifications microstructurelles. Il en résulte des variations des propriétés mécaniques et de la résistance à la corrosion dans la région soudée. Il a été évalué l'influence du processus de soudage FSW sur la résistance à la corrosion de l'alliage d'aluminum 2524-T3 joint. Différentes techniques ont été utilisés, telles que microscopies optique et électronique à balayage ; des mesures de potentiel en circuit ouvert et de spectroscopie d'impédance électrochimique ; et des tests de corrosion : agar-agar, corrosion intergranulaire et corrosion par exfoliation. Il a été montré par différentes techniques que l'interface de la zone affectée thermomécaniquement/thermiquement du côté du retrait était la plus sensible à la corrosion parmi toutes les zones étudiées.

Une étude parallèle a été développée concernant le mécanisme de corrosion du magnésium pur. Ce métal a fait l'objet d'un nombre considérable de travaux et, malgré son ubiquité et son histoire, il reste controversé. Ceci est principalement dû à la présence de l'effet de différence négative (NDE), qui augmente la formation d'hydrogène lorsque le magnésium est polarisé sur le domaine anodique. Une analyse détaillée des spectres d'impédance électrochimique obtenus pour l'électrode de Mg lors de son immersion dans une solution de sulfate de sodium a été réalisée. Un modèle a été proposé qui prend en compte la présence de : (i) d'un mince film d'oxyde (MgO) qui a progressivement recouvert la surface de l'électrode de Mg, (ii) de zones sans film où la dissolution du Mg se produit en deux étapes consécutives, (iii) d'une épaisse couche de produits de corrosion ($Mg(OH)_2$), (iv) d'un intermédiaire adsorbé $\mathrm{Mg}^{+}_{\mathrm{ads}}$ qui est responsable de la réaction chimique permettant d'expliquer le NDE. A partir des analyses des données d'impédance, différents paramètres ont été extraits tels que l'épaisseur du film d'oxyde mince, la résistivité à l'interface métal/film d'oxyde et à l'interface film d'oxyde/électrolyte, la surface active en fonction du temps d'exposition à l'électrolyte, l'épaisseur de la couche épaisse de $Mg(OH)_2$ et les constantes cinétiques des réactions électrochimiques.

Mots-clés : AA2524-T3 ; Soudage par friction et mélange (FSW) ; Magnésium, Effet de différence négative (NDE).

LIST OF TABLES

Table 3.1 - Nominal chemical compositions (wt. %) of the AA2024 and AA2524 alloys [73]. ...8

Table 4.1 - Chemical composition (wt.% or ppm) obtained by inductively coupled plasma - optical emission spectrometry (ICP-OES) of the aluminum alloy 2524 used in this study. 28

Table 4.2- Impurity quantities (ppm) of the commercially pure magnesium used in this work (Goodfelow). 28

Table 5.1 - Area covered by particles with sizes greater than 10 μm^2 over the AA2524-T3 welded sample. 39

LIST OF FIGURES

Figure 3.1 - Precipitation hardening of aluminum-copper alloy [76]. 8

Figure 3.2 - Schematic representation of the effect of coherent (a) and incoherent (b) precipitates [76]. 9

Figure 3.3 - Typical aging curve for aluminum alloys [76]. 10

Table 3.2 - Temper designation for aluminum alloys [76], [77]. 10

Figure 3.4 - Schematic representation of the FSW process. The letters used to designate the different zones formed along the cross section refer to the (a) advancing side base metal zone (BM-AS), (b) advancing side heat affected zone (HAZ-AS), (c) stir zone (SZ), (d) retreating side heat affected zone (HAZ-RS), (e) retreating side base metal zone (BM-RS) and (f) thermomechanically affected zone (TMAZ). Adapted from [11], [100]. 14

Figure 3.5 - a) Electrochemical impedance diagrams plotted after different hold times of pure Mg in 0.1 M Na_2SO_4 solution at E_{corr} with an electrode rotation rate of 240 rpm: (∘) 1 h 30 min, (•) 21 h and (□) 32 h; b) normalized impedance diagrams, and c) simulated impedance diagram using a proposed kinetic model [53]. 21

Figure 3.6 - Schematic representation of the interface and the equivalent circuit [53]. 22

Figure 3.7 - Optical micrographs taken in situ of a corroding pure Mg (99.9 wt.%, 280 ppm of Fe) after 40 min in a NaCl solution at pH 6.5 with concentrations of a) 1 M, b) 0.1 M and c) 10^{-2} M [125]. 23

Figure 3.8 - A schematic representation of the anodic hydrogen evolution process that distinguishes the contribution of corrosion film, accumulated impurities, and anodic area [27]. 24

Figure 3.9 - Hydrogen evolution current density plotted as a function of the applied anodic current density. The experiment was performed in a galvanostatic polarization mode (iTOT), and the contribution of hydrogen released from uncovered areas (iANOD) or covered by a film of corrosion products ($\mathrm{iFilm} + \mathrm{Imp}$) was calculated [129]. 24

Figure 3.10 - a) STEM micrograph and b) depth profile showing the O/Mg atomic ratio across the Mg/oxide film interface formed during conditioning at E_{corr} in 0.01 M NaCl for 24 h [130]. 25

Figure 3.11 - Instantaneous corrosion rate determined from hydrogen evolution, PH, from the corrosion current density from the polarization curve, Pi, and from EIS, $\mathrm{Pi/EIS}$, for the high purity Mg plotted versus immersion time in 3.5% NaCl saturated with $Mg(OH)_2$ at 25 °C [137]. 26

Figure 4.1 - Organization scheme and description of all tests performed. 29

Figure 5.1 - Optical micrographs of FSW-welded 2524-T3 alloy after chemical etch in 25% (vol.) HNO_3 and 2% (vol.) HF solution in distilled water for 7 seconds. It shows the different zones after the welding process: (1) base metal (BM), heat affected zone (HAZ) and thermomechanically affected zone (TMAZ) on the retreating side (RS); (2) stir zone (SZ); and (3) base metal (BM), heat affected zone (HAZ) and thermomechanically (TMAZ) affected zone on the advancing side (AS). 34

Figure 5.2 - Microhardness profile along the cross section of the AA2524-T3 FSW-welded sample. 35

Figure 5.3 - Macrographs showing the color variation directly linked to the pH change along the surface (top view) of a FSW-welded AA2524-T3 sample during the agar-agar visualization test. 37

Figure 5.4 - Electron micrographs of the TMAZ/HAZ-RS (a) and the TMAZ/HAZ-AS zones (c) and its image particle distribution analysis, respectively (b) and (d). 39

Figure 5.5 - Macrographs of the welded AA2524-T3 sample (a) and its base metal separately (b) after 15 minutes of immersion in EXCO solution. Additionally, it is shown cross section micrographs obtained by SEM of the welded sample: (1) TMAZ/HAZ-RS, (2) TMAZ/HAZ-AS, (3) BM, and separately, (4) BM after the exfoliation corrosion test. 41

Figure 5.6 - Macrographs of the welded AA2524-T3 sample (a) and its base metal separately (b) after 30 minutes of immersion in the intergranular corrosion test solution. Cross section micrographs obtained by SEM of the welded sample: (1) BM-RS, (2) SZ, and, (3) BM tested separately, after intergranular corrosion test. 43

Figure 5.7- Open circuit potential variation with time of immersion in 100 mM Na_2SO_4 + 1 mM NaCl solution of different zones of the AA2524-T3 welded by FSW. 44

Figure 5.8 - Electrochemical impedance diagrams after 4 h, 8 h, 16 h and 24 h, of immersion in 100 mM Na_2SO_4 + 1 mM NaCl solution for the following zones: BM (a), TMAZ/HAZ-RS (b), SZ (c), and TMAZ/HAZ-AS (d). 47

Figure 5.9 - Corrosion potential (-) and pH variation in 0.1 mol.L^{-1} Na_2SO_4 solution (Ω = 1000 rpm), with (-) and without (-) Mg in solution, as a function of immersion time. 50

Figure 5.10 - Current-potential curves obtained after 2 h (-) and 24 h (-) of pure Mg immersion in 0.1 mol.L^{-1} Na_2SO_4 solution at E_{corr} (Ω = 1000 rpm and v = 0.167 mV.s^{-1}). The anodic and cathodic branches were obtained separately from E_{corr} (independent measurements), and the curves were corrected for the ohmic drop. 51

Figure 5.11 - Electrochemical impedance diagrams of pure Mg after 12 hours of immersion in 0.1 mol.L^{-1} Na_2SO_4 solution at E_{corr} for different rotation rates: a) raw impedance diagrams (Nyquist representation) and b) normalized impedance diagrams (each diagram was normalized by the maximum value of the real part of the impedance). 53

Figure 5.12 - Electrochemical impedance diagrams obtained for pure Mg after different immersion times in 0.1 mol.L^{-1} Na_2SO_4 solution at E_{corr} (Ω = 1000 rpm): a) raw impedance diagrams (Nyquist representation) and b) normalized impedance diagrams (each diagram was normalized by the maximum value of the real part of the impedance). 54

Figure 5.13 - Sketch of the interface describing the different layers formed during the Mg corrosion. According to the impedance data analysis, the MgO layer thickness is about 5-7 nm (Figure 5.17) and the $Mg(OH)_2$ layer thickness is about 20-30 μm (Figure 5.20).....56

Figure 5.14 - Electrochemical impedance diagrams of pure Mg after 12 hours of immersion in 0.1 mol.L^{-1} Na_2SO_4 solution at E_{corr} (Ω = 1000 rpm) for two anodic overpotentials: a) raw impedance diagrams (Nyquist representation) and b) normalized impedance diagrams (each diagram was normalized by the maximum value of the real part of the impedance).....62

Figure 5.15 - Electrochemical impedance response of pure Mg after 35 hours of immersion in 0.1 mol.L^{-1} Na_2SO_4 solution at E_{corr} (Ω = 1000 rpm). a) Variations of the phase angle (circle) and corrected phase angle from the ohmic resistance (triangle) as a function of the frequency; b) variations of the absolute value of the imaginary part of the impedance as a function of the frequency. 64

Figure 5.16 - Complex-capacitance plot obtained from the electrochemical impedance response of Mg after 35 h of immersion in a 0.1 mol.L^{-1} Na_2SO_4 solution (Ω = 1000 rpm) from the data presented in Figure 5.12 using Eq. (3). The axis is not orthonormal to make the extrapolation to the C_∞ axis better visible. 65

Figure 5.17 - Oxide film thickness formed on the Mg surface as a function of immersion time in 0.1 mol.L^{-1} Na_2SO_4 solution (Ω = 1000 rpm). Each point of this curve corresponds to the analysis of the complex-capacitance plot, as shown in Figure 5.16.....66

Figure 5.18 - (a) Resistivity at the metal/oxide interface and (b) at the oxide/solution interface of the MgO thin film as a function of immersion time for the corrosion of Mg in 0.1 mol.L^{-1} Na_2SO_4 solution (Ω = 1000 rpm). These data were obtained from the fitting procedure assuming a power-law model for the description of the interfacial capacitance (see text). 68

Figure 5.19 - Impedance response of Mg after 35 h of immersion in 0.1 mol.L^{-1} Na_2SO_4 solution (Ω = 1000 rpm) in a Nyquist representation (blue circles) and fitting of the EIS response with the model (Eqs. (22) and (25)) (red crosses). The fitted diagram corresponds to the following parameters: b_1 = 28.9 V^{-1}, b_2 = 11.8 V^{-1}, b_{-2} = 9.3 V^{-1}, k_1 = 2.32 x 10^{-10} cm^2.s^{-1}, k_2 = 9.35 x 10^{-2} cm^2.s^{-1}, k_{-2} = 7.58 x 10^{-4} cm^2.s^{-1}, k_3 = 8.16 x 10^{-3} cm^2.s^{-1}, δ_{corr} = 22.2 µm, δ_{ox} = 6.7 nm, D = 3 x 10^{-6} cm^2.s^{-1}, β = 10^{-6} mol.cm^{-2}. 70

Figure 5.20 - Total thickness of the corrosion layer formed on Mg surface as a function of immersion time in 0.1 mol.L^{-1} Na_2SO_4 solution (Ω = 1000 rpm) obtained from the fitting of the impedance diagram, as exemplified in Figure 5.19.....71

Figure 5.21 - Active surface area evolution as a function of the immersion time for Mg in 0.1 mol.L^{-1} Na_2SO_4 solution (Ω = 1000 rpm). The relative surface area was calculated from the charge transfer resistance, determined from the diameter of the first capacitive loop of the impedance diagram for each immersion time (Figure 5.12) and by using the first measurement performed, after 2 h of immersion, as the reference value.....73

Figure 5.22 - Kinetic parameters evolution corresponding to a) k_1 related to reaction 5.6 and b) k_2 related to reaction 5.7 as a function of immersion time for the corrosion of Mg in 0.1 mol.L^{-1} Na_2SO_4 solution (Ω = 1000 rpm). The blue open circles correspond to the raw kinetic constant determined from the fitting procedure; the plain blue circles are the same data corrected from the surface variations (see text); the red squares correspond to the variation of the Tafel coefficient.....74

TABLE OF CONTENTS

1. INTRODUCTION 1

1.1. Interest of light metal and alloys 1

1.2. Aluminum 1

1.3. Magnesium 2

2. OBJECTIVE 5

2.1. General objective 5

2.2. Specific objectives 5

3. LITERATURE REVIEW 7

3.1. Aluminum 7

3.1.1. Aluminum alloy 7

3.1.1.1. Age-hardenable alloys 8

3.1.1.2. Heat treatment designation 10

3.1.1.3. Corrosion of aluminum-copper-magnesium (Al-Cu-Mg) alloys 11

3.1.1.4. Electrochemical techniques applied to aluminum corrosion investigation 13

3.1.1.4.1. Conventional electrochemical techniques 13

3.1.1.5. Friction Stir Welding (FSW) 13

3.1.1.5.1. FSW technique 13

3.1.1.5.2. Microstructure of aluminum alloys joined by FSW 14

3.1.1.5.3. Influence of FSW on the corrosion behavior of aluminum alloys 16

3.2. Magnesium 19

3.2.1. Kinetic aspect: the negative difference effect (NDE) and current reaction mechanisms 19

3.2.1.1. Model based on the existence of a monovalent ion 19

3.2.1.2. Model based on the existence of a cathodic film 22

3.2.2. Corrosion product film 25

3.2.3. Determination of the corrosion rate 25

4. MATERIALS AND METHODS 28

4.1. Materials 28

4.1.1. Aluminum 28

4.1.2. Magnesium 28

4.2. Methods 28

4.2.1. Aluminum 29

4.2.1.1. Friction Stir Welding (FSW) 29

4.2.1.2. Microstructural characterization 29

4.2.1.2.1. Sample preparation 29

4.2.1.2.2. Optical Microscopy (OM) 29

4.2.1.2.3. Scanning Electron Microscopy (SEM) 30

4.2.1.3. Corrosion tests 30

4.2.1.3.1. Exfoliation corrosion test (ASTM G34) 30

4.2.1.3.2. Intergranular corrosion test (ASTM G110) 30

4.2.1.3.3. Agar-agar test 30

4.2.1.3.4. Vickers microhardness 31

4.2.2. Magnesium 31

4.2.2.1. Sample preparation 31

4.2.2.2. Experimental setup 31

4.2.3. Electrochemical techniques 32

4.2.3.1. Conventional electrochemical techniques 32

4.2.3.1.1. Open circuit potential (OCP) measurements 32

4.2.3.1.2. Potentiodynamic polarization (Polarization) 32

4.2.3.1.3. Electrochemical impedance spectroscopy (EIS) 32

5. RESULTS AND DISCUSSION 33

5.1. Aluminum 33

5.1.1. Microstructural characterization 33

5.1.1.1. Microstructure of AA2524-T3 welded by FSW 33

5.1.1.2. Microhardness test 35
5.1.2. Corrosion tests 36
5.1.2.1. Agar-agar test 36
5.1.2.1.1. Image analysis 38
5.1.2.2. Exfoliation corrosion test (ASTM G34) 40
5.1.2.3. Intergranular corrosion test (ASTM G110) 42
5.1.3. Electrochemical characterization of the FSW-welded AA2524-T3 44
5.2. Magnesium 49
5.2.1. Steady-state measurements 49
5.2.2. Electrochemical impedance measurements 52
5.2.2.1. Electrochemical impedance diagrams at E_{corr} 52
5.2.2.2. Kinetics model of the corrosion mechanism 55
5.2.2.3. Electrochemical impedance diagrams at low anodic over potentials 61
5.2.2.4. Interfacial capacitance 63
5.2.3. Modeling of the electrochemical response 69
6. CONCLUSIONS 76
6.1. General conclusions 76
6.2. Specific conclusions 76
7. FUTURE WORKS 78
8. REFERENCES 79

1. INTRODUCTION

1.1. Interest of light metal and alloys

Lightweight metal and alloys have become of great importance in engineering for construction of transportation equipment. At present, the metals that serve as the base of the principal light alloys are aluminum and magnesium. One of the most important lightweight alloys are the aluminum alloys in use for several applications such as structural components, wrought aluminum alloys, parts and plates. However, some casting parts that have low cost of production play important role in aircraft industries. Magnesium and its alloys are among the lightest of all metals and the sixth most abundant metal on earth. Magnesium is ductile and the most machinable of all metals. Many of these lightweight alloys have appropriately high strength to warrant their use for structural purposes, and as a result of their use, the total weight of transportation equipment has been considerably decreased [1].

1.2. Aluminum

Aluminum alloys are produced and used in many forms such as casting, sheet, plate, bar, rod, channels and forgings in various areas of industry and especially in the aerospace industry. The advantages of these alloys over traditional iron-based alloys are lightweight, corrosion resistance, and very good thermal and electrical conductivities. These factors plus the fact that some of these alloys can be formed in soft condition and heat treated to a temperature comparable to structural steel make them very attractive for fabricating various aircraft and missile parts. Aluminum alloys are effective materials for the reduction of vehicle weight and are expanding their applications [2], [3].

Pure aluminum has a high resistance to corrosion in many environments as a result of a protective film rapidly formed on its surface when exposed to air or in neutral aqueous solutions. This film is preserved even after long periods of immersion in acid and alkaline media. However, in order to increase the mechanical properties of aluminum, alloying additions of Cu and Zn have been made. As the solubility in aluminum of both these elements is limited, second phase particles are formed, which are responsible for the enhancement of the mechanical performance that is characteristic of duraluminum. The formation of these precipitates has a deleterious effect on the corrosion resistance of the alloys, due to the galvanic coupling between the precipitates and the matrix [4].

Aluminum alloys from the 2xxx series are widely used in the aerospace industry due to their lightweight, high specific strength and durability from which the most important brand is

the 2024-T3 [5], [6]. However, in the last years, efforts to improve mechanical and corrosion resistances of these alloys have led to the launch of the 2X24 (X = 1-5) series with stricter control of the main alloying elements and lower limits of Fe and Si impurities levels [7].

Aluminum alloy 2524 is a new kind of aerospace material with high damage-tolerance and excellent fatigue properties [7]. It has been considered as a potential substitute for the commercial Al 2024 alloy and is currently used on the Boeing 777 aircraft as fuselage and lower wing skin materials [8], [9].

Friction stir welding (FSW), a recently developed solid-state joining technique, was devised by The Welding Institute (TWI) in 1991 [10]. This technique is attractive for joining high strength aluminum alloys for aerospace, automotive and marine applications since there is far lower heat input during welding (80% max. of Al melting temperature) compared with conventional welding methods such as TIG or MIG. In addition, to perform FSW-welding no additional support material is needed, i.e., leading to drastically weight reduction of the joined aircraft parts when comparing to the use of rivets (60% less) [11]–[14].

1.3. Magnesium

Magnesium is the lightest of all structural metal materials in practical use, with a density equivalent to two-thirds that of Al, one-third that of Zn and one quarter that of steel. Magnesium alloys are therefore recognized as alternatives to Al alloys and steel in reducing the weight of structural materials. Furthermore, magnesium alloys have high strength-to-weight ratios, excellent castability, machinability, weldability, thermal stability and good damping capacity [15]–[17].

These properties make magnesium alloys an attractive target in a number of applications, especially in fields where weight reduction is critical for particular technical requirements. Magnesium alloys have several applications, including in automobiles, computer parts, mobile phones, sporting goods, hand-held tools, household equipment and aero- space components. Magnesium alloys could also contribute towards meeting future requirements of the automotive industry to make lighter cars and thus improve fuel efficiency and reduce emissions, as the use of magnesium alloys would significantly decrease the weight of automobiles without sacrificing structural strength [18], [19].

Pure magnesium is rarely used in industrial engineering applications. However, for improving its mechanical and other properties, alloying elements are added, most commonly aluminum, manganese, zinc, zirconium, silicon, calcium and rare earth elements. In appropriate

amounts, these additives enhance the anticorrosion and mechanical properties of magnesium alloys [15], [20].

Aluminum has the most favorable effect on magnesium: it improves strength and hardness, increases the freezing range and makes the alloy easier to cast. However, one of the major obstacles to widespread use of magnesium alloys is its poor corrosion resistance: magnesium alloys are highly susceptible to corrosion attack, particularly in wet environments. Therefore, selecting appropriate alloying elements and finding the best alloy design constitute the first step to improve the anticorrosion property of magnesium alloys [18], [21], [22].

The corrosion mechanism of Mg has been the subject of considerable amount of work [18], [23]–[26], and despite its ubiquity and history, the primary mechanism remains poorly understood. This is mainly due to an anomalous phenomenon called the negative difference effect (NDE) which increases the hydrogen evolution reaction rate when the magnesium is anodically polarized [22], [27]. Indeed, even if this phenomenon has been well documented in the literature [25], [27]–[29] and has been observed from various techniques [16], [30]–[33], the mechanism itself is tricky and the subject has become controversial. At the corrosion potential, there is a good agreement with the global reaction (Eq. (1.1)):

$$\mathrm{Mg} + \mathrm{H}^{+} + \mathrm{H_2O} \rightarrow \mathrm{Mg}^{2+} + \mathrm{OH}^{-} + \mathrm{H_2} \tag{1.1}$$

Followed by the formation of corrosion products (Eq. (1.2)):

$$\mathrm{Mg}^{2+} + 2\mathrm{OH}^{-} \rightarrow \mathrm{Mg(OH)_2} \tag{1.2}$$

Even if it is written in a global form, Eq. 1.1 also accounts for the formation of the dihydrogen, and is in agreement with one of the striking observations that can be done on Mg, namely the amount of dihydrogen formed seems to depend on the amount of Mg oxidized. The rate of the NDE has been intensely investigated as a function of impurities contained in the Mg [34]–[37]. Metal impurities, even in small amounts, (e.g., Fe, Cu, Ni), result in large overpotential for the hydrogen evolution reaction at the Mg corrosion potential. However, from a thermodynamic point of view, even if these impurities act as local cathodes, any shift of the potential towards the anodic domain, it should result in a decrease of the hydrogen production reaction. Consequently, the metal impurities cannot be the only factors responsible for the NDE, but such behavior has been further investigated for alloying elements [38], [39].

Other developments, including film-based model [25], [40], formation of magnesium

hydride [41], [42], or formation of a soluble univalent Mg species [43]–[45] have been proposed to make an attempt to explain the NDE. For the latter, the existence of soluble univalent species dissolved in solution remains questionable [25]. Thus, there is a need to understand how the NDE takes place at the electrode surface and its role on the corrosion mechanism of the Mg.

Additionally, the overall corrosion of Mg also leads to the formation of a thin oxide film (in the nanometer range) on the Mg surface in different corrosive environments. This thin film has been evidenced by means of X-ray photoelectron spectroscopy (XPS) [46], [47] or time-of-flight secondary ion mass spectroscopy (ToF SIMS) depth profiles [48], [49].

Interestingly, the use of electrochemical impedance spectroscopy (EIS) has delivered reliable and reproducible results for the study of Mg corrosion [50]–[53]. However, in many studies the analysis of the impedance spectra was mainly limited to the study of the charge transfer resistance and to the evaluation of the polarization resistance as the main parameter to describe the corrosion kinetics of the material [54].

Recently, a mathematical model for describing the inductive loop that appears in the EIS results has been devised to account for the production of the excess of hydrogen [55]. This model takes into account the evolution of the electrode surface over time, but it was uncorrelated from any kinetic aspect allowing the NDE to be linked to the corrosion mechanism of Mg. Moreover, plotting EIS data in different representations allows further analysis, in particular, the determination of the interfacial capacitance [56]. For instance, the use of complex capacitance representation allows the characterization of thin oxide layers formed on passive metals [57]–[60], or on Mg alloys [20], resulting in a possible evaluation of the oxide layer thickness.

2. OBJECTIVE

2.1. General objective

The main objective of this work is developed through two axes of which the understanding of the corrosion of light alloys is the guideline.

- This study aims at employing microstructural characterization, electrochemical and corrosion testing techniques to allow a better understanding the effects of friction stir welding process on the microstructure and the corrosion resistance of the 2524-T3 aluminum alloy welded by FSW.
- Proposing a corrosion mechanism based on the experimental evidences from EIS for pure magnesium, since many different mechanisms have been proposed and they are controversial.

2.2. Specific objectives

- The objective of the first part of this work was to study the corrosion behavior of the aluminum alloy 2524-T3, being this alloy developed to replace the AA2024 alloy, presenting lower levels of impurities. For joining aluminum plates, the friction stir welding (FSW) technique has been an alternative, because it is not necessary to add any material to perform the welding process and this technique introduces lower temperatures during welding, which reduces the amount of defects in the weld joint. Thus, it is necessary to evaluate the corrosion mechanism of the AA2524-T3 alloy after the FSW process.
- It was aimed to characterize the microstructural modifications introduced into the alloy during welding, which mainly results in the formation of four different microstructural zones, namely: base metal (BM), stir zone (SZ), heat affected zone (HAZ), and thermomechanically affected zone (TMAZ).
- Due to the quite complex microstructural modifications, it was intended to understand how these modifications affect the electrochemical behavior of the different welded zones of the aluminum alloy. Furthermore, it was aimed to evaluate the existence of galvanic couplings between the different zones and their corrosion resistance.

- The second part of this work aimed at better understanding the corrosion mechanism of pure magnesium, since this material has several engineering applications and is biocompatible with the human body, and the different models proposed so far are often controversial and ambiguous.
- In order to better understand the corrosion mechanism of pure Mg, a detailed analysis of its mechanism was performed using different electrochemical techniques and sodium sulfate solution. Also, it was aimed at extending the scope of a previously developed model involving the relaxation of an adsorbed intermediate [53]. Finally, it was intended to investigate the evolution of kinetic parameters by means of the fitting procedure of the EIS spectra.

3. LITERATURE REVIEW

3.1. Aluminum

Pure aluminum has two main characteristics that justify its use in the aeronautical industry. The first is associated with its low density (2.7 g cm^{-3}), approximately one third of the density of most steels (7.8 g cm^{-3}). In addition, it has excellent corrosion resistance in various media, including in air atmosphere, to which aircraft are constantly exposed. Such protection originates from the formation of a thin layer of aluminum oxide (Al_2O_3) which is a nanometric film when the alloy is exposed to atmospheric air, and which gives the aluminum excellent corrosion resistance [61]. However, aluminum in its genuine form does not meet the levels of mechanical resistance required for its use as structural material in the aviation industry. For this reason, the metallurgical industries have developed a large variety of aluminum alloys [62], [63].

The German Alfred Wilm in 1903, aiming at increasing the mechanical resistance of pure aluminum and taking advantage of its low density and high corrosion resistance, found that aluminum could be hardened by the phenomenon of precipitation hardening when inserting 4% of copper during the production of these alloys. In continuation to his experiments, six years later Wilm developed an aluminum alloy with high mechanical strength by adding small amounts of magnesium and manganese to his initial alloy. Such aluminum alloy is the 2xxx series precursor [64], [65].

3.1.1. Aluminum alloy

2xxx aluminum alloys are widely used for aerospace structural components due to their high strength and low density [66], [67]. The most employed alloy is the AA2024, which is used in parts where toughness, fatigue resistance and mechanical strength are major requirements, like in fuselages and shear webs [68]. However, aircraft designers have required materials with better performances and enhanced corrosion resistance properties than the conventional AA2024 alloy [66], [69], [70]. In this way, in the 1990s the Aluminum Company of America (ALCOA) developed the AA2524, a purer version of AA2024 with lower and better controlled amounts of alloying elements [66], [71] as well as decreased impurities amount. Nowadays, AA2524 sheets are used as skin sheets in Boeing and Airbus aircrafts [67], [72].

Table 3.1 shows the comparison between the nominal chemical compositions of the AA2024 and AA2524 [73]. In the latter alloy, there is a tighter control in the amounts of the two main alloying elements (Cu and Mg) and lower quantities of Fe and Si, which are impurities

frequently found in the composition of the 2xxx series aluminum alloys. For both alloys, Cr, Mn and Cu are added to control grain structure, weldability and corrosion resistance [74]. In addition, Cu is added to improve the mechanical resistance [75]. According to Chen et al. (2013) [9], by controlling the impurity contents and the process parameters, the AA2524-T3 can exhibit approximately 15% - 20% increase in fracture toughness, twice the fatigue crack growth resistance, and 30% - 40% longer lifetime before failure when compared to AA2024-T3, without loss of strength or corrosion resistance.

Table 3.1 - Nominal chemical compositions (wt. %) of the AA2024 and AA2524 alloys [73].

Alloy	Cu	Mg	Mn	Zn	Fe	Ti	Si	Cr	Al
AA2024	3.80 - 4.90	1.20 - 1.80	0.90	0.30	0.50	-	0.50	0.10	Balance
AA2524	4.00 - 4.50	1.20 - 1.60	0.45 - 0.90	0.15	0.12	0.10	0.06	0.05	Balance

Additionally, DeBartolo and Hillberry (2001) [71] report significant reduction in the amount of the S-type (Al_2CuMg) intermetallic particles in the microstructure of AA2524 when compared to AA2024, as well as a decrease in the quantity of β-type intermetallics particles, those containing iron, even though in a lesser extent than for the S-type ones.

3.1.1.1. Age-hardenable alloys

Considering the aluminum-copper system shown in Figure 3.1, if an aluminum alloy containing 4% copper is heated to 940 °F (500 °C) and held for 1 h, the copper will form a solid solution with the aluminum. After solution heat treatment, if the alloy is quenched in cold water to room temperature, copper will be kept in solution in a stable condition. However, during the aging process, for instance at 340 °F for 10 h, very fine particles of aluminum-copper are precipitated and both the strength and the hardness greatly increase [76].

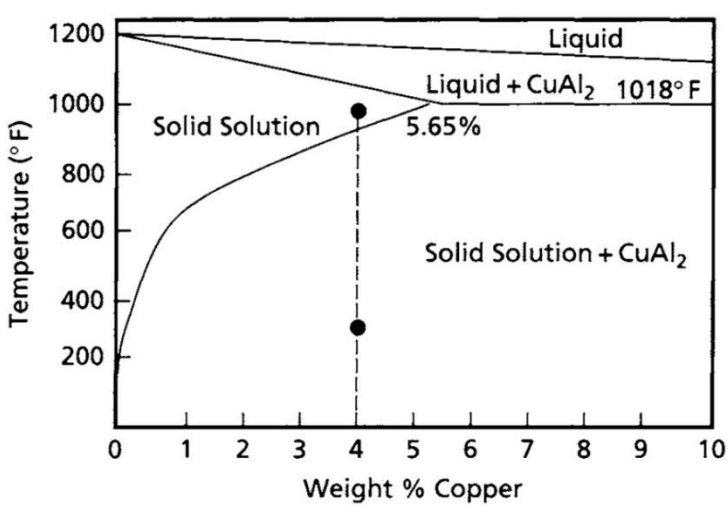

Figure 3.1 - Precipitation hardening of aluminum-copper alloy [76].

Precipitation hardening strengthens the alloy due to the formation of submicroscopic precipitates that severely strain the matrix lattice. The strengthening effect is maximized when the precipitate is coherent with the matrix. Figure 3.2 compares atomic structures with different types of precipitates.

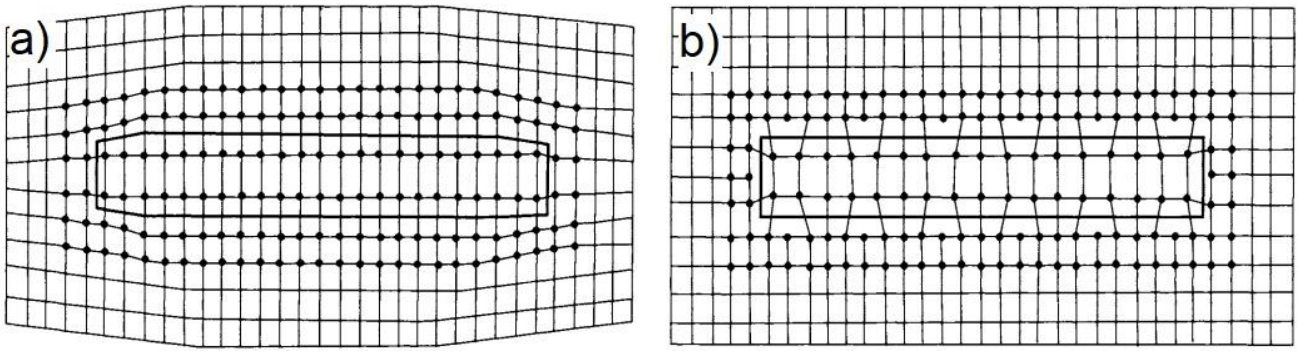

Figure 3.2 - Schematic representation of the effect of coherent (a) and incoherent (b) precipitates [76].

A coherent precipitate is observed when the atomic arrangement of both the precipitate and the matrix is the same with no discontinuity in the lattice; however, the atomic spacings are different enough to distort the crystal lattice as shown in Figure 3.2a, which is to be compared to the incoherent case presented in Figure 3.2b. This leads to increased strength by obstructing and retarding dislocation movement. In the aluminum-copper system, these solute clusters of precipitate are called Guinier-Preston (GP) zones, which are solute rich domains fully coherent with the matrix. GP zones are extremely fine presenting sizes in the range of tens of angstroms. The exact shape, size, and distribution of the GP zones depend on the specific alloy and on the thermal and mechanical history of the product. The progression of precipitation hardening in the aluminum-copper system is [76]:

Super saturated solid solution → Clustering → GP Zones → θ" → θ'→ θ

The GP zones will normally develop on aging at room temperature. During heating, the GP zones develop an intermediate precipitate (θ"), which has a tetragonal structure that forms as plate. It maintains coherency with the matrix and further increases the strain in the matrix, providing peak strength levels. On further heating, 0" is replaced by a second intermediate precipitate, θ', which is not coherent with the matrix and the strength starts decreasing. The alloy is then termed overaged. However, in the highest strength condition, both, θ" and θ', are generally present. Further heating of the alloy causes the transformation of θ' into the equilibrium precipitate θ (Al_2Cu). The progression of the aging process is shown schematically in Figure 3.3 [76].

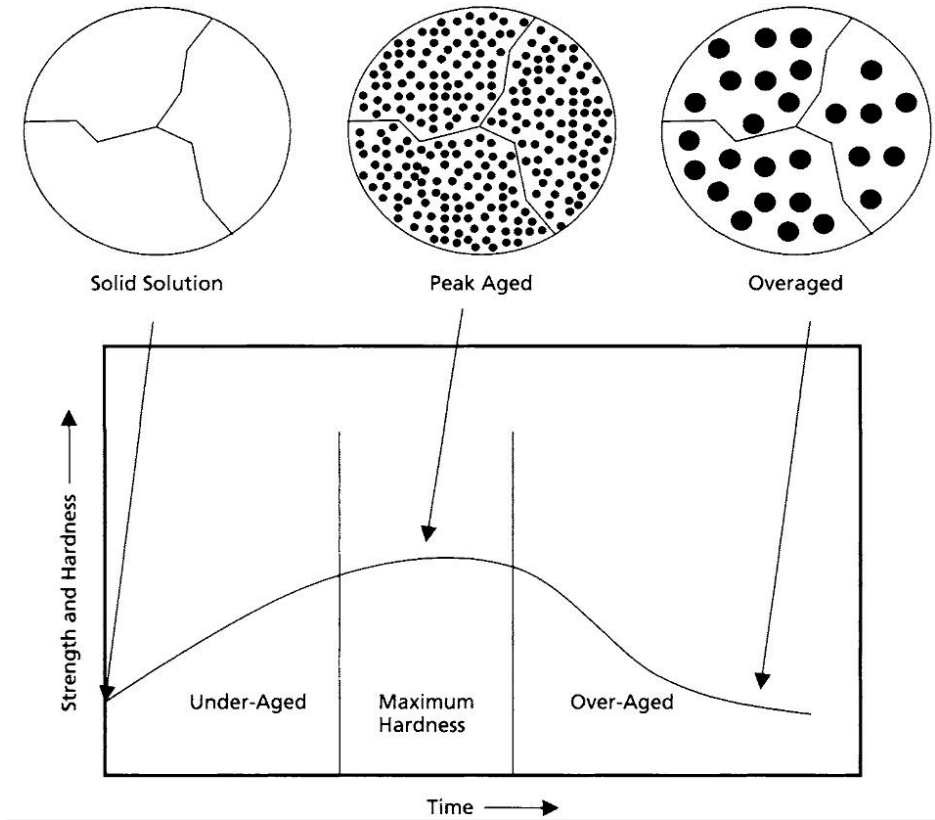

Figure 3.3 - Typical aging curve for aluminum alloys [76].

3.1.1.2. Heat treatment designation

The temper designations for aluminum alloys are shown in Table 3.2. Alloys in the as-fabricated condition are designated by an F; those in the annealed condition are designated with an O; those in the solution treated condition that have not reached a stable condition are designated with a W; and those that have been hardened by cold work are designated with an H. If the alloy has been solution treated and then aged, by either natural or artificial aging, it is designated by a T with the specific aging treatment designated by a number between 1 and 10.

Table 3.2 - Temper designation for aluminum alloys [76], [77].

Series	Treatment
T1	Natural aging
T2	Cold worked and natural aging
T3	Solution treated, cold worked and natural aging
T4	Solution treated and natural aging
T5	Artificial aging
T6	Solution treatment and artificially aging
T7	Solution treatment and overaging
T8	Solution treatment, cold working and artificial aging
T9	Solution treatment, artificial aging and cold working
T10	Cold working and artificial aging

To redistribute residual stresses after quenching, stress relief by deformation is often applied to wrought products. This makes the product less susceptible to warping during machining and improves both, fatigue strength and stress corrosion resistance.

3.1.1.3. Corrosion of aluminum-copper-magnesium (Al-Cu-Mg) alloys

Although having a low equilibrium potential, aluminum is resistant to corrosion in neutral media. This behavior is due to the formation of a thin aluminum oxide layer (Al_2O_3) on the metal surface, which is protective and inert [78]. The thickness of this oxide layer film formed in air at room temperature ranges between 2 and 3 nm [79]. However, it is adherent and compact, establishing a protective barrier between the metal and the surrounding medium. According to Pourbaix diagram [80] for pure Al, the thermodynamic stability of the aluminum oxide in aqueous systems lies in the pH range between 4 and 8. Above or below these pH values, the oxide can be dissolved exposing the base metal to aggressive media, leading to corrosion, which, in most practical cases, occurs locally, giving rise to pitting corrosion [78]. Nevertheless, the stability domain of the oxide layer is greatly affected by the presence of aggressive ions, especially chlorides, which locally destabilize the oxide layer. In the presence of such ions, aluminum is susceptible to localized corrosion even in neutral media.

Aluminum alloys can corrode by many forms: general, intergranular, exfoliation, filiform, stress-corrosion cracking, corrosion fatigue, but pitting is the main form, which, for passive metals, consists in the local breakdown of the passive layer [81]. Pitting corrosion of high strength aluminum alloys is an important issue because their structural integrity can be greatly reduced due to fatigue cracks easily nucleated at corrosion pits and can rapidly propagate under dynamic or cyclic loads [82].

During pitting formation the zones of attack are determined by the microscopic and submicroscopic characteristics of the passive layer; however, pitting can also occur in metal/environments system apparently free from heterogeneities, but containing aggressive anions, such as chloride ions in the solution [83].

The general electrochemical reactions occurring during aluminum corrosion can be represented as follows [84]:

$$Al \rightarrow Al^{3+} + 3e^- \quad (3.1)$$

$$O_2 + 2H_2O + 4e^- \rightarrow 4OH^- \quad \text{(alkaline or neutral media)} \quad (3.2)$$

$$2H^{+}+2e^{-} \rightarrow H_2 \qquad \text{(acid, deaerated media)} \quad (3.3)$$

The occurrence of the cathodic reactions (3.2) and (3.3) on the metal surface is extremely enhanced by galvanic coupling effects related to the presence of heterogeneities in the alloy's microstructure. These areas present different electrochemical potentials in relation to the matrix promoting corrosion activity. Moreover, in the vicinity of these zones, the passive film is generally less resistant, further increasing the probability of the onset of localized corrosion.

As widely documented in the literature, high strength aluminum alloys have heterogeneous microstructure due to the complex composition and thermomechanical treatments that they are submitted to optimize their mechanical properties. According to Bousquet (2011) [85], the following microstructural features are found in such alloys:

- IM particles (from 1 µm to 50 µm) - they are enriched in different alloying elements and are formed during the rapid cooling (quenching) process to which the alloys are submitted after the solution annealing.
- Dispersoid particles (from 0.02 µm to 0.5 µm) - they are formed by the precipitation of transition elements (Cr, Mn or Zr) which are insoluble in the Al matrix. Their role is to control the grain structure, delay the recrystallization process and increase the grain size. They do not contribute to hardening.
- Intergranular precipitates (between 0.1 µm and 0.4 µm) - they precipitate at the grain boundaries or at the sub-grains by diffusion of solute atoms near these regions. When this process is significant it can lead to regions depleted in alloying elements (precipitate free zones, PFZ) near the grain boundaries, which can reach few hundred nanometers.
- Strengthening precipitates (with dimensions between few nanometers and 0.1 µm) - composed of clusters of solute atoms or metastable phases, coherent or semi-coherent with the matrix. They precipitate inside the grains and contribute to matrix hardening by blocking the movement of dislocations. They can enlarge due to over-aging, causing a reduction in the hardness of the material.

Several investigations have shown that the IMs are the main responsible for the initiation of localized corrosion in high strength aluminum alloys [75], [86]–[88]. For the 2024-T3 alloy, the more studied brand of the 2XXX series, localized corrosion is initiated by dealloying of S-phase IMs (Al-Cu-Mg) and subsequent trenching of the Al matrix in their vicinity [89]. With

increasing immersion time, Al-Cu-Fe-Mn and Al-Cu-Fe-Mn-Si particles are sequentially activated [75], [90]. Due to the similarities between the composition of the IMs in the microstructure of this alloy and those in the 2524, the initiation mechanism of local corrosion activity should be the same, even though it can be expected that the susceptibility to localized attack initiation will be lower in the 2524 compared to the 2024 due to the lower content of IMs in the last alloy [66], [71]. Therefore, as high corrosion resistance is required for structural metallic materials employed in aircrafts, the high strength aluminum alloys used in the aerospace industry are protected by a multilayer system.

3.1.1.4. Electrochemical techniques applied to aluminum corrosion investigation

3.1.1.4.1. Conventional electrochemical techniques

Corrosion is a thermodynamically spontaneous process in which the metal tends to return to its lower energy state when interacting with oxidizing agents in the medium. The mechanisms of corrosion in the presence of aqueous media are of electrochemical nature and therefore can be studied by electrochemical techniques. Conventional electrochemical techniques, such as electrochemical impedance spectroscopy (EIS), anodic or cathodic polarization techniques, and open circuit potential (OCP) measurements as a function of the time of contact with the corrosive medium have been widely used in corrosion studies [91]–[94].

These techniques are very useful in studies of uniform corrosion. In cases of localized corrosion, conventional techniques have certain limitations. However, conventional electrochemical techniques have been cited in the literature in the study of these alloys. These techniques are used for characterization of oxide layer properties as well as its degradation in aggressive media, for investigation of galvanic coupling, and of the effects of mechanical and thermal processing on the corrosion behavior of these materials [95]–[99].

3.1.1.5. Friction Stir Welding (FSW)

3.1.1.5.1. FSW technique

Friction Stir Welding (FSW) is a welding method that was developed in the 1990s by The Welding Institute (TWI) in Cambridge, UK. Such technique was created to perform welding of alloys that are difficult to weld, for instance, the 2xxx series aluminum alloys. In this welding process, the temperatures reach around 80% of the melting temperature, which results in drastic reduction of defects from the solidification of the welded material, and it also provides good mechanical properties and low distortion [12].

The development of the FSW process is of great interest for the aeronautical industry, which uses rivets for joining parts made of aluminum alloys. Less than two decades ago, the Federal Aviation Administration (FAA) authorized the use of the FSW process in the manufacture of the eclipse-500 commercial jet. The use of this type of welding resulted in a reduction of approximately 60% in the amount of rivets used throughout the aircraft, thereby reducing its weight, and also reducing the time required to assemble parts using rivets by up to ten times [13].

The welding tool used in the FSW process is of the non-consumable type. It consists of the shoulder that holds the surfaces of the plates to be welded, and the tip of the tool that has a smaller diameter in relation to the shoulder and is responsible for penetrating between the plates and performing the mixing of the semi-solid zones, as illustrated in Figure 3.4.

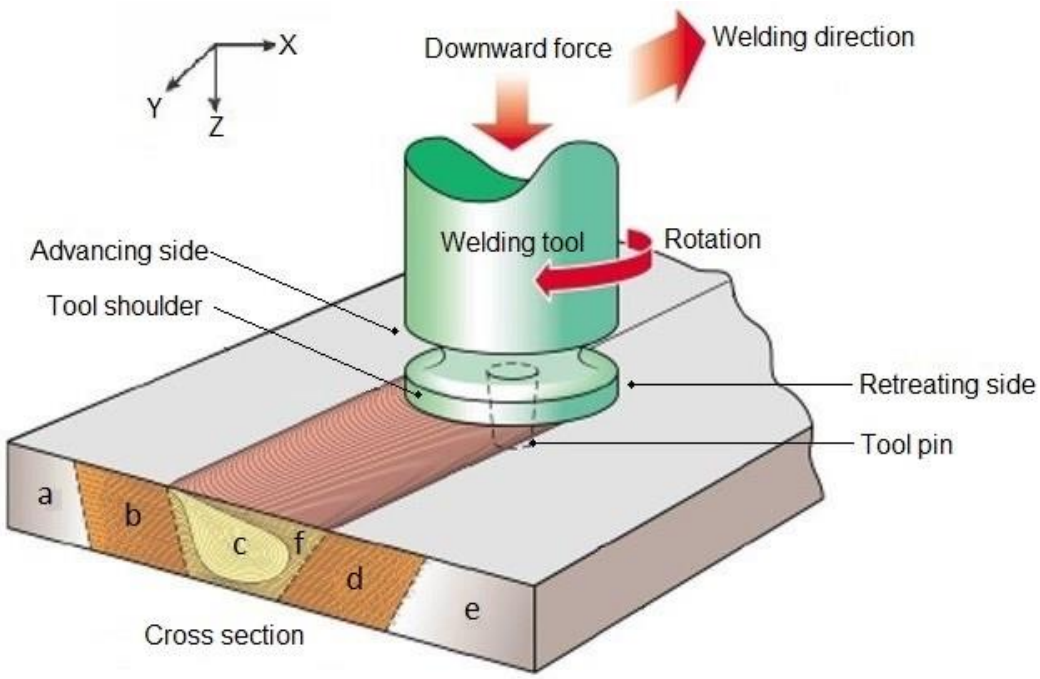

Figure 3.4 - Schematic representation of the FSW process. The letters used to designate the different zones formed along the cross section refer to the (a) advancing side base metal zone (BM-AS), (b) advancing side heat affected zone (HAZ-AS), (c) stir zone (SZ), (d) retreating side heat affected zone (HAZ-RS), (e) retreating side base metal zone (BM-RS) and (f) thermomechanically affected zone (TMAZ). Adapted from [11], [100].

3.1.1.5.2. Microstructure of aluminum alloys joined by FSW

Although the temperatures related to the FSW process are considered to be low when compared to other welding processes, it is high enough to modify the microstructure of the zones adjacent to the welded parts. Consequently, it interferes with the mechanical properties as the 2xxx series aluminum alloys depend on hardening precipitates to preserve their mechanical properties [100].

As illustrated in Figure 3.4, that shows the cross section of the welded plates, the FSW technique results in four different zones, i.e., (a/e) base metal (BM), (b/d) heat affected zone (HAZ), (f) thermomechanically affected zone (TMAZ), and (c) stir zone (SZ) or nugget [11], [14], [100], [101].

- The BM corresponds to the unaffected zone during the welding process due to its distance from the center of the weld, therefore, its microstructure is not affected.
- The HAZ presents a change in hardness in comparison to the BM and has different response to chemical attack.
- The TMAZ suffers plastic deformation from the rotation of the tool, but the recrystallization phenomenon is not observed.
- The SZ presents a microstructure composed of finely distributed equiaxial grains due to the dynamic recrystallization process. It occurs because of the deformation and the high temperatures reached during the welding process [14], [102], [103].

Differences in electrochemical behavior along the cross section of the welded joint results from FSW, and are also identified between the advancing and retreating side of the weld zone. Such differences are caused by variations in the microstructure of the alloy during the FSW process. In addition, the welding parameters also affect it [104], [105].

Bousquet et al. (2011) [103] have identified thermal gradients within the same zone, leading to variation in microhardness within the same region of the weld, and related the differences to the distribution of precipitate hardeners. Bousquet et al. (2011) [103] used transmission electron microscopy (TEM) to reveal the differences between the precipitates formed or dissolved by thermomechanical treatments during FSW welding in 2024-T3 and 7050-T651 aluminum alloys. By TEM, the authors demonstrated that the BM of the 2024-T3 alloy showed high density of dispersoids rich in Cu and Mn inside the grains, with dimensions between 200 and 500 nm and under the form of sticks. HAZ and TMAZ also presented such dispersoids inside their grains, besides fine intragranular precipitated S'(S) phase. In the nugget, those dispersoids were in smaller quantities and not evenly distributed. Moreover, coarse intragranular precipitates of S'(S) phase were observed.

3.1.1.5.3. Influence of FSW on the corrosion behavior of aluminum alloys

There are several published works in literature dedicated to the study of corrosion of aluminum alloys welded by FSW, mainly studies using high strength alloys of the aerospace industry. Several authors have reported decreased corrosion resistance of the welding zone when compared with the matrix unaffected by the welding process [103], [104], [106]. Others showed that the weld region exhibits nobler behavior than the base metal [105], [107], [108], and there are also indications of no difference between the corrosion behavior of the base metal and the welded region [99].

Differences in electrochemical behavior along the cross section of the welded sample have also been verified [109], [110], as well as due to the sense of tool rotation (advancing or retreating) in relation to the weld bead [110]. Such differences may originate from the different experimental conditions employed during FSW welding, as the parameters adopted affect the amount of applied deformation and heat generation in the welded area, and consequently the microstructure of the material [109]. It may also originate from pre- and post-treatments applied to the welded parts.

Microstructural differences also exist within the same weld zone, since the FSW process does not allow mixing of the constituents on atomic scale. However, thermal gradients occur in the weld region and can result in changes in microstructure. Bousquet et al. (2011) [103] identified variations in microhardness within the same welded area, which was related with differences in both the distribution and density of hardening precipitates in these regions.

Proton et al. (2011) [108] investigated the corrosion behavior of a FSW-welded 2050 aluminum alloy in 1 M NaCl, before and after the T8 heat treatment. The tests were performed on the cross section of the welded alloy, and electrochemical techniques and microstructural observations were employed in addition to galvanic coupling characterizations. The polarization curves showed active behavior for the base metal and all weld regions, regardless the application of heat treatment after welding. However, post-heat treatment procedure ennobled the potential of the weld zone relatively to the base metal, particularly with regard to the HAZ. This observation was obtained by galvanic coupling tests after T8 treatment, that showed cathodic behavior related to the HAZ comparatively to the SZ and the BM, while without the heat treatment the HAZ was anodic relative to SZ and BM. Regarding the type of corrosion, it was observed that the BM was susceptible to pitting corrosion while the untreated weld region was prone to intergranular and intragranular corrosion after heat treatment.

In another work, Proton et al. (2013) [111] characterized the corrosion behavior of the SZ of AA2050 welded by FSW and subjected to T8 heat treatment. Immersion, electrochemical, and gel visualization tests were used. The results of electrochemical and corrosion tests showed that the untreated SZ was susceptible to intergranular corrosion and the heat-treated to both, inter and intragranular corrosion. The gel visualization test, on the cross section of the SZ, on the other hand, showed heterogeneous behavior with the lower region of the weld being more anodic than the upper one, regardless of the heat treatment. Microstructural observations also revealed that the morphologies of corrosion related to the SZ, either with or without heat treatment, were different. This was correlated with differences in the microstructure of this region.

Fahimpour et al. (2012) [112] compared the electrochemical behavior of the AA6061 welded by FSW (800 rpm and 200 mm/min) or by TIG. The authors observed the following rank of corrosion resistance for the welded alloy: base metal > FSW > TIG. The lower corrosion resistance of the FSW weld region in relation to the base metal was explained by the larger amount of grain boundaries (smaller grains) in this region increasing its susceptibility to corrosion. For the TIG process, according to the authors, the dendritic structures with heterogeneous distribution is responsible for the low corrosion resistance. For both types of welding process, the subsequent use of T6 heat treatment resulted in corrosion resistance of the weld zone similar to that of the base metal.

Xu et al. (2011) [107] obtained opposite results to Fahimpour et al. (2012) [112], with the base metal showing higher susceptibility to pitting corrosion compared to the SZ. However, the solution used by these authors consisted of a NaOH buffer and the pH was stabilized at 12, which may have be the reason for the different results. The authors observed larger quantities of Al_2Cu phase at the base metal, impairing the formation of a protective oxide layer. The electrochemical activity related to chloride ions was greater in this region, increasing its tendency to pitting corrosion.

Bousquet et al. (2011) [103] evaluated the corrosion susceptibility of FSW-welded AA2024-T3 by the standardized intergranular corrosion test (ASTM-G110 [113]) and the use of an electrochemical microcell for open circuit potential measurements. The results from intergranular corrosion test showed that both, the BM and the different welding regions, are susceptible to intergranular corrosion, and the HAZ in the vicinity of the TMAZ was the area of highest susceptibility. Micrographic observations showed that pitting corrosion was the main

corrosion type in the BM and in the SZ. Open circuit potential measurements showed large potential fluctuations in the BM and in the HAZ in close proximity to BM, which was attributed to the stochastic characteristic of the pitting corrosion prevailing in these regions. In addition, intergranular corrosion due to a continuous line of precipitates at the grain boundaries was related to the interface between the HAZ and the TMAZ. Stable potentials were measured at the zones between the TMAZ and the SZ which was related to the uniform distribution of intermetallic particles fractured by the tool movement, resulting in a large number of small pits distributed over the surface. Regarding possible galvanic effects, the open circuit potentials related to the base metal were higher than those related to the weld affected regions.

In order to reduce the temperature rise during FSW, Jariyaboon et al. (2013) [106] investigated the effect of cryogenic carbon dioxide cooling, applied during welding, on the corrosion behavior of the 2024-T351aluminum alloy. It was found that the heat treatment did not modify the corrosion mechanism, but effectively reduced the zone susceptible to corrosion. Thus, for both conditions, with or without heat treatment, the HAZ was anodic in relation to the BM and the SZ, although the MB also showed anodic activity. SEM observations of the welded cross section after immersion tests showed intergranular corrosion in the HAZ and SZ, which was attributed to the Cu-depleted zones at the grain boundaries, and pitting corrosion around the intermetallic particles in the BM. It was also found that the SZ presents heterogeneous electrochemical activity. The lower region (root of the weld) of the sample welded without cooling was anodic, and the regions near the end of the SZ, on the retreating side, for the sample welded with cooling. It was also observed that the density of cathodic sites was higher in the SZ region than in the BM. This was due to precipitation of S-phase particles in this region, which act as cathodes.

Squillace et al. (2004) [114] evaluated the susceptibility to corrosion of the FSW-welded regions of the aluminum alloy AA2024-T3 by polarization curves and electrochemical impedance tests . They found that the base metal was more prone to corrosion than the SZ and HAZ, which were passive.

There are few papers in literature that report on the effects of welding parameters, more specifically welding and rotation rate, on the mechanical and corrosion properties of aluminum alloys welded by FSW. Jariyaboon et al. (2007) [115] found that the welded region (HAZ + TMAZ + SZ) behaves anodically with respect to the matrix. Also, the zones preferentially anodic shifts from the SZ to the HAZ when the tool rotation speed increases. This behavior was related

to dissolution and reprecipitation of dispersoid particles and hardening due to the thermal cycles imposed by welding. Concerning the corrosion behavior of the individual areas, investigated by polarization tests using a microcell, it was found that the pitting potential increased with increasing tool displacement speed when keeping constant the tool rotation speed. Increasing rotation speed, keeping the displacement speed constant, whereby the effect of the rotation speed seems to play a more important role in this parameter. On the other hand, the results of the cathode curves did not allow any direct correlation between the variation of welding parameters and the reduction reaction rate.

Regarding the zones formed during the friction stir welding process with a non-consumable pin and the complexity of their microstructures, both, for similar and dissimilar alloys, new studies on the corrosion behavior of these joints will bring important information about the mechanisms of corrosion of FSW-welded aluminum alloys.

3.2. Magnesium

Many studies have been carried out since the 1920s on Mg corrosion. For example, a 1926 report by Boyer ("National Advisory Committee for Aeronautics" - NACA) concerning the corrosion of Mg and its alloys [116]. This report indicated that the electrochemical potential of Mg is highly negative and that hydrogen release is observed until a film of corrosion products appears, which has the effect of reducing the electrode potential of the metal. These first observations were subsequently complemented, and several models of Mg corrosion mechanisms were developed, some of which are still under debate.

3.2.1. Kinetic aspect: the negative difference effect (NDE) and current reaction mechanisms

A phenomenon known as negative difference effect, NDE, is observed during the corrosion of pure Mg. This phenomenon is characterized by an increase of hydrogen evolution, as well as an anomalous high dissolution rate, during anodic polarization of pure Mg [117]. These experimental results have led to the development of several mechanisms to explain the corrosion behavior of pure Mg.

3.2.1.1. Model based on the existence of a monovalent ion

Song et al. (1997) [118] proposed a model based on the existence of a monovalent Mg^{+} type reaction intermediate. Then, BARIL et al. (2007) [53] proposed a mechanism in which the monovalent ion Mg^{+}, resulting from the oxidation of Mg, is adsorbed on the surface of the

electrode (Eq. (3.5)). The adsorbed Mg (Mg^{+}_{ads}), similar to adsorbed intermediate observed in the iron corrosion process, can then be oxidized to Mg^{2+} (Eq. (3.6)), or allow the release of dihydrogen by a chemical reaction with water (Eq. (3.7)). For cathodic overpotential with respect to the corrosion potential, hydrogen release can also occur depending on the water reduction reaction (Eq. (3.8)). Thus, the overall reaction Eq. (3.4), which express as:

$$Mg + 2H_2O \rightarrow Mg^{2+} + 2OH^- + H_2 \quad \text{(Overall reaction)} \tag{3.4}$$

can be split into the following elementary reactions:

$$Mg \xrightarrow{k_1} Mg^{+}_{ads} + e^- \quad \text{(Partial anodic reaction)} \tag{3.5}$$

$$Mg^{+}_{ads} \underset{k_{-2}}{\overset{k_2}{\rightleftharpoons}} Mg^{2+} + e^- \quad \text{(Partial anodic reaction)} \tag{3.6}$$

$$2Mg^{+}_{ads} + 2H_2O \xrightarrow{k_3} 2Mg^{2+} + 2OH^- + H_2 \quad \text{(Chemical reaction, NDE)} \tag{3.7}$$

$$2H_2O + 2e^- \rightarrow 2OH^- + H_2 \quad \text{(Cathodic reaction)} \tag{3.8}$$

$$Mg^{2+} + 2OH^- \rightarrow Mg(OH)_2 \quad \text{(Corrosion product formation)} \tag{3.9}$$

$$MgO + H_2O \rightleftharpoons Mg(OH)_2 \quad \text{(Equilibrium MgO-Mg(OH)}_2\text{)} \tag{3.10}$$

Depending on the initial pH, in aqueous media, the pH of the solution increases and stabilizes at about 10, after 2 hours of immersion, following the proposed mechanism (Eq. (3.7)) [50]. According to the model described above, the production of Mg^{+} ions and the cathodic hydrogen release reaction take place preferentially at the interface, in areas not covered by the film, i.e., free of a partially protective corrosion product film (Eqs. (3.9) and (3.10)). The chemical production of hydrogen is accompanied by the production of Mg^{2+} and hydroxide ions, which increase concomitantly with the applied overpotential [16], [40], [53], [118]–[120].

It is important to highlight that the existence of Mg^{+} species in the reactions between Mg and water is still controversial and no experimental evidence of its presence has been provided

so far [18]. The presence of the monovalent ion (Mg^{+}) was firstly assumed by Petty et al. (1954) [121].

Samaniego et al. (2014) [122] reproduced the experience of Petty et al. (1954) [121] using *in situ* Raman spectroscopy techniques, but did not come to the same conclusions. The authors demonstrated the presence of other reducing agents in solution, which may invalidate the conclusions of the original article by Petty et al. (1954) [121].

BARIL et al. (2007) [53] obtained good correlation between their experimental impedance diagrams (Figure 3.5a and Figure 3.5b) and that resulting from calculation and simulation (Figure 3.5c) by taking into account that Mg^{+}_{ads} follows the Langmuir isotherm and that the kinetic constants of electrochemical reactions follow the Tafel laws. It should be mentioned that this approach involving adsorbed intermediates accounting for capacitive or inductive time-constants has already been validated in the case of the iron dissolution, but also invoked for the dissolution of other metals such as zinc.

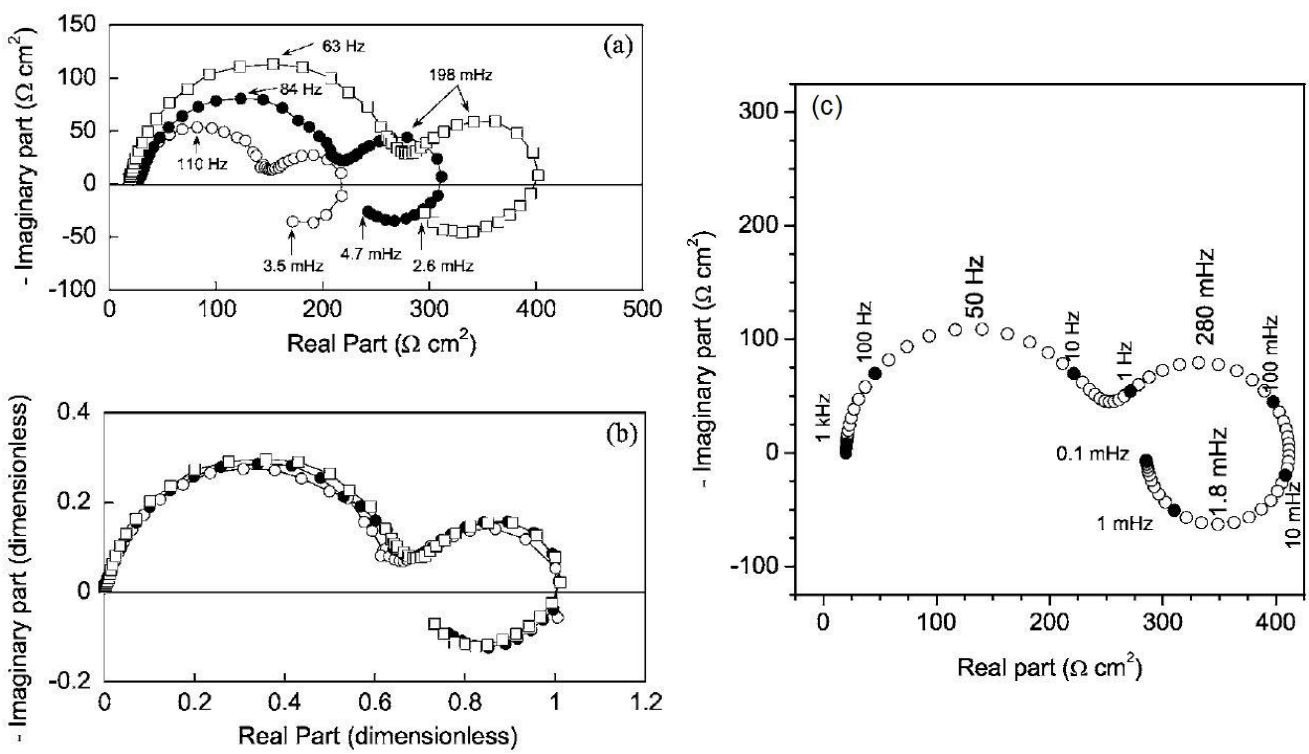

Figure 3.5 - a) Electrochemical impedance diagrams plotted after different hold times of pure Mg in 0.1 M Na_2SO_4 solution at E_{corr} with an electrode rotation rate of 240 rpm: (∘) 1 h 30 min, (•) 21 h and (□) 32 h; b) normalized impedance diagrams, and c) simulated impedance diagram using a proposed kinetic model [53].

The equivalent electric circuit presented in Figure 3.6 shows a schematic representation of the magnesium-electrolyte interface, following the proposed kinetic model [53] where R_e is

the electrolyte resistance, Z_f is the faradaic impedance in parallel with the double layer capacitance, C_d. R_f and C_f, are the resistance and capacitance of the oxide film (MgO), respectively. R_f is assumed to be very large in comparison to Z_f and C_d larger than C_f.

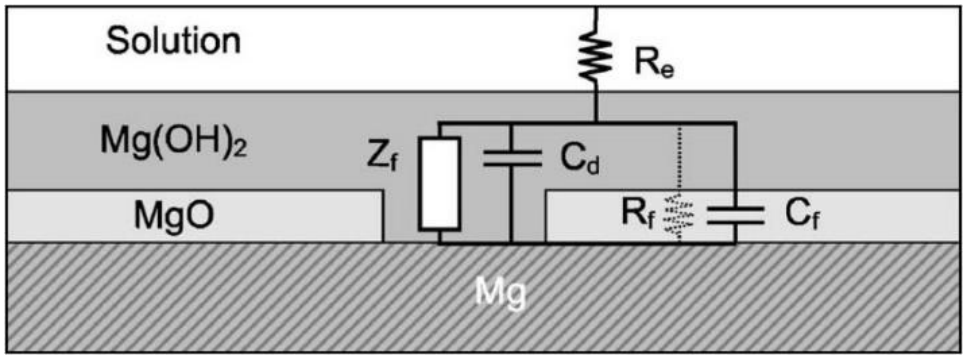

Figure 3.6 - Schematic representation of the interface and the equivalent circuit [53].

At this point, it is also worth mentioning that some recent works modelling the magnesium-electrolyte interface using density functional theory (DFT) have been reported [123], [124]. It has been shown that the water reduction reaction follows a Volmer-Heyrovsky mechanism (Eqs. (3.11) and (3.13)), rather than a Volmer-Tafel mechanism (Eqs. (3.11) and (3.12)). This reaction would be favoured in the presence of $\mathrm{OH_{ads}}$ species.

$$\text{Volmer:} \quad \mathrm{H^+ + e^- \rightleftharpoons H_{ads}} \tag{3.11}$$

$$\text{Tafel:} \quad \mathrm{2H_{ads} \rightleftharpoons H_2} \tag{3.12}$$

$$\text{Heyrovsky:} \quad \mathrm{H_{ads} + H^+ + e^- \rightleftharpoons H_2} \tag{3.13}$$

This theoretical approach may be of interest for the detection of $\mathrm{Mg^+_{ads}}$ species, which has never been reported experimentally.

3.2.1.2. Model based on the existence of a cathodic film

Several authors have proposed to explain the NDE by the existence of a film of corrosion products having a cathodic role at uncovered areas, often called "dark corrosion film" [27]. This film which is formed during immersion in an electrolyte would be the primary source of hydrogen release, associated with a high corrosion rate (NDE) [26]. This model is based on active

corrosion products and impurities that would be the site of the cathodic reactions. Several authors have noted higher cathodic activity on pure Mg samples previously anodically polarized and covered with a corrosion product film than on samples that have not undergone this procedure.

Williams et al. (2015) [125] showed that cathodic activity was mainly located at the interface between the corrosion product film, the region not covered by it, and the electrolyte. The measured cathodic currents were ten times higher for a Mg sample containing 280 ppm of Fe impurities than for a sample with a level of Fe below 80 ppm. These authors showed that the concentrations of iron impurities and electrolyte (NaCl) have an important impact on the morphology of the corrosion product film. In solutions of high NaCl concentration, a disc shape corrosion product was observed, while in those of low NaCl contents, a corrosion-filiform propagation was seen (Figure 3.7).

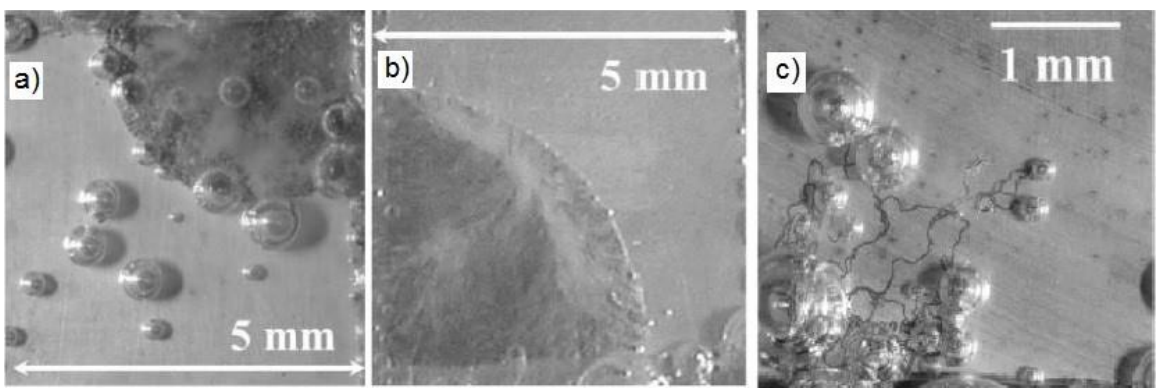

Figure 3.7 - Optical micrographs taken in situ of a corroding pure Mg (99.9 wt.%, 280 ppm of Fe) after 40 min in a NaCl solution at pH 6.5 with concentrations of a) 1 M, b) 0.1 M and c) 10^{-2} M [125].

The release of hydrogen is correlated with the increase in anodic polarization but does not seem to be correlated with the quantity of corrosion products [26]. Enrichment of the film with metallic particles of impurities (often Fe) has been suggested as an explanation for its high cathodic activity. Cain et al. (2015) [126] highlighted this enrichment using the Rutherford backscattering spectrometry technique. Frankel; Fajardo; Lynch, (2015) [27] distinguished three sources of hydrogen release ($\mathrm{HE_{total}}$) from corrosion product film ($\mathrm{HE_{film}}$), impurities ($\mathrm{HE_{impurities}}$) or anodic sites (uncovered Mg) ($\mathrm{HE_{anode}}$), as shown in Eq. (3.14) and Figure 3.8.

$$\mathrm{HE_{total}} = \mathrm{HE_{anode}} + \mathrm{HE_{film}} + \mathrm{HE_{impurities}} \tag{3.14}$$

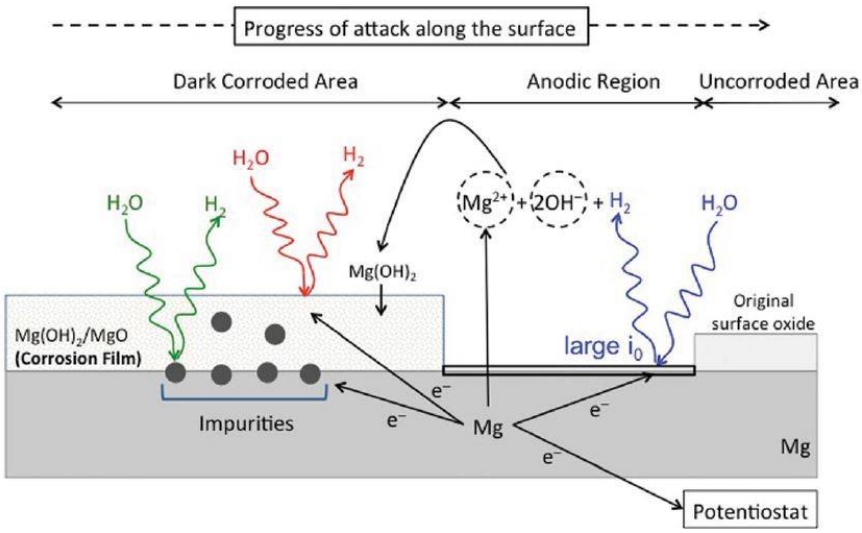

Figure 3.8 - A schematic representation of the anodic hydrogen evolution process that distinguishes the contribution of corrosion film, accumulated impurities, and anodic area [27].

However, it has been shown that the enrichment of the film by impurities itself cannot explain the NDE [127], [128]. Fajardo et al. (2015; 2016) [31], [129] showed on an ultra-pure sample (99.9999% Mg) that the film and the impurities trapped in it were only a small part of the NDE, as shown in Figure 3.9. The authors calculated the current from the corroded areas based on the total hydrogen released and the plot of previously acquired current-voltage curves on polarized samples. It can be seen in Figure 3.9 that the NDE is mainly associated with localized anodic reaction in uncovered areas. Indeed, only a small fraction of the total current is attributed to the reactivity related to impurities or film. Besides, Fajardo et al. (2015; 2016) [31], [129] highlighted the phenomenon on a sample almost free of impurities (≅ 1 ppm).

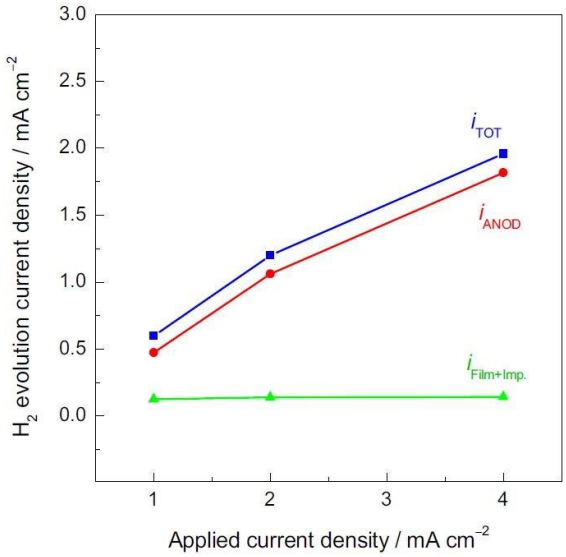

Figure 3.9 - Hydrogen evolution current density plotted as a function of the applied anodic current density. The experiment was performed in a galvanostatic polarization mode (i_{TOT}), and the contribution of hydrogen released from uncovered areas (i_{ANOD}) or covered by a film of corrosion products ($i_{Film+Imp}$) was calculated [129].

3.2.2. Corrosion product film

Taheri; Danaie; Kish (2014) [130] studied ultra-pure Mg sample previously immersed for 24 h in 0.01 M NaCl solution by SEM-EDS and STEM. The authors highlighted that the film consisted of a thin layer of partially hydrated MgO on the metal substrate, formed by contact with air after polishing procedure. A thicker and more porous $\mathrm{Mg(OH)_2}$ layer is formed above the first oxide layer, seemingly by the interaction of the oxide layer with water.

EDS analysis revealed the presence of chloride ions in the porosity of the outer film. Figure 3.10a shows the morphology of the film. Its total thickness is between 350 nm and 700 nm, according to Taheri; Danaie; Kish (2014) [130]; the thickness of the internal layer of MgO is 3-5 nm, thinner than earlier reported (20-40 nm) by Nordlien et al. (1997) [131]. The evolution of the O/Mg ratio shown in Figure 3.10b allows identifying an area of a few tens of nanometers with a ratio close to 1 (MgO) near to the metal. Then, a layer with a ratio close to 2 ($\mathrm{Mg(OH)_2}$) on top of the previous layer.

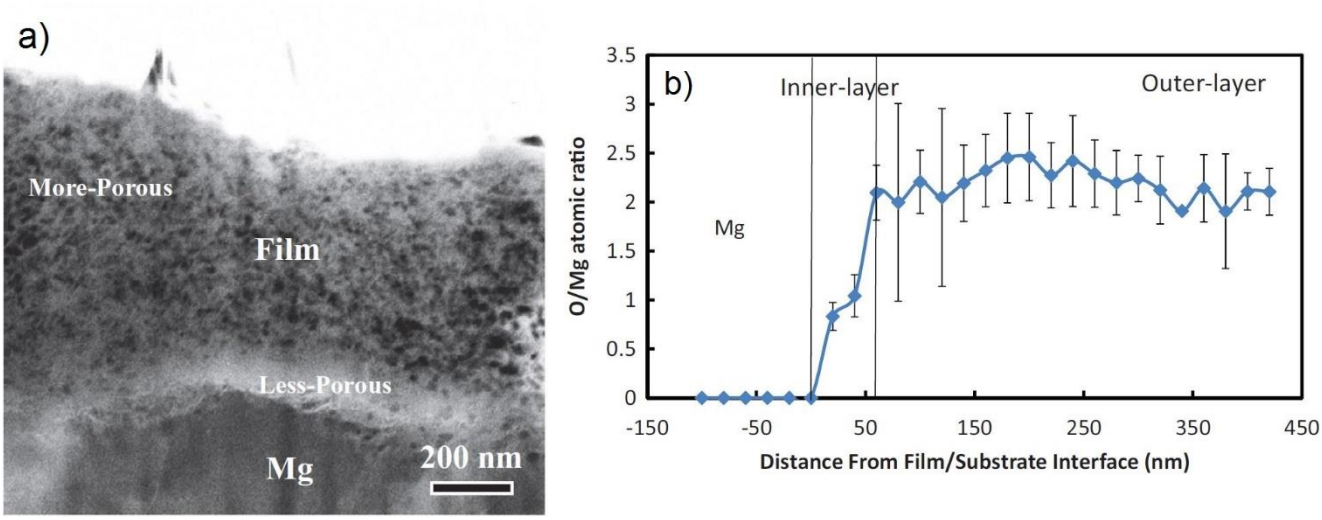

Figure 3.10 - a) STEM micrograph and b) depth profile showing the O/Mg atomic ratio across the Mg/oxide film interface formed during conditioning at E_{corr} in 0.01 M NaCl for 24 h [130].

Brady et al. (2015) [132] studied the formation of a corrosion product film on Mg alloys by small-angle neutron diffraction. They showed that immersion in 5 wt.% NaCl solution leads to the formation of a porous film of $\mathrm{Mg(OH)_2}$ which has a large specific surface area, estimated at 4-40 $m^2.g^{-1}$ by BET method.

3.2.3. Determination of the corrosion rate

The corrosion rate of pure Mg and its alloys can be determined either by mass loss, by analysis of the amount of $\mathrm{Mg^{2+}}$ ions in solution, by measuring the quantity of $\mathrm{H_2}$ released, or

by electrochemical measurements (polarization curves and EIS) [18]. The presence of several reactions, particularly in the anodic domain (oxidation possibly in two steps coupled with chemical reactions, presence of a protective film), makes difficult the estimate of Tafel coefficients and corrosion rate by Stern-Geary's law [24], [133]. Indeed, Keddam [134] showed that as soon as the electrochemical mechanism can be split into elementary steps, one of which involving adsorbed intermediates, the use of Stern and Geary relationship must be used with a great care.

In addition, the presence of the chemical reaction that causes the NDE (Eq. (3.7)) leads to underestimated corrosion rates by electrochemical measurements [24], [135]–[137]. Qiao et al. (2012) [137] studied the corrosion resistance of high-purity Mg in NaCl 3.5% saturated with $\mathrm{Mg(OH)_2}$. These authors concluded that the corrosion behavior was consistent with the uni-positive $\mathrm{Mg^+}$ ion corrosion mechanism, particularly because the corrosion rate measured using electrochemical techniques was consistently lower than that measured independently, either by weight loss or hydrogen evolution, as predicted by the presence of univalent $\mathrm{Mg^+}$ species for the Mg corrosion mechanism.

Figure 3.11 shows instantaneous corrosion rates determined by hydrogen release (P_H), polarization curves (P_i) or by EIS measurements ($P_{i,EIS}$). The authors showed that the corrosion rates estimated by electrochemical techniques are always lower than those determined by measurements of $\mathrm{H_2}$ released.

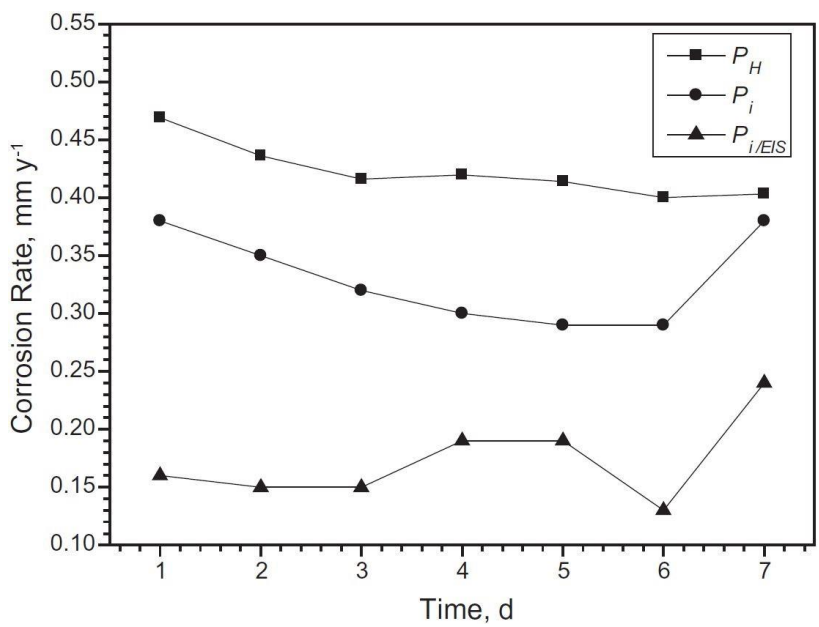

Figure 3.11 - Instantaneous corrosion rate determined from hydrogen evolution, $\mathrm{P_H}$, from the corrosion current density from the polarization curve, $\mathrm{P_i}$, and from EIS, $\mathrm{P_{i/EIS}}$, for the high purity Mg plotted versus immersion time in 3.5% NaCl saturated with $\mathrm{Mg(OH)_2}$ at 25 °C [137].

Several authors [33], [54], [138] indicated that the use of polarization resistance, R_P, is preferred to the use of charge transfer resistance R_T in the Stern-Geary equation. It leads to a good correlation between the corrosion rates determined by all methods above. However, these authors used a model to estimate R_P values, which could result in underestimated values (significant dispersion at low frequency) and lead to inaccurate estimation of the corrosion rate. Besides, Silverman (1989) [139] clarified that in the case of systems that have an inductive loop due to the presence of adsorbed species, the use of R_T in the Stern-Geary equation was recommended. Here again, in the case of complex mechanism, Keddam [134] has shown that the corrosion behavior is better evaluated by the charge transfer resistance than the polarization resistance.

4. MATERIALS AND METHODS

4.1. Materials

4.1.1. Aluminum

The 2524-T3 aluminum alloy in the form of plates used in this work was provided by EMBRAER S.A. The chemical composition of this alloy is shown in Table 4.1. The compositional values were obtained by means of inductively coupled plasma - optical emission spectrometry (ICP-OES) technique performed at the Chemistry Institute of the University of São Paulo. All the samples used in this work were cut from the same sheet.

Table 4.1 - Chemical composition (wt.% or ppm) obtained by inductively coupled plasma - optical emission spectrometry (ICP-OES) of the aluminum alloy 2524 used in this study.

Sample	Al (%)	Cu (%)	Mg (%)	Mn (%)	Fe (ppm)	Zn (ppm)	Ti (ppm)	Si (ppm)
AA2524	94.06	4.17	1.35	0.56	757	291	274	137

4.1.2. Magnesium

The material used in this part of the study was a Mg rod (5 mm in diameter) with a purity of 99.9% purchased from Goodfellow. The impurity contents of the commercially pure Mg used in this study (composition by the provider) are shown in Table 4.2.

Table 4.2- Impurity quantities (ppm) of the commercially pure magnesium used in this work (Goodfelow).

Element	Al	Cu	Fe	Mn	Ni	Si	Zn
(ppm)	70	20	280	170	10	50	<20

4.2. Methods

The experiments performed along this work were divided into three main parts: microstructural characterization, corrosion tests, and electrochemical characterization. The organization scheme and description of all tests performed are presented in Figure 4.1.

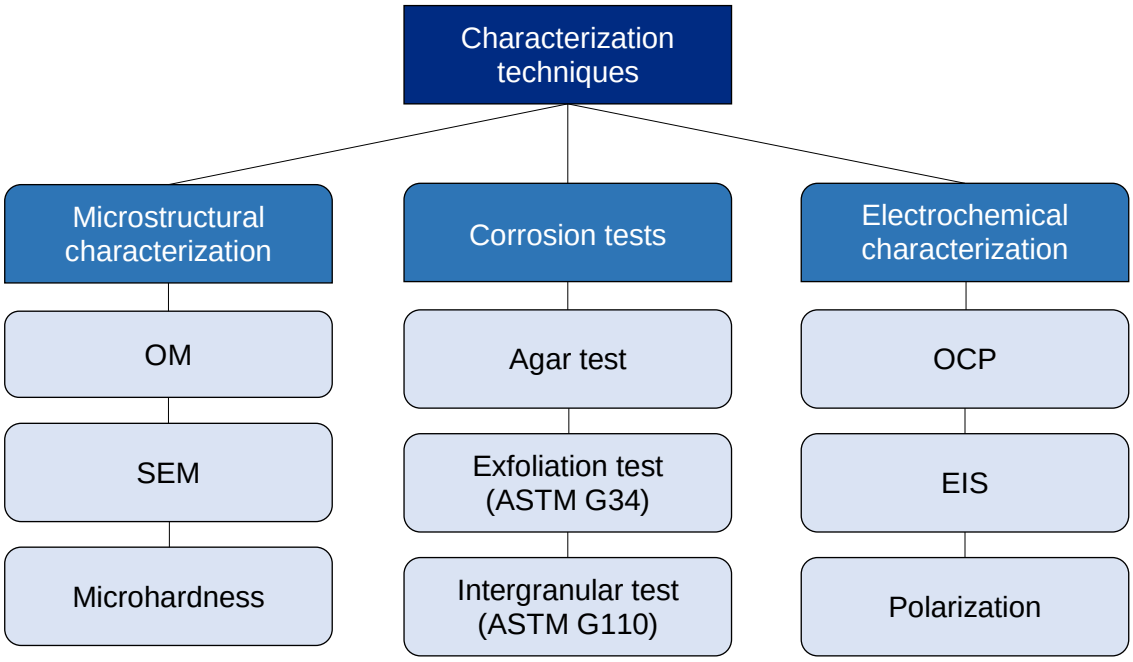

Figure 4.1 - Organization scheme and description of all tests performed.

4.2.1. Aluminum

4.2.1.1. Friction Stir Welding (FSW)

FSW of the AA2524 was performed at the National Center for Research in Energy and Materials (CNPEM) - National Laboratory of Nano Technology (LNNano). A welding tool made of AISI H13 steel was used. The diameters of the shoulder and pin were 10.97 mm and 3.80 mm, respectively, and pin height 1.25 mm. The welding parameters were as follows: penetration depth: 1.18 mm, angle of tool inclination: 0º, rotation: 1,200 rpm in counterclockwise direction, advancement speed: 150 mm/min and axial force of 4 kN.

4.2.1.2. Microstructural characterization

4.2.1.2.1. Sample preparation

The aluminum alloy surfaces were prepared according to conventional metallographic techniques, consisting of mechanical polishing with silicon carbide paper (SiC) with different grain sizes (P320, P500, P800, P1200, P2400 and P4000), and polishing with 3 µm and 1 µm diamond suspension. Depending on the test performed, different surface finishes were used.

4.2.1.2.2. Optical Microscopy (OM)

The samples were prepared according to the metallographic techniques described previously. The microstructure was revealed after attack with a solution composed of 25% (vol.)

HNO_3 and 2% (vol.) HF in distilled water. A LEICA EC3 camera coupled with the LEICA DMLM optical microscope was used to observe the surface.

4.2.1.2.3. Scanning Electron Microscopy (SEM)

Scanning electron microscopy (SEM) and chemical analysis by energy dispersive X-ray spectroscopy (EDXS) were employed for different samples. Information on grain and surface morphology, and analysis of the chemical composition of the micrometric particles were obtained. Different electronic microscopes were used, depending on the availability and resolution of each one, namely:

- Bench Scanning Electron Microscope Hitachi - TM3000;
- Scanning electron microscope coupled with field emission gun (SEM-FEG) JEOL - JSM-6701F;
- Scanning electron microscope JEOL - JSM-6010L.

4.2.1.3. Corrosion tests

4.2.1.3.1. Exfoliation corrosion test (ASTM G34)

The exfoliation corrosion test followed the standard ASTM G34 [140]. The samples were immersed in a solution of 4 M NaCl, 0.5 M KNO_3 and 0.1 M HNO_3 diluted in H_2O up to 1 L of solution, for 48 hours. According to the standard test, the volume of the test solution should follow the ratio of 30 mL of solution to 1 cm^2 of sample exposed area. After the test, the samples were cut in the cross section and analyzed by OM and SEM.

4.2.1.3.2. Intergranular corrosion test (ASTM G110)

The intergranular corrosion test followed ASTM G110-97 [113]. The samples were cleaned in a solution of 945 mL of distilled H_2O, 50 mL of HNO_3 (70%) and 4 mL of HF (48%) for 1 minute at 93 ºC. Then, the samples were exposed to a HNO_3 solution (70%) at room temperature for 1 minute and, subsequently, washed and air-dried. Finally, the samples were exposed to the test solution for 6 hours at ambient temperature. After the test, the samples were air dried and cut in the cross section to be analyzed by OM and SEM.

4.2.1.3.3. Agar-agar test

The agar-agar test is a qualitative analysis that aims at observing the change of the pH on the surface of samples as a function of corrosion time when exposed to aggressive media. In this work, the samples were exposed to a solution composed of 0.6 M NaCl, 0.3 g agar-agar and 1 mL of universal indicator in 10 mL of H_2O, heated at 100°C. The NaCl concentration of

this test was relatively high (0.6 M) in order to accelerate the corrosive processes and the appearance of the corrosion effects on pH in a short time. In this test, due to hydrolysis promoted by the aluminum ions in the anodic regions (Eq. (4.1)), the agar becomes orange in color. In the cathodic regions, in turn, the generation of hydroxyl ions occurs as a consequence of oxygen reduction (Eq. (4.2)), resulting in the green/blue coloration [141].

$$Al^{3+} + H_2O \rightarrow Al(OH)^{2+} + H^+ \qquad \text{Eq. (4.1)}$$

$$O_2 + 2H_2O + 4e^- \rightarrow 4OH^- \qquad \text{Eq. (4.2)}$$

4.2.1.3.4. Vickers microhardness

Vickers HV 0.3 microhardness test, with 30 gf load, was performed using a Shimadzu microhardness tester. Microhardness measurements were performed along the sample top surface from the BM-RS in the direction to the BM-AS of the FSW-welded 2524-T3 aluminum alloy. A graph of the microhardness profile of the different zones formed after FSW was obtained with the indentations results.

4.2.2. Magnesium

4.2.2.1. Sample preparation

The lateral part of the pure Mg cylinder was insulated with a cataphoretic paint and, in sequence, with an epoxy resin leaving a surface area of disk electrode corresponding to 19.6 mm^2 for exposure to the test solution. Before the electrochemical tests, the electrode was ground with successive SiC abrasive papers, down to grit P4000.

4.2.2.2. Experimental setup

All the experiments were performed using a rotating disk electrode (RDE). The electrode rotation rate was fixed at 1000 rpm, but different rotations were also used. During the experiments the temperature was maintained at (25.0 ± 0.1) °C by means of a double-walled cell connected to a cryostat to regulate the temperature. The electrolyte was in contact with air and the experiments were performed in 0.1 $mol.L^{-1}$ Na_2SO_4 electrolytic solution (pro analysis grade) with an initial pH of 5.6. The reference and the counter electrodes were a mercury sulfate electrode (MSE) in a saturated potassium sulfate solution (E_{MSE} = 0.64 V/SHE) and a platinum gauze of large surface area, respectively.

4.2.3. Electrochemical techniques

4.2.3.1. Conventional electrochemical techniques

4.2.3.1.1. Open circuit potential (OCP) measurements

In order to verify the potential stabilization time of the studied materials, open circuit potential measurements were performed. The tests were carried out using the potentiostat Gamry Ref 600+ or Autolab, both connected to a microcomputer and controlled through the software of the respective manufacturers.

4.2.3.1.2. Potentiodynamic polarization (Polarization)

For the magnesium rod, potentiodynamic polarization curves, anodic and cathodic, were obtained separately (two independent measurements) after a preliminary hold time of 2 h at the corrosion potential (E_{corr}). The potential sweep rate was fixed at 0.167 $mV.s^{-1}$. The polarization curves were corrected considering the ohmic drop, experimentally determined from the high-frequency limit of the impedance diagrams.

4.2.3.1.3. Electrochemical impedance spectroscopy (EIS)

The global impedance diagrams were obtained in potentiostatic mode, with 10 mV_{rms} or 20 mV_{rms} of amplitude perturbation, for Mg and Al, respectively and with 8 points per decade in both cases. The linearity was checked by varying the amplitude signal for each material. At least two experiments were performed. The consistency of the obtained impedance diagrams were always checked with the Kramers-Kronig relations [142], [143]. The equipment used were the same as those defined in 4.2.3.1.1. As well as for the OCP and polarization curves, tests were performed on samples of pure magnesium and on 2524-T3 aluminum alloy, with and without welding, which allowed the comparison of the respective behaviors.

5. RESULTS AND DISCUSSION

5.1. Aluminum

5.1.1. Microstructural characterization

5.1.1.1. Microstructure of AA2524-T3 welded by FSW

The temperatures reached during the FSW process are comparatively low in relation to those of other welding processes, however, they were high enough to modify the microstructure of the zones adjacent to the welded plates. Consequently, it interferes with the mechanical properties of the material as the 2xxx series aluminum alloys rely on hardening precipitates to maintain their mechanical properties [100].

Differences in electrochemical behavior can be detected along the cross section of the welded joint, as well as with respect to the advancing or retreating rotational movement of the welding tool. Such differences are caused by changes in the microstructure of the alloy during FSW. In addition, the welding parameters also have significant effect on such behavior [104], [105].

Furthermore, the FSW process is asymmetric and introduces different degrees of deformation and temperature peaks on both sides of the weld bead, retreating and advancing sides. The advancing side (AS) of the weld is subjected to higher temperatures compared to the retreating side (RS), thus the microstructural modifications are always different on both sides [144], [145].

Figure 5.1 shows optical micrographs of the different zones formed along the cross section of FSW-welded 2524-T3 aluminum alloy after metallographic preparation (4.2.1.2.1), followed by chemical etch for 7 seconds in a solution of 25% (vol.) HNO_3 and 2% (vol.) HF, diluted in distilled water. It is possible to observe the different zones of the alloy after FSW: (1) base metal (BM), heat affected zone (HAZ), and thermomechanically affected zone (TMAZ) ,on the retreating side (RS); (2) stir zone (SZ); and (3) base metal (BM), heat affected zone (TZA) and thermomechanically affected zone (TMAZ) on the advancing side (AS).

The BM corresponds to the unaffected zone during the welding process due to its distance from the weld center, so its microstructure was maintained without change.

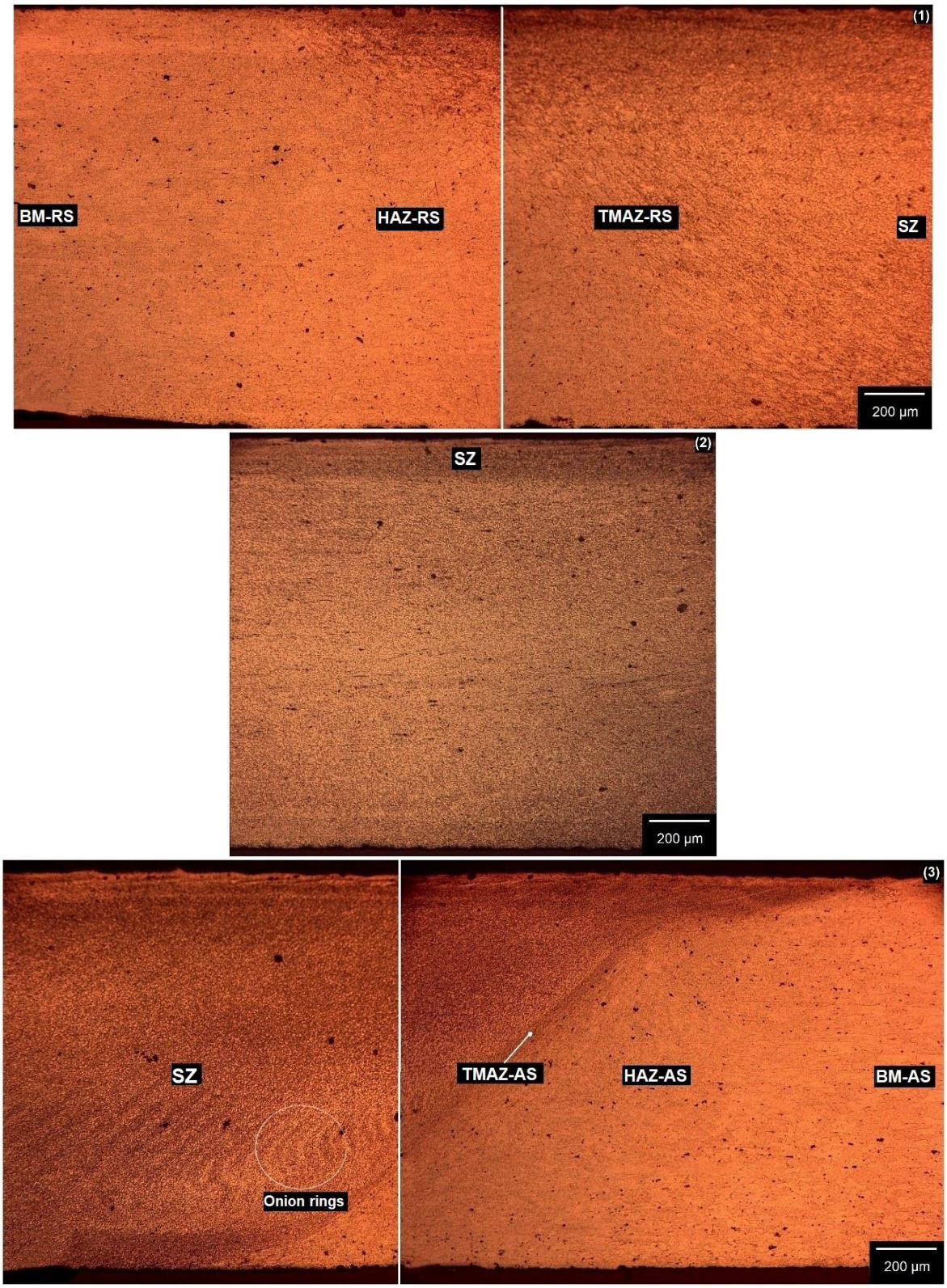

Figure 5.1 - Optical micrographs of FSW-welded 2524-T3 alloy after chemical etch in 25% (vol.) HNO_3 and 2% (vol.) HF solution in distilled water for 7 seconds. It shows the different zones after the welding process: (1) base metal (BM), heat affected zone (HAZ) and thermomechanically affected zone (TMAZ) on the retreating side (RS); (2) stir zone (SZ); and (3) base metal (BM), heat affected zone (HAZ) and thermomechanically (TMAZ) affected zone on the advancing side (AS).

Observation of the optical micrographs in Figure 5.1 shows that the HAZ does not exhibit significant microstructural differences compared to the BM, although it shows difference in hardness values and a different response to chemical attack from the BM. It is also seen that the TMAZ suffers plastic deformation due to tool rotation, but the recrystallization phenomenon is not observed. Also, the SZ presents a microstructure composed of finely distributed equiaxial grains, due to dynamic recrystallization. It occurs because this region is subject to greater deformation and temperature during the welding process [14], [102], [103].

5.1.1.2. Microhardness test

Microhardness measurements were performed along the top surface of the sample. Hardness is one of the properties most affected when there are microstructural differences, due to the different zones formed during FSW, such as changes in grain size and precipitation or dissolution of hardening precipitates. The microhardness profile of the AA2524-T3 FSW-welded sample is shown in Figure 5.2.

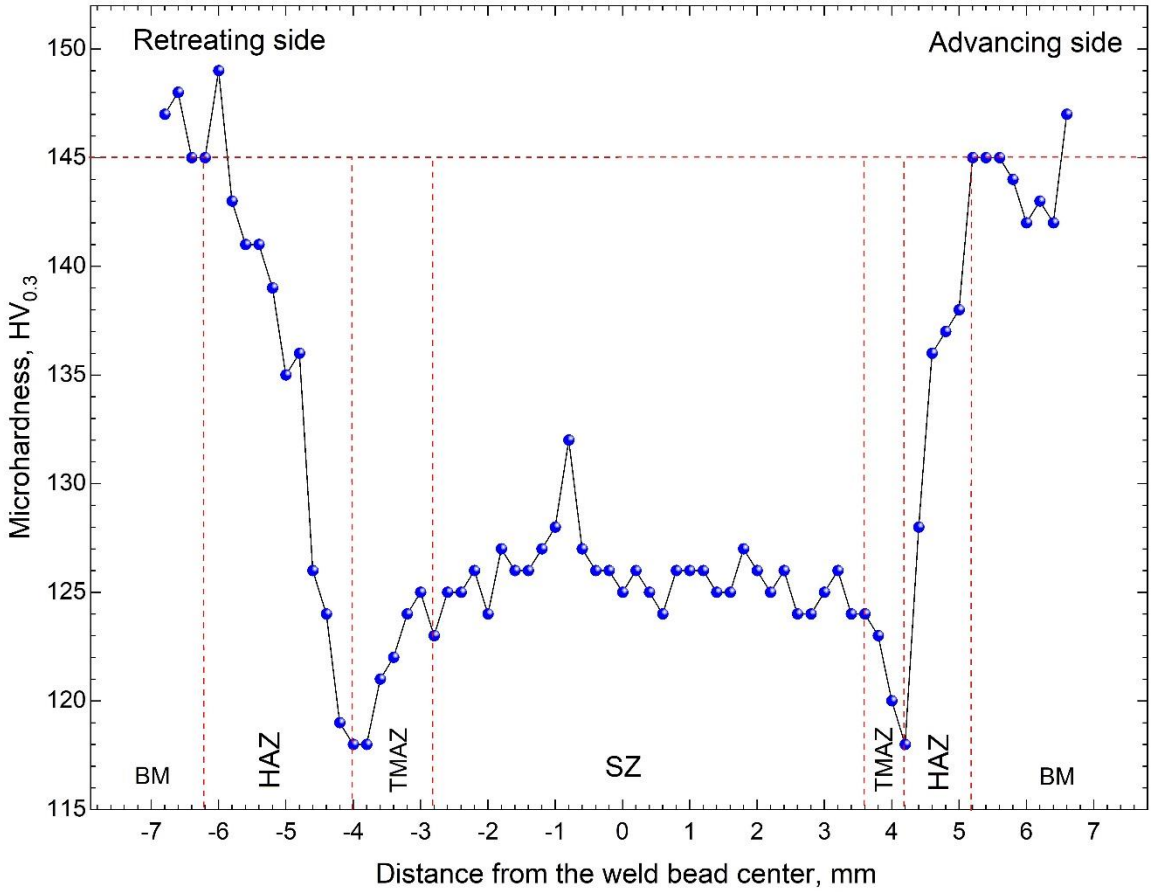

Figure 5.2 - Microhardness profile along the cross section of the AA2524-T3 FSW-welded sample.

Vickers microhardness test throughout all different zones resulting from FSW can assist in understanding the microstructural changes. Figure 5.2 shows that the microhardness of the SZ is lower compared to the BM, due to the high temperatures reached in that zone. Such temperature allows the dissolution of hardening precipitates, the formation of S' phase precipitates and their coalescence, as well as, the dissolution of part of them, which tends to reduce the microhardness values. Even after cooling, the GPB hardening zones, which are formed from the S' phase dissolved by the effect of high temperature, are not sufficient to allow significant increase in microhardness [146]–[149].

Concerning the TMAZ/HAZ-RS and TMAZ/HAZ-AS zones, their microhardness values were very similar (≈118 $Hv_{0.3}$). In addition, it was possible to observe that the area corresponding to the first region is larger than that of the second one. This was expected as the FSW welding process tends to result in a larger TMAZ/HAZ zone on the retreating side due to the rotational and translation movement of the welding tool. This also leads to higher accumulation of particles in the RS comparatively to the AS [146].

The microhardness test reflects a mean value of the indented area [103]. A possible explanation for the microhardness differences between the SZ and both TMAZ/HAZ (RS and AS) is that the SZ in mainly constituted of very small grains well-dispersed (Figure 5.1 - (2)) increasing the materials hardness. Both TMAZ/HAZ zones, especially at the retreating side, is composed of larger grains (Figure 5.1 - (1)), and have coarsened particles and less S' phase hardening precipitates in comparison to the SZ.

5.1.2. Corrosion tests

5.1.2.1. Agar-agar test

Figure 5.3 shows the results obtained from the agar-agar visualization experiment. In this test, the low pH regions due to hydrolysis stimulated by Al^{3+} are associated with the anodic activities [141]. On the other hand, zones of high pH are associated with the reduction of dissolved oxygen that produces hydroxyl ions in the cathodic zones. However, it should be noted that in the gel, due to the slow diffusion of released ions and oxygen, the corrosion kinetics may be different from those observed in aqueous media. Nevertheless, the agar-agar gel visualization technique proposed by Isaacs et al. [141] allows a general visual observation of the region most susceptible to corrosion of the sample under analysis as a function of time.

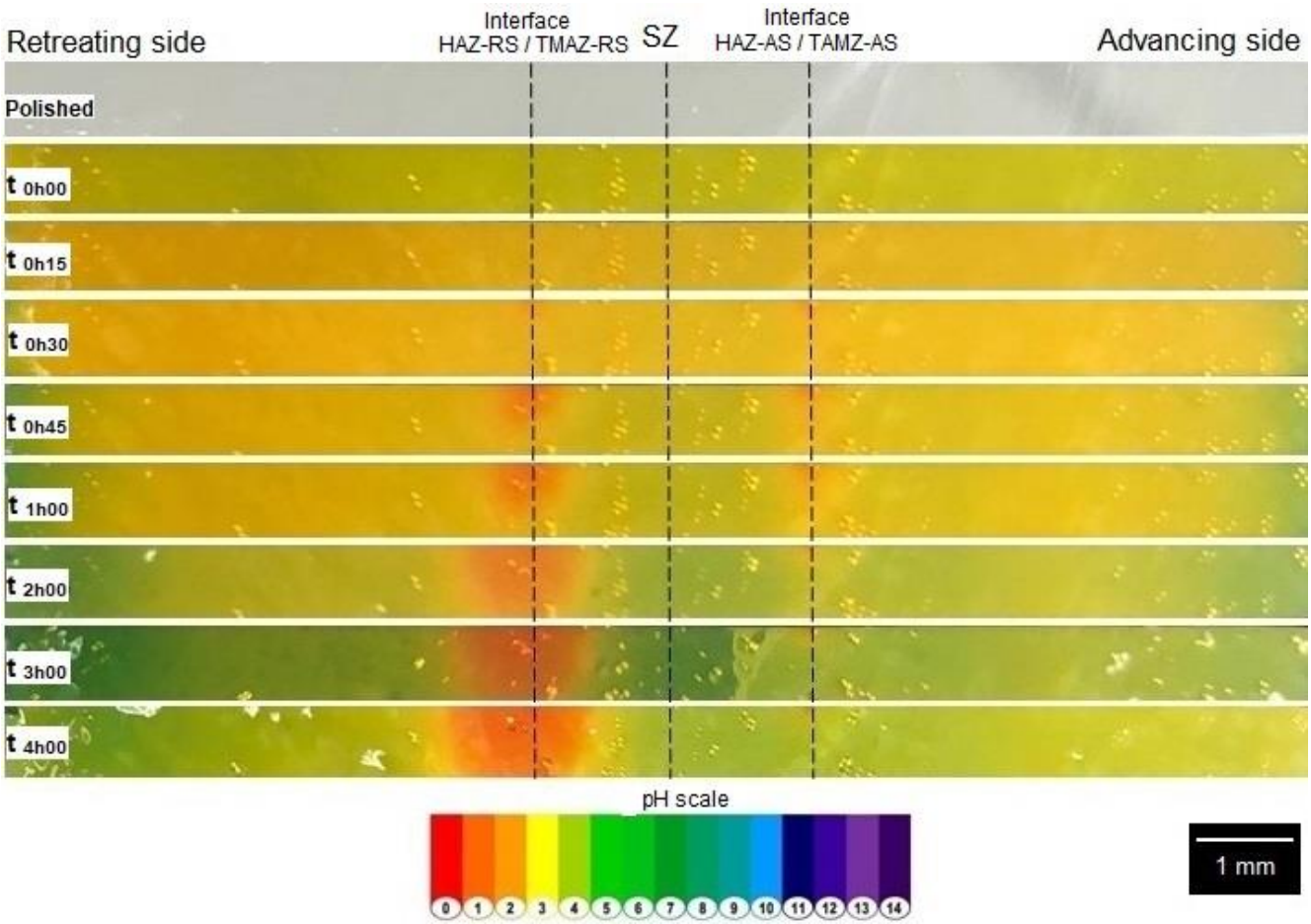

Figure 5.3 - Macrographs showing the color variation directly linked to the pH change along the surface (top view) of a FSW-welded AA2524-T3 sample during the agar-agar visualization test.

It can be observed from the macrographs in Figure 5.3 that the transition area between TMAZ-RS and HAZ-RS, possibly TMAZ-RS, as reported by Queiroz et al. [150], is predominantly anodic in relation to the other exposed zones along the surface of the 2524-T3 aluminum alloy welded by the FSW process. Throughout the experiment, the TMAZ-AS and the HAZ-AS zones also exhibited anodic activities after 30 min, but not very pronounced, and the effects of the anodic reactions on the pH of the medium were not clearly identified for periods longer than 1 h.

Queiroz et al. [150] performed a similar test for the FSW-welded AA2024-T3 alloy and found that the TMAZ-RS was the area of highest anodic activity throughout the entire area under analysis (similar to what is observed in Figure 5.3). It was shown that the corrosion type observed was severe localized corrosion (SLC), which was initiated in regions with copper-rich coarse intermetallic clusters, and these, in turn, were found in greater quantities in the TMAZ-RS than in any other zone of the welded alloy. The observations were related to the higher

amount of fragmented particles at the TMAZ-RS due to the rotational and translational movements of the tool dragging and throwing these particles there when compared to the SZ and TMAZ-AS. Such fragmentation, together with the tool movement causes the accumulation of coarse particles in the TMAZ on the retreating side, which explains the higher electrochemical activity in the zone [150].

In addition, since the FSW welding process is thermomechanical, it changes the quenching condition of the base metal and causes distinct variations along the affected zones of the material. Consequently, activities due to macro and micro galvanic couplings are enhanced in the alloy. It is also worth noting that modifications in welding parameters can alter the corrosion susceptibility of the alloy [115] because such modifications introduce different degrees of deformation.

5.1.2.1.1. Image analysis

It has been reported in literature that the electrochemical most active area in certain materials is related to its high concentration of micro cells. Different morphology and sizes of intermetallic particles affect the corrosion behavior of Al alloys. According to Blanc and Mankowski (1997) [151] and Blanc et al. (1997) [152] the size and amount of particles in the aluminum alloy, besides their composition, are among the most significant features influencing pitting properties.

Figure 5.4 shows the TMAZ/HAZ-RS (a) and the TMAZ/HAZ-AS zones (c) and their particle distribution from the image analysis, (b) and (d), respectively. Although the entire cross section of the AA2524-T3 FSW-welded sample has been analyzed, a special attention was given to these zones because they were the most actives areas, as shown in Figure 5.3.

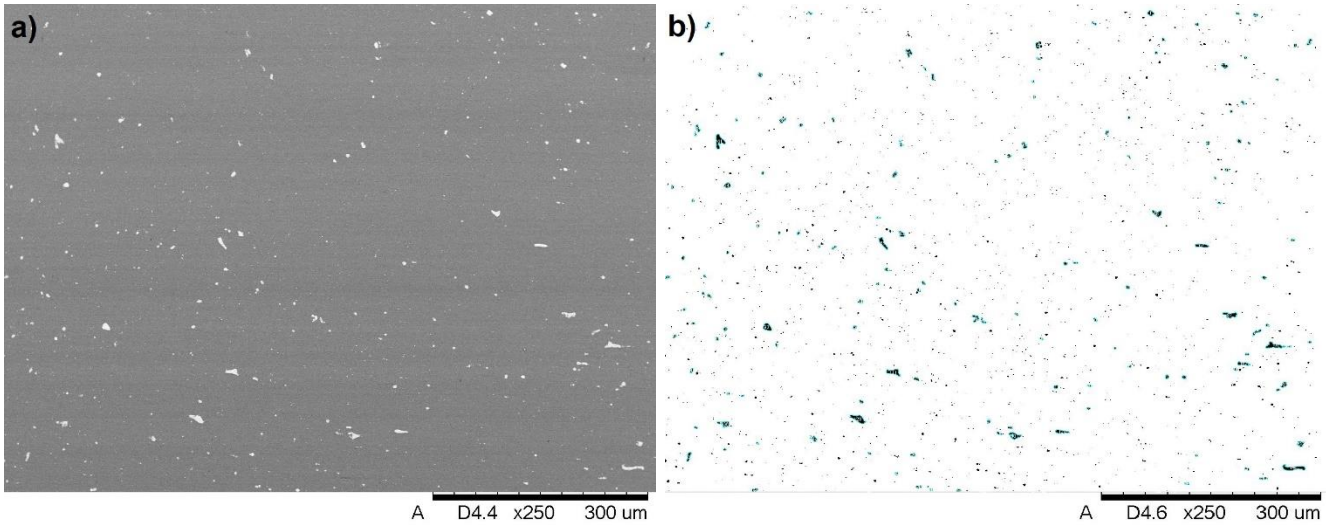

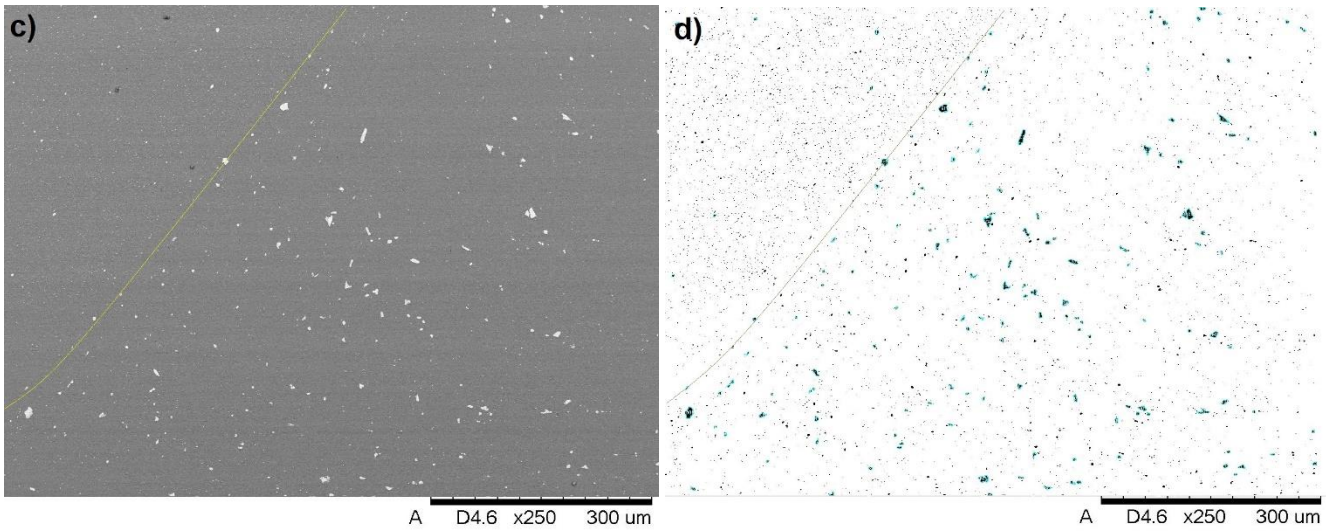

Figure 5.4 - Electron micrographs of the TMAZ/HAZ-RS (a) and the TMAZ/HAZ-AS zones (c) and its image particle distribution analysis, respectively (b) and (d).

In Figure 5.4c, it was added a yellow line over the TMAZ/HAZ-AS interface (hundreds of micrometer thickness) to highlight the difference in size and particle distribution between the SZ and TMAZ-AS. Such SEM analysis is complementary to the optical micrographs shown in Figure 5.1 since it is possible to better observe the particle distribution and their mean size.

Image analysis was performed with the support of the ImageJ® software. It was necessary as the intermetallic particles were well dispersed along the whole microstructure. Even though Figure 5.4 does not show significant differences between the distribution of particles in the TMAZ/HAZ-AS and TMAZ/HAZ-RS, the image analyses performed showed that there are minor variations related to particle distribution and it can be correlated to the phenomenon observed in Figure 5.3.

Table 5.1 shows image analysis results for the entire microstructure. The analysis consisted of calculating the area corresponding to the intermetallic particles with size greater than 10 μm^2. This condition was applied as the interest was to study the distribution of coarse particles.

Table 5.1 - Area covered by particles with sizes greater than 10 μm^2 over the AA2524-T3 welded sample.

	Particles ≥ 10 μm^2			
	BM	TMAZ/HAZ-RS	SZ	TMAZ/HAZ-AS
Area coverage (%)	0.504	0.740	0.464	0.515

Results from image analyses showed that the area occupied by large particles (>10 μm^2) varied along the AA2524-T3 FSW-welded sample. Even though it seems to be minor differences, when it comes to micro cells it can have a huge effect on the initiation and propagation of the corrosion process, as it can be observed in Figure 5.3 and the data of Table 5.1. Indeed, these micro and nanoparticles can be seen as an array of microelectrodes on which the cathodic reaction is enhanced.

The results of this work corroborate those of Queiroz et al. (2019) where the corrosion process was preferentially located in the TMAZ/HAZ-RS region, compared to the TMAZ/HAZ-AS. This was related to the level of particle breakdown due to rotational and translational movement of the welding tool. The tool movement was responsible for accumulation of coarse particles in the TMAZ/HAZ area on the retreating side, which explains the higher electrochemical activity in that zone.

The stir zone (SZ) presents the lowest levels of large intermetallic particles because this zone experiences the most intense movement of the tool leading to a severe breakdown of the particles present.

5.1.2.2. Exfoliation corrosion test (ASTM G34)

Exfoliation corrosion is known to be a more aggressive form of intergranular corrosion, being the result of the continuous expansion of corrosion products generated between grain boundaries by intergranular corrosion. Figure 5.5 shows macrographs of a FSW-welded AA2524-T3 alloy specimen (a) and the base metal separately (b) after 15 minutes of immersion in EXCO solution (4.2.1.3.1) during the exfoliation corrosion test. As the etching solution is very aggressive, hydrogen bubbles appear on the entire surface of the specimen already within the first few minutes of testing.

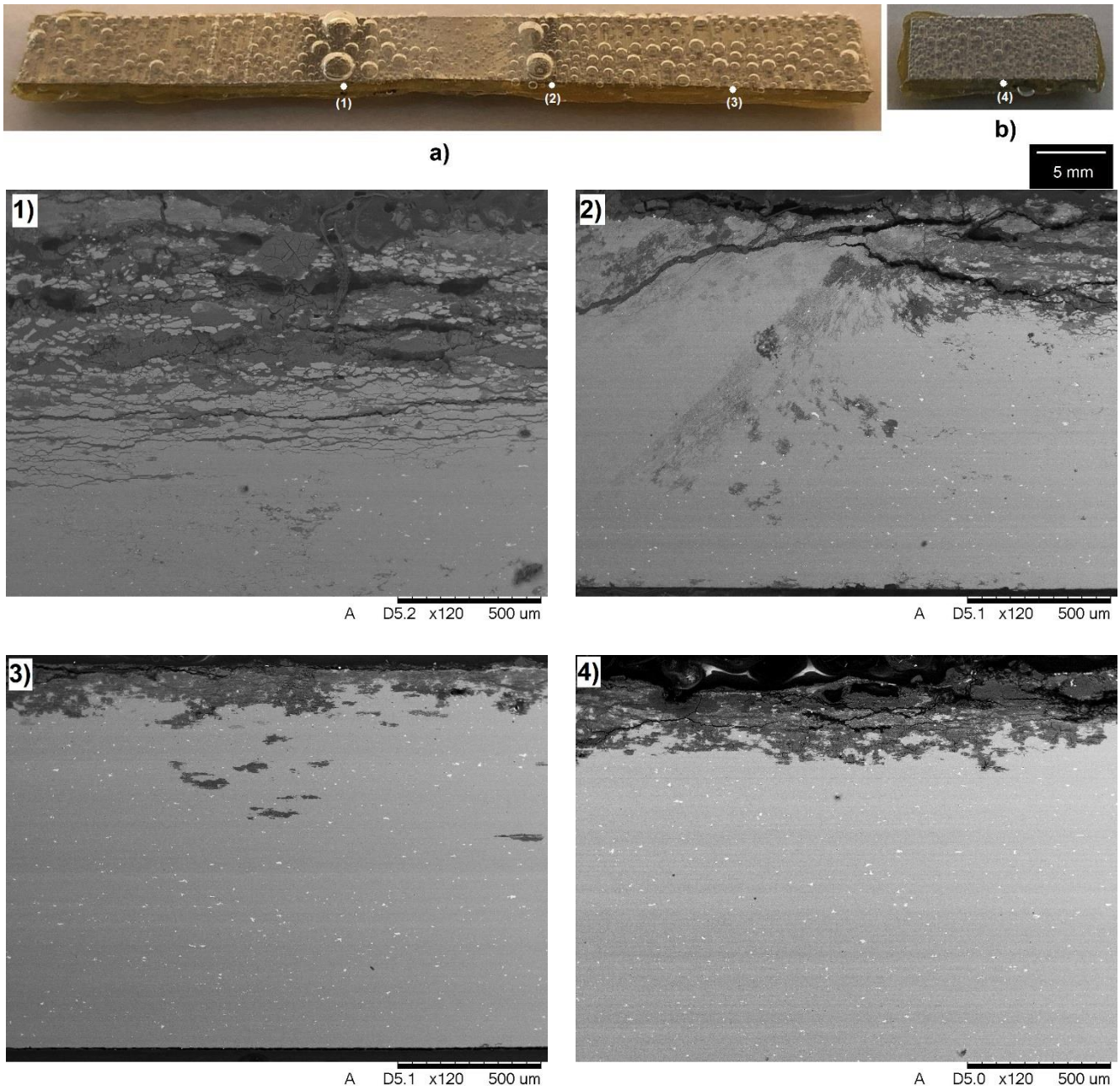

Figure 5.5 - Macrographs of the welded AA2524-T3 sample (a) and its base metal separately (b) after 15 minutes of immersion in EXCO solution. Additionally, it is shown cross section micrographs obtained by SEM of the welded sample: (1) TMAZ/HAZ-RS, (2) TMAZ/HAZ-AS, (3) BM, and separately, (4) BM after the exfoliation corrosion test.

Corrosion activity was significantly reduced in the recrystallized stir zone (SZ) of the material (indicated in this case by the smaller volume of bubbles) comparatively to the other zones exposed to the solution. It occurs because recrystallization process consumes part of the energy stored between grains generated during the rolling process leading to grain elongation and deformation, as is the case of aluminum alloys [140]. This is one of the possible

explanations for the phenomenon observed in Figure 5.5a, because the grains in the BM are still deformed by the rolling process, while in the SZ, recrystallization with grain refinement occurred. This was due to heat generation in that region, arising from the rotation movement and displacement of the welding tool (see Figure 3.4), consequently, decreasing the energy stored in such grains.

It is seen in Figure 5.5a the presence of larger volume of bubbles at the TMAZ and HAZ of AS and RS, especially at the retreating side comparatively to the other zones. Figure 5.5 (1) confirms that exfoliation was more intense in the TMAZ/HAZ-RS in comparison to the TMAZ/HAZ-AS (Figure 5.5 (2)). This result shows that FSW besides resulting in higher quantities of intermetallic particles in the retreating side, than in the advancing one, it also leads to changes in the precipitation of hardening precipitates, as shown in Figure 5.2. Consequently, susceptibility to exfoliation corrosion was dependent on the side of the FSW affected zone.

Regarding the base metal, the cross section analysis of the FSW-welded sample (Figure 5.5 (3)) and the unwelded one (Figure 5.5 (4)), it can be seen that exfoliation was more intense in the sample tested separately. It suggests that in the welded sample the BM was cathodically protected while the other zones acted anodically, especially the region of TMAZ/HAZ-RS.

5.1.2.3. Intergranular corrosion test (ASTM G110)

Figure 5.6 shows different macrographs of the AA2524-T3 FSW-welded sample (a) and its base metal separately (b) after 30 minutes of immersion in the intergranular corrosion test solution. Then, in the same figure, electron micrographs of the welded sample are shown: (1) BM-RS, (2) SZ and, separately, (3) BM after intergranular corrosion test (6 hours).

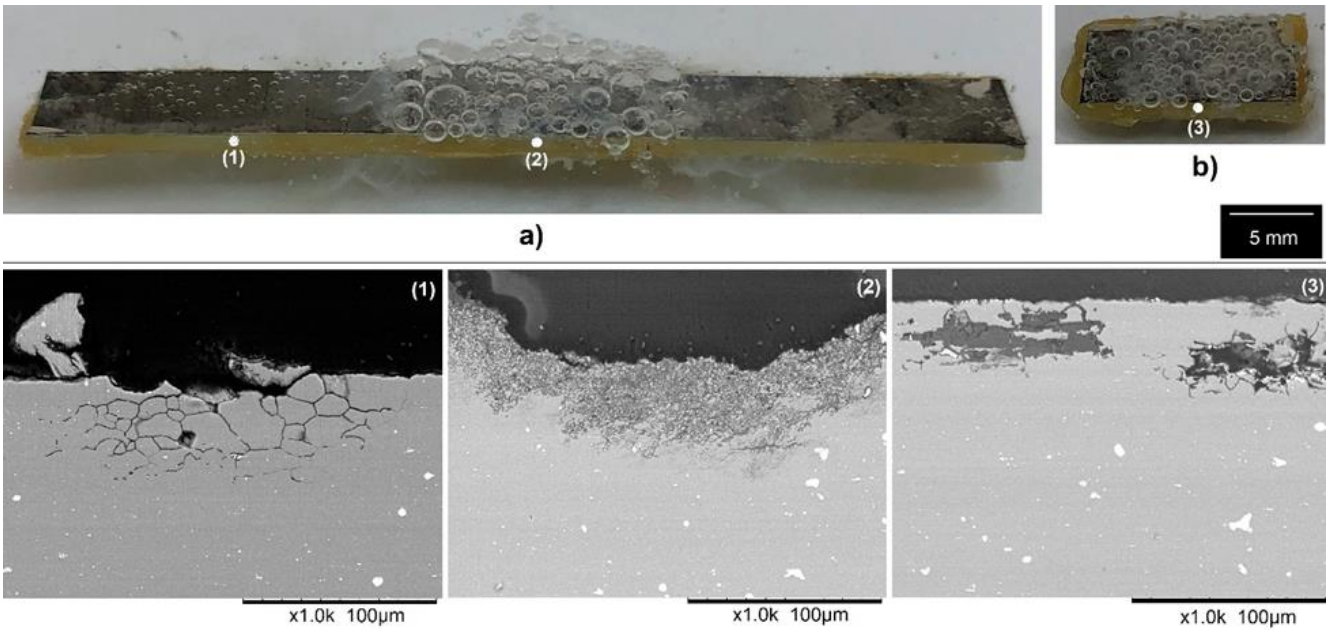

Figure 5.6 - Macrographs of the welded AA2524-T3 sample (a) and its base metal separately (b) after 30 minutes of immersion in the intergranular corrosion test solution. Cross section micrographs obtained by SEM of the welded sample: (1) BM-RS, (2) SZ, and, (3) BM tested separately, after intergranular corrosion test.

In Figure 5.6a it is evident the evolution of bubbles in the central zone of the sample (weld region), while on the rest of the sample (BM) few and small bubbles were seen. A dark surface film was observed, possibly due to copper redeposition, or copper enrichment by selective leaching of aluminum and magnesium from the alloy, and of other compounds [89], [153]. Further analysis is required by the use of other characterization techniques to confirm this hypothesis.

It is known that the FSW process gives rise to different welding zones, each with its own intrinsic characteristic (item 5.1.1.1). As each region has unique electrochemical potential, it is possible that the phenomenon of galvanic coupling occurs, which is corroborated by the cathodic protection observed in the BM coupled to the welded zone, with the BM being nobler than the weld joint.

Relatively to the weld zone, it is important to highlight that due to rotation and translation movements of the weld tool, this region experiences different temperature gradients, phase dissolution, precipitate enrichment, reprecipitation and mainly microstructural modifications, as can be observed in Figure 5.6 - (1) and (2).

Another phenomenon is the fact that the BM of the welded specimen (Figure 5.6a) presented few and small bubbles from the corrosive process while the same BM, but isolated from the rest of the specimen and exposed to the corrosive environment (Figure 5.6b),

presented a considerable amount of bubbles, indicating a higher susceptibility to intergranular corrosion.

The higher susceptibility to corrosion can be better observed by means of Figure 5.6 - (1) and (3). It is possible to notice that intergranular corrosion shown in Figure 5.6 - (3) is more intense than the one related to the welded sample with all zones exposed. In addition to intergranular corrosion, as seen in Figure 5.6 - (1), there is also the occurrence of intragranular corrosion, indicating a more intense corrosion process with removal of material and formation of corrosion products.

5.1.3. Electrochemical characterization of the FSW-welded AA2524-T3

Electrochemical evaluation of the 2524-T3 aluminum alloy welded by FSW was performed using a microcell (0.049 cm^2 exposed area) and isolating each analyzed zone with wax, in a 100 mM Na_2SO_4 + 1 mM NaCl solution. This solution presents lower aggressiveness compared to the ones with results presented in the previous sections. Sulfate ions adsorb on aluminum alloys surface, contributing to their passivation and delaying nucleation of pits and, therefore, the breakdown of the passive film [152], [154], [155].

Figure 5.7 shows the variation of open circuit potential with time of immersion in the test solution for the AA2524-T3 welded by FSW.

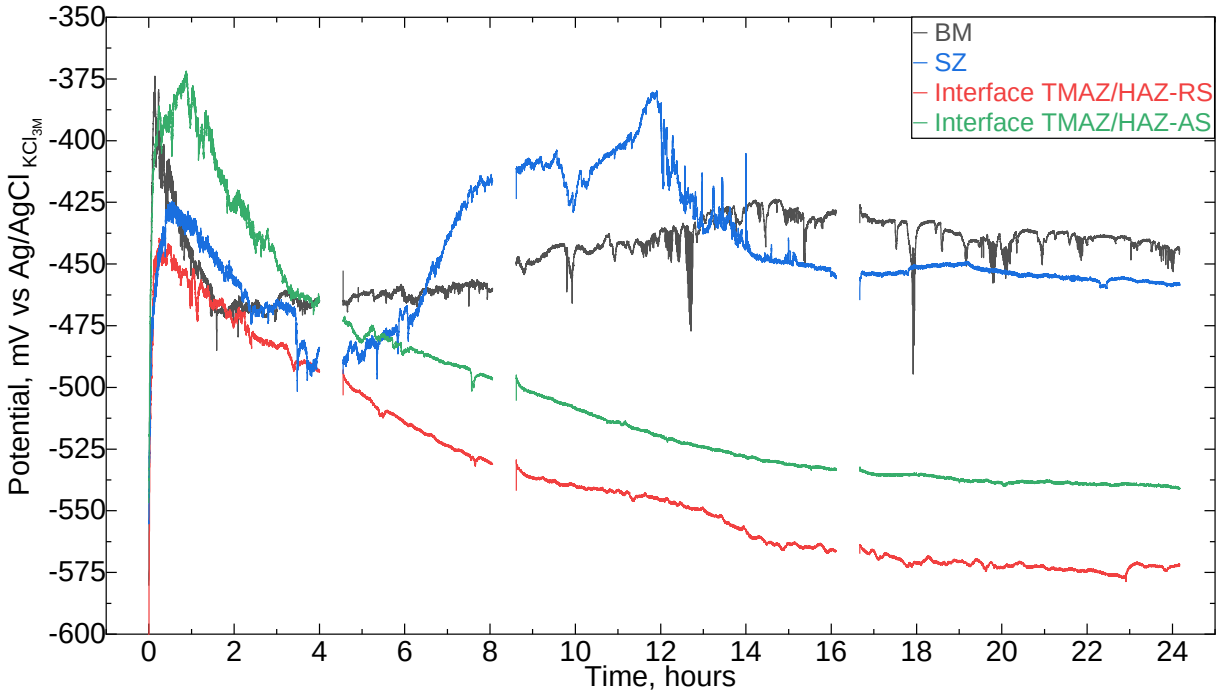

Figure 5.7- Open circuit potential variation with time of immersion in 100 mM Na_2SO_4 + 1 mM NaCl solution of different zones of the AA2524-T3 welded by FSW.

Figure 5.7 shows that all zones presented increase in potential soon after exposure to the test solution, possibly related to preferential dissolution of Mg, that is the most active element in the alloy , as well as the growth of the oxide on the Al alloy matrix by immersion in aerated medium [156]. Then, it was followed by potential drop that can be explained by localized attack to the weak areas of the oxide film with time of immersion in corrosive medium. The presence of Cl^- ions in the solutions favors corrosion attack at the weakest areas of the oxide film, that in the alloy studied, corresponds to the regions of the micrometric particles.

It can be seen that both TMAZ/HAZ zones (RS and AS) shows a similar behavior. Once the potential starts decreasing, due to oxide film breakdown, after near one hour of the experiment, it continuously decreased until the end of the experiment. In addition, these two zones presented the lowest potential among all the studied zones, with the retreating side showing the most negative value (approximately -575 mV).

Another interesting information that can be drawn from Figure 5.7 is the possibility of galvanic coupling (potential difference higher than 50 mV between two adjacent zones) between the SZ and each of the zones. It must be mentioned that the stir zone is in direct contact with the TMAZ of both sides (Figure 5.1). The potential difference between the SZ and the advancing side is around 85 mV, and the difference on the retreating side is nearly 115 mV, which is consistent with the results shown in the agar-agar test (Figure 5.3), and image analysis (Figure 5.4) where the tendency to corrosion of these zones was observed.

The potentials related to the BM and SZ in the curves of Figure 5.7 suggest that oxide growth and localized attack occurred continuously during exposure to the test solution. However, potential oscillations decreased in amplitude after 14 h for the SZ, whereas it continued for the BM along the duration of test. These results suggest that the base metal is highly susceptible to pitting nucleation although corrosion propagation was favored on both TMAZ/HAZ sides of the welded alloy.

Modifications introduced by friction stir welding of the 2524-T3 aluminum alloy were observed. Such microstructural modifications rise from rotation and translation movements of the weld tool and can lead to galvanic coupling, pit nucleation at some zones, and solubilization, dissolution of hardening precipitates, and intermetallic particles breakdown.

Figure 5.8 shows electrochemical impedance (EIS) diagrams (Nyquist) obtained after 4 h, 8 h, 16 h and 24 h, for the following zones: BM (a), TMAZ/HAZ-RS (b), SZ (c), and TMAZ/HAZ-AS (d).

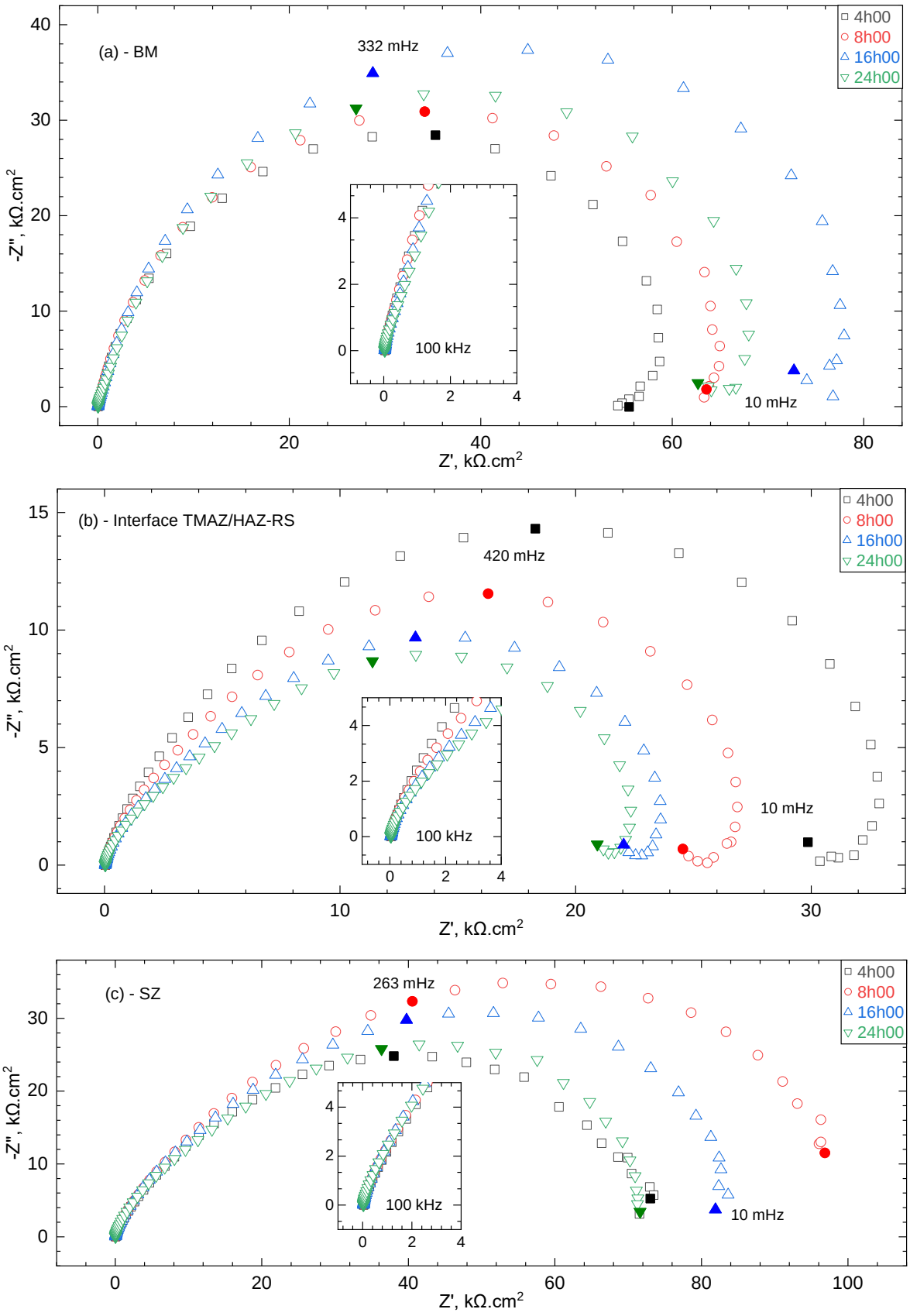
(a) - BM
332 mHz
10 mHz
100 kHz
4h00
8h00
16h00
24h00
-Z'', kΩ.cm²
Z', kΩ.cm²
(b) - Interface TMAZ/HAZ-RS
420 mHz
10 mHz
100 kHz
4h00
8h00
16h00
24h00
-Z'', kΩ.cm²
Z', kΩ.cm²
(c) - SZ
263 mHz
10 mHz
100 kHz
4h00
8h00
16h00
24h00
-Z'', kΩ.cm²
Z', kΩ.cm²

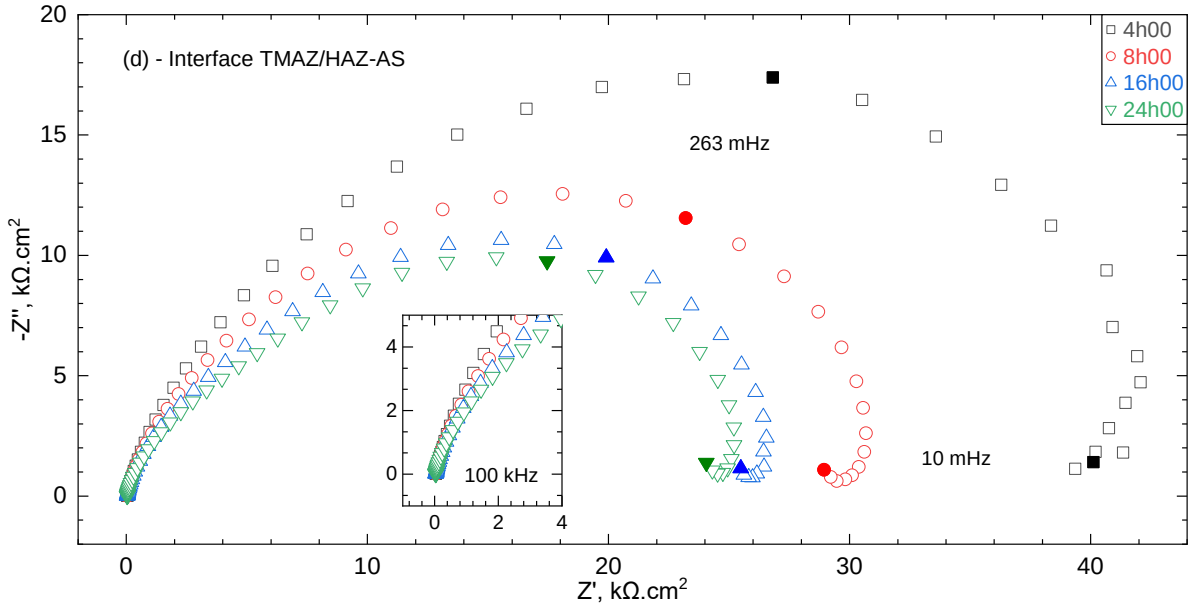

Figure 5.8 - Electrochemical impedance diagrams after 4 h, 8 h, 16 h and 24 h, of immersion in 100 mM Na_2SO_4 + 1 mM NaCl solution for the following zones: BM (a), TMAZ/HAZ-RS (b), SZ (c), and TMAZ/HAZ-AS (d).

EIS results presented in Figure 5.8 was used here qualitatively for comparison of the corrosion resistance of different zones resulting from FSW. Regarding the results reproducibility, which is not trivial, no changes were observed in the trend between triplicate measurements. Firstly, it is important to note that the highest impedances were related to the SZ, whereas the lowest ones, to the TMAZ/HAZ-RS. It is worth mentioning, that for the BM, the impedance continuously increased with time of exposure to the test solution, corroborating the hypothesis of oxide growth on the matrix of the BM along the test, as suggested by Figure 5.7. It is also interesting to notice that for the TMAZ/HAZ-RS and TMAZ/HAZ-AS, the impedance continuously decreased with time, also corroborating the results shown in Figure 5.7. In addition, for the SZ, impedance and potential increased between 4 h and 8 h, and then decreased slightly until the test was terminated. However, during the whole test period the impedances for the SZ were always superior to those of the BM.

For the welded zone (Figure 5.8 (b), (c) and (d)), a depressed capacitive arc can be seen in the high-medium frequency range. Though the visual evaluation of the impedance data above the real axis in the high-medium frequency yield only one time constant, a more detailed analysis of the data can lead to the derivation of at least two time constants (not performed in this work) [157], [158]. The number of time constants is determined by calculating the difference between the fitted and the experimental data as function of frequency. When this difference

shows a periodicity, it means that not all time constants have been taken into account. Therefore, it is believed that the visual depressed capacitive loop above the real axis is due to the interaction of two capacitive loops, as suggested in the literature [158], [159].

In Figure 5.8 (b) and (d) it can be observed a depressed capacitive arc in the high to intermediate frequencies whose radius decreased with time. This could be due to the interaction of different time constants also indicating a process under activation control. The literature relates the decreasing in the radius with the decrease in the charge-transfer resistance and the increasing of the double layer capacitance with the development of pitting at the surface [159].

In addition, the inductive loops at the low frequency domain, according to the literature, can be attributed to the relaxation of adsorbed anions on the electrode surface, in which oxygen ions predominate because it is responsible for the oxide layer growth [160], [161]. On the other hand, the literature also attributes the inductive loop with the weakening of the protective effectiveness of the aluminum oxide layer with increasing immersion time, because the surface oxide layer becomes progressively less protective, due to the action of the Cl^- anions [159].

Following the discussion about the evaluation of the corrosion rate from the EIS diagram (in the previous part), we consider in this work that it is given by charge transfer resistance, that is, in the case of the diagram presented in Figure 5.8 by the amplitude of the high frequency loop. It is also worth noting that in this case, the error made by using the polarization resistance is directly linked to the amplitude of the low frequency inductive time-constant.

The obtained EIS diagrams that showed the lowest impedances related to TMAZ/HAZ interfaces are in good agreement with the results previously discussed: agar-agar test (Figure 5.3), microstructural characterization (Figure 5.1), image analysis (Figure 5.4), and OCP measurements (Figure 5.7). In those experiments, it was possible to observe that the TMAZ/HAZ-RS was the zone most susceptible to corrosion initiation and propagation. This was related to the highest concentration of (Al_2CuMg) phase S intermetallic particles that were broken and dragged to the zone due to the rotation of the tool during FSW. The results are also in accordance to the pertinent literature [87], [88], [163], [157]. The last point to mention is the fact that all the EIS diagrams are similar in shape and the time-constants of each spectrum remains also unchanged. This indicated that even if the kinetics of the corrosion mechanism changes as a function of the investigated zone, the electrochemical mechanism involved remains the same.

5.2. Magnesium

5.2.1. Steady-state measurements

Leleu et al. (2018) [20] showed that the corrosion rate of a commercially pure Mg was about four times higher in NaCl solution than in Na_2SO_4 solution. Thus, in the present study, a less aggressive electrolyte than NaCl was chosen to reduce the dissolution rate of Mg in order to perform EIS measurements over extended periods.

The variations of the corrosion potential and pH measured in a 0.1 $mol.L^{-1}$ Na_2SO_4 solution, either with or without Mg immersed in the solution is shown in Figure 5.9. The pH and E_{corr} measurements in both conditions were carried out simultaneously to take into account any environmental influence during the experiment, e.g., temperature and air composition variations.

A significant variation of E_{corr} (blue line) is observed during the first 20 hours of immersion. E_{corr} increased quite rapidly and then stabilized after 32 hours. This E_{corr} evolution is accompanied by the alkalinization of the electrolyte: the initial pH was 5.7 (red line) and rapidly increased to reach a pH value of 8.3 after 60 hours of immersion. A tendency to continuous increase was seen, as previously reported by Bo et al. (2014) [164]. The corrosion potential increase can be correlated to the growth of the magnesium oxide film (MgO) and its protective effect with immersion time. The blank experiment, i.e., the pH variation measured without any Mg in solution shows a small decrease of 0.2 unit in pH value during the 60 hours of the experiments. As expected, the pH increase is to be ascribed to the reactivity of Mg that produce hydroxyl ions when it corrodes.

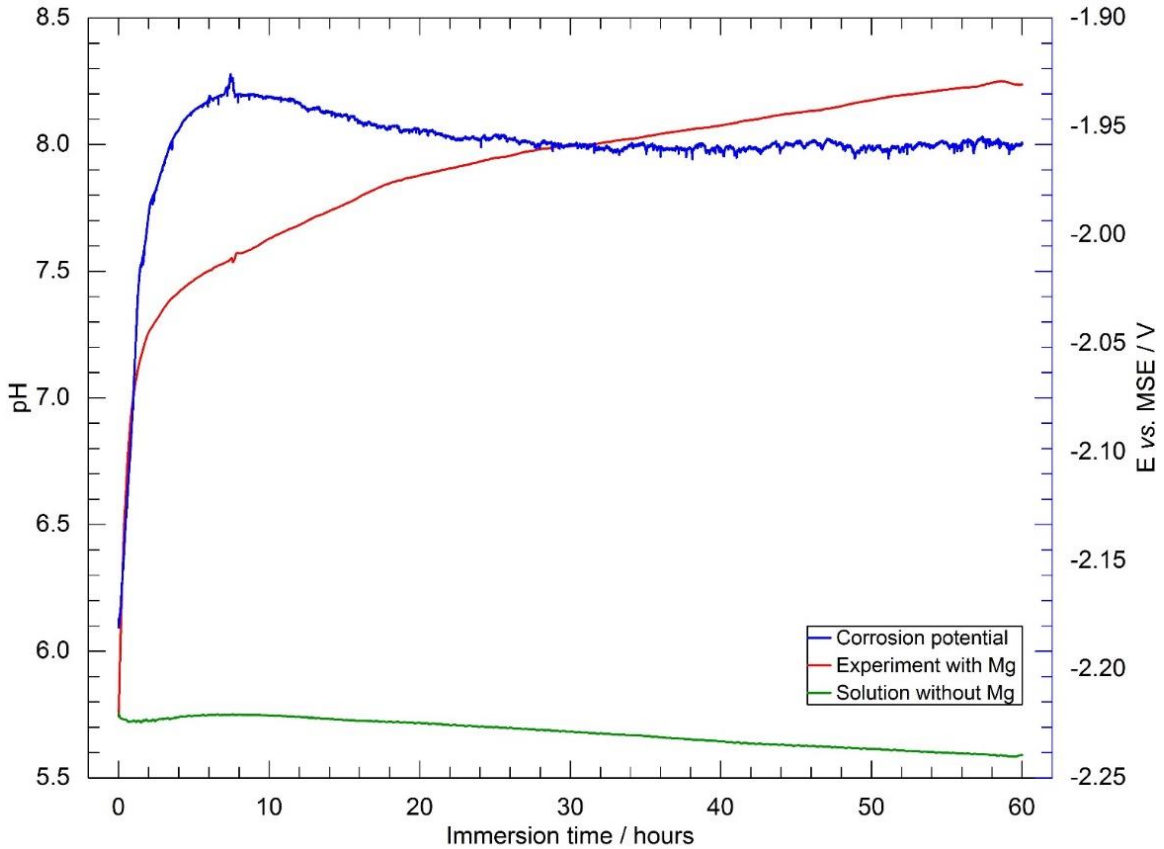

Figure 5.9 - Corrosion potential (-) and pH variation in 0.1 mol.L^{-1} Na_2SO_4 solution (Ω = 1000 rpm), with (-) and without (-) Mg in solution, as a function of immersion time.

Current-potential curves obtained for pure Mg after 2 h and 24 h immersion times in 0.1 mol.L^{-1} Na_2SO_4 solution at E_{corr} are shown in Figure 5.10. It shows the evolution of the current as the potential changes progressively on the pure Mg electrode. A low scan rate corresponding to 0.167 mV.s^{-1} was used in an attempt to be as close as possible to the steady-state polarization curve.

As previously reported, whatever the immersion time, the anodic polarization curves can be split up in three different domains [53]. The first domain for low anodic overvoltage is almost linear (150 mV from the corrosion potential), it is composed of a mixed controlled domain, composed of diffusion and kinetics contribution. This behavior might be explained by the formation of a monovalent adsorbed intermediate followed by the formation of the divalent Mg^{2+} ion. It can also be seen that the current density decreases when increasing the immersion time. The second domain starts at about -1.9 V/MSE for which a significant change in the slope of the curve and an increase of the current density can be observed. Such behavior could be ascribed to a change of the limiting process in the dissolution mechanism, e.g., ohmic drop control due the increase of the MgO film thickness as a function of time. The last domain, for

potentials higher than -1.8 V/MSE, is characterized by a plateau of current density at about 20 mA.cm^{-2}, independent of the immersion time.

The cathodic polarization curves correspond to the hydrogen evolution reaction and show two different slopes that are difficult to interpret due to the formation of hydrogen bubbles at the electrode surface. Nevertheless, it is shown that the cathodic curves are not strongly influenced by immersion time, and the slopes are very close to each other at potentials below -2.16 V/MSE. On noble metals, these two slopes are usually explained using the two possible mechanisms for the hydrogen evolution reaction, namely the Volmer-Tafel and the Volmer Heyrovsky mechanisms.

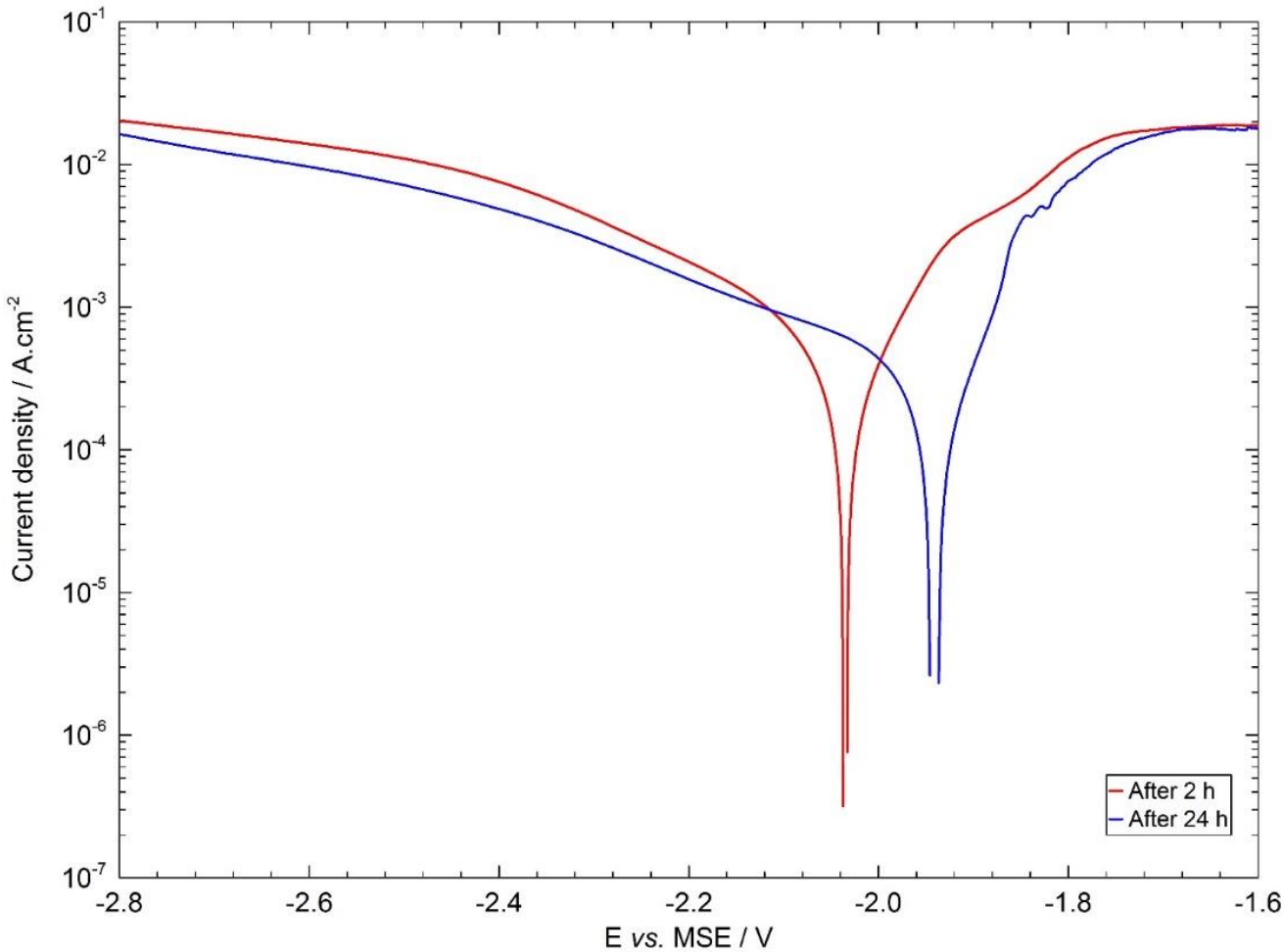

Figure 5.10 - Current-potential curves obtained after 2 h (-) and 24 h (-) of pure Mg immersion in 0.1 mol.L^{-1} Na_2SO_4 solution at E_{corr} (Ω = 1000 rpm and v = 0.167 mV.s^{-1}). The anodic and cathodic branches were obtained separately from E_{corr} (independent measurements), and the curves were corrected for the ohmic drop.

5.2.2. Electrochemical impedance measurements

5.2.2.1. Electrochemical impedance diagrams at E_{corr}

The influence of different rotation rates on the impedance diagram for a pure Mg electrode is shown in Figure 5.11a. Such EIS diagrams were obtained in a potentiostatic mode at E_{corr} after 12 h of immersion in 0.1 mol.L^{-1} Na_2SO_4 solution. These impedance diagrams were measured on the same electrode one after the other. Thus, the slight difference in amplitude for these EIS diagrams may be explained by an evolution of the reactivity or the variation in the active surface area of the Mg. All these diagrams show three distinct time constants. In the high-frequency range, the first capacitive loop corresponds to the charge transfer resistance in parallel with the interfacial capacitance. This capacitance will be thoroughly discussed in the following sections. The medium-frequency time constant is attributed to the diffusion of Mg^{2+} species inside the porous layer ($Mg(OH)_2$) formed by the corrosion products. It has been previously shown that this time constant was independent of the electrode rotation rate [51]. The low-frequency inductive loop is ascribed to the relaxation of adsorbed intermediates. Such mechanism, involving a monovalent species adsorbed on the electrode surface has already been observed for the corrosion of different metals, including Fe [165], [166], Cr [167] and Zn [168], [169] that is for multi-step reaction mechanism involving adsorbed species [165], [170], [171].

Figure 5.11b shows the diagrams presented in Figure 5.11a after normalization. The normalization procedure was performed by dividing each EIS diagram present in Figure 5.11a by the largest value of its real part intercepting the x-axis. The normalization of such curves allows one to observe that the EIS diagrams evolution with time is related to a change of the sample active surface area, as it is possible to observe a homothetic variation.

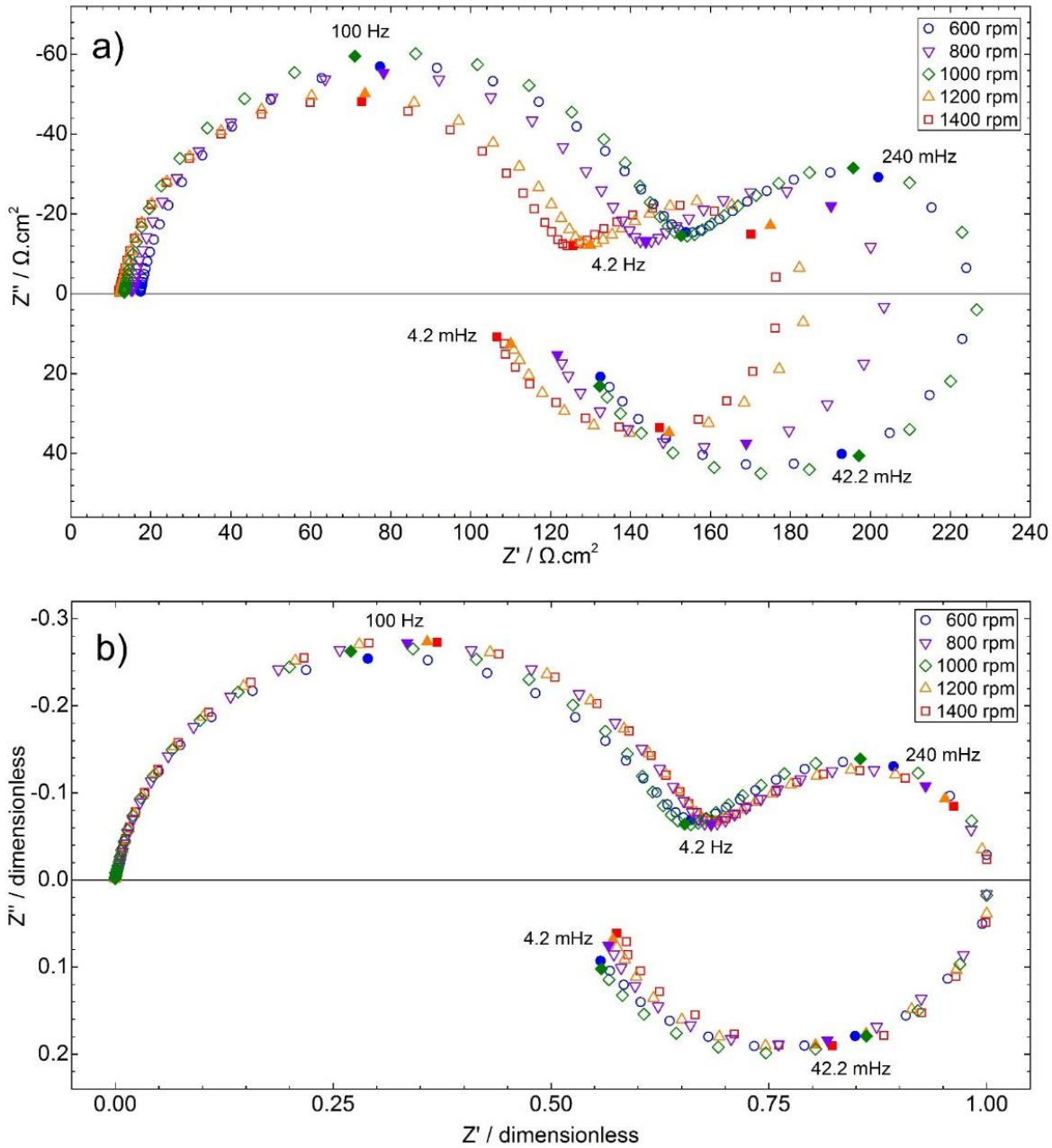

Figure 5.11 - Electrochemical impedance diagrams of pure Mg after 12 hours of immersion in 0.1 mol.L^{-1} Na_2SO_4 solution at E_{corr} for different rotation rates: a) raw impedance diagrams (Nyquist representation) and b) normalized impedance diagrams (each diagram was normalized by the maximum value of the real part of the impedance).

Even though the diagrams shown in Figure 5.11a look like presenting different proportions, it is possible to observe in Figure 5.11b, in a dimensionless representation, that they all have the same aspect ratio over the whole frequency range, leading to conclude that the difference observed in Figure 5.11a is due to the evolution of the system itself.

According to Figure 5.11b, all the EIS diagrams are quasi-identical, especially the medium frequency time constant which is ascribed to diffusion. Since the diffusion contribution on the EIS in liquid phase is governed by the rotation rate of the electrode, this means that the

diffusion process occurs in the solid phase, i.e., inside the thick porous layer ($Mg(OH)_2$) and does not depend on the hydrodynamic layer, as already demonstrated by Baril; Pébère (2001) [51].

Impedance diagrams (Nyquist coordinates) obtained at E_{corr} for the pure Mg electrode as a function of immersion time are shown in Figure 5.12a. They were obtained after different immersion times in 0.1 mol.L^{-1} Na_2SO_4 solution and $\Omega = 1000$ rpm.

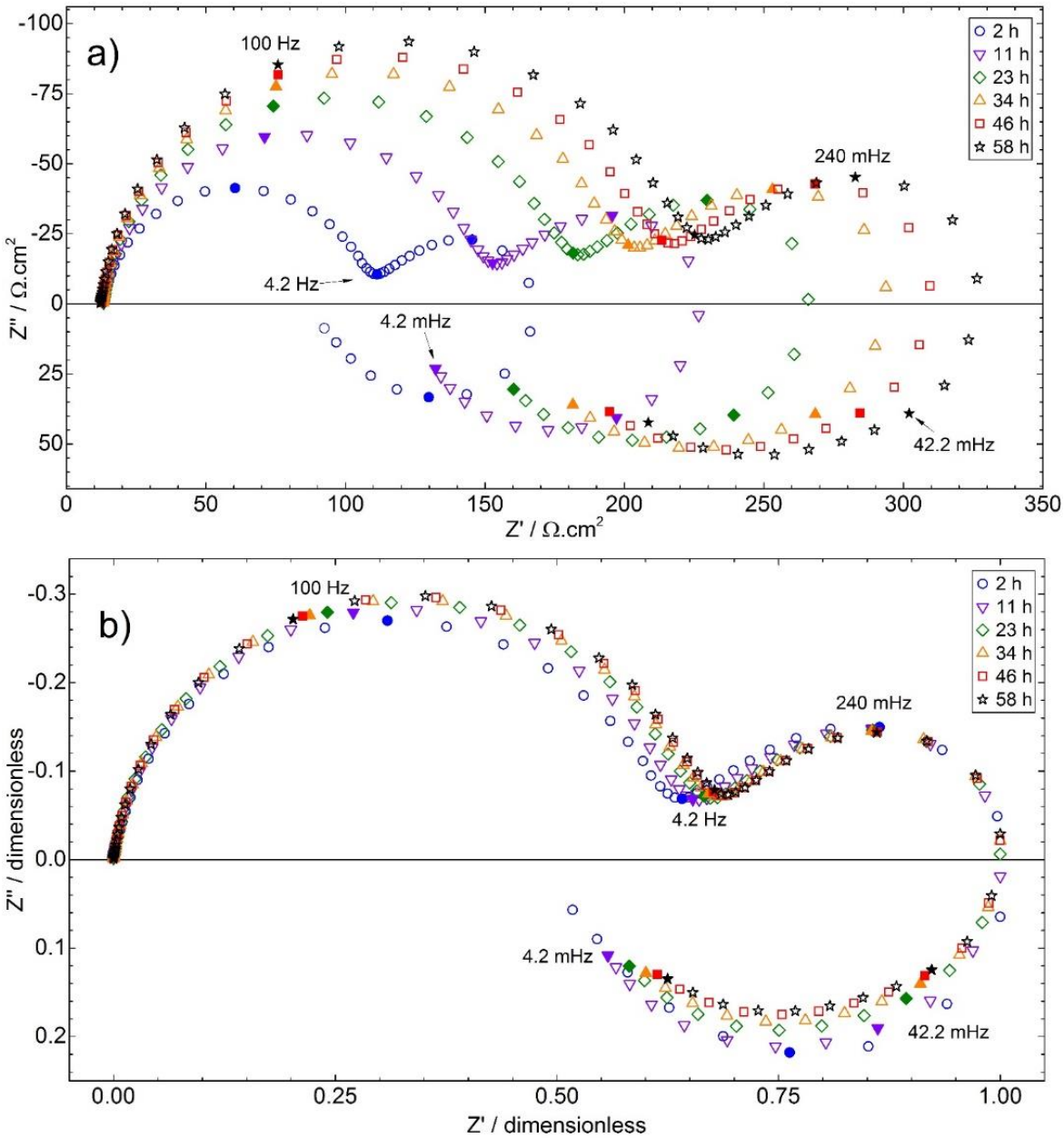

Figure 5.12 - Electrochemical impedance diagrams obtained for pure Mg after different immersion times in 0.1 mol.L^{-1} Na_2SO_4 solution at E_{corr} (Ω = 1000 rpm): a) raw impedance diagrams (Nyquist representation) and b) normalized impedance diagrams (each diagram was normalized by the maximum value of the real part of the impedance).

Interestingly, the impedance diagrams in Figure 5.12a are homothetic to each other. This can be better visualized in Figure 5.12b, where each diagram was normalized by the maximum value of the real part of the impedance. With such a dimensionless representation, all the EIS diagrams superimpose and the three-time constants remain unchanged regardless of the immersion time, except for the first time of measurement (2 h). This difference can be ascribed to the reactivity of the bare Mg during the first hours of immersion.

Moreover, the characteristic frequency of the first capacitive loop slightly varies with time. Conversely, the second characteristic frequency, corresponding to the diffusion process is constant, in agreement with the rotating disk electrode (RDE) theory for the diffusion in a finite-thickness layer. As a result, whatever the frequency domain considered, the variation of the amplitude of the impedance response of each process follows the same proportionality law. This behavior can be attributed to a variation of the active surface area with the immersion time. In other words, the increase of the impedance translates into a decrease in current, i.e., a decrease of the active surface area of the electrode on which the Mg dissolution occurs. It should be noticed that this active surface area is small by comparison with the surface area covered by MgO (see section 5.3.2). This conclusion is in agreement with scanning electrochemical microscopy experiments performed above a corroding Mg substrate that showed a decrease of the surface area of the reactive domain as a function of the immersion time [53].

5.2.2.2. Kinetics model of the corrosion mechanism

A general sketch of the pure Mg interface is presented in Figure 5.13. Such model was based on some experimental data. First, from the impedance diagrams and its homothetic behavior previously shown, it can be inferred that the Mg active surface area may change over time. It was related to the formation of holes on the thin oxide layer (MgO) and also to the growth of the thick corrosion layer ($Mg(OH)_2$). Second, there is a diffusion process occurring on the Mg surface and the change of the electrode rotation rate do not change the amplitude of this time constant, and it is directly linked to the formation of the corrosion layer.

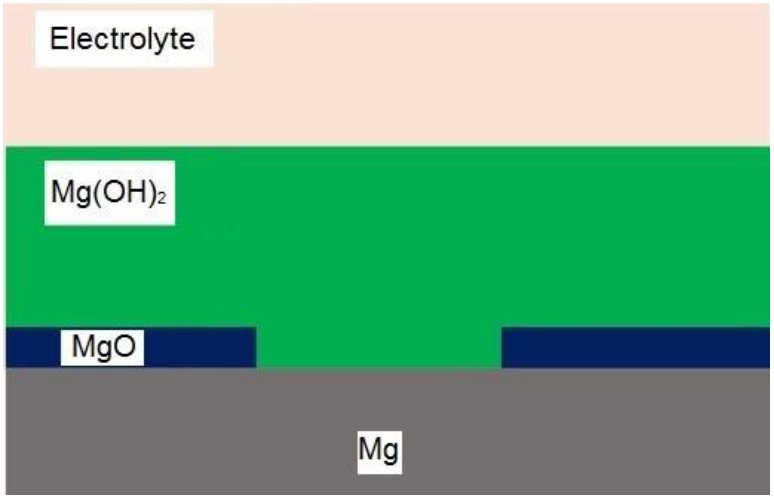

Figure 5.13 - Sketch of the interface describing the different layers formed during the Mg corrosion. According to the impedance data analysis, the MgO layer thickness is about 5-7 nm (Figure 5.17) and the $Mg(OH)_2$ layer thickness is about 20-30 μm (Figure 5.20).

From the above results, a detailed description of the impedance response can be provided accounting for both, the corrosion mechanism of the Mg in sulfate solution and the interfacial capacitance of the electrode. Unlike most of the literature, we provide a mechanistic description of the corrosion mechanism in terms of elementary reactions together with the analysis of the CPE behavior accounting for the thin oxide film at the Mg surface. Such an approach allows to avoid the use of equivalent electrical circuits and allows to demonstrate the significant role played by the adsorbates on the corrosion mechanism.

At E_{corr}, the description of the corrosion mechanism of a metal accounts for both the anodic and the cathodic processes, resulting in a null net current. In the case of Mg, the impedance results (Figure 5.12 and Figure 5.14) showed that, at E_{corr} and for low anodic potential values, the impedance diagrams show the same time constants, the impedances only increased by a multiplying factor depending on the immersion time. Thus, it can be concluded that the Mg dissolution dominates the impedance response and in the following, only the anodic reaction was taken into account to describe the dissolution mechanism of Mg, that is valid at E_{corr} and for low anodic overpotentials.

Moreover, the steady-state anodic curve and the inductive loop observed on all the EIS diagrams suggest that the mechanism involved an adsorbed intermediate. Hence, it is proposed a corrosion mechanism involving the $\mathrm{Mg}^{+}_{\mathrm{ads}}$ species that remains as active sites on the electrode surface. Interestingly, such an intermediate has been previously proposed by Baril et al. (2007) [53] and is also in agreement with the recent works of Taylor (2016) [172] and Yuwono et al. (2017) [34] involving the formation of adsorbed intermediates at the electrode

surface leading to the formation of hydrogen bubbles.

Thus, in the film-free areas, two successive anodic reactions occur (Eqs. (5.1) and (5.2)):

$$\mathrm{Mg} \xrightarrow{\mathrm{k_1}} \mathrm{Mg^+_{ads}} + \mathrm{e^-} \tag{5.1}$$

and

$$\mathrm{Mg^+_{ads}} \underset{\mathrm{k_{-2}}}{\overset{\mathrm{k_2}}{\rightleftharpoons}} \mathrm{Mg^{2+}} + \mathrm{e^-} \tag{5.2}$$

where k_i and k_{-i} are the forward and the backward rate constants of the reaction i, respectively and expressed in $\mathrm{cm^{-2}\,s^{-1}}$.

Assuming that the kinetic constants of the electrochemical reactions follow the Tafel's law, each reaction has a normalized time constant $\mathrm{K_i}$ corresponding to its rate constant $\mathrm{k_i}$ (Eq. (5.3)):

$$\mathrm{K_i} = \mathrm{k_i}\,\exp[\pm b_i(E - E^0)] \tag{5.3}$$

where b_i is the activation coefficient (in $\mathrm{V^{-1}}$) and $E - E^0$ the applied overpotential concerning the origin of potentials, E^0. The sign in the exponential term is positive for an oxidation reaction and negative for a reduction reaction. In the following, the origin of potentials is chosen as the corrosion potential obtained after reaching the steady-state, and thus, $V = E - E_{corr}$.

For the NDE, which is a chemical reaction of the Mg^+_{ads}, formed on the Mg surface, with water to produce dihydrogen (Eq. (5.4)) the increase of the magnitude of the inductive loop, observed on the EIS diagrams as a function of the applied potential (Figure 5.14), indicated that the surface coverage by the adsorbed species also increased with the potential. Such behavior is in agreement with the relaxation of adsorbed species [56], [173] and also with the increase of the $\mathrm{H_2}$ formation when the potential of the Mg electrode is shifted towards anodic values. It is thus proposed that the NDE occurs only with the Mg^+_{ads}, and expresses as:

$$\mathrm{Mg^+_{ads}} + \mathrm{H_2O} \xrightarrow{\mathrm{k_3}} \mathrm{Mg^{2+}} + \mathrm{OH^-} + \frac{1}{2}\mathrm{H_2} \tag{5.4}$$

Assuming that the adsorbate Mg^{+}_{ads} obeys a Langmuir's isotherm with a maximum number of sites per surface unit β, and a fraction of surface coverage θ, the charge, and mass balance express as:

$$\beta \frac{d\theta}{dt} = K_1(1-\theta) - K_2\beta\theta + K_{-2}C_{Mg^{2+}} - k_3\beta\theta \tag{5.5}$$

and

$$D\frac{C_{Mg^{2+}}}{\delta_{corr}} = K_2\beta\theta - K_{-2}C_{Mg^{2+}} + k_3\beta\theta \tag{5.6}$$

where $C_{Mg^{2+}}$ is the interfacial concentration of Mg^{2+} in solution. δ_{corr} is the total thickness of the corrosion product layer. It should be recalled that δ_{corr} accounts for the thickness of the $Mg(OH)_2$ and is different from the MgO film thickness (δ_{ox}), that can be determined from the capacitance plots (Figure 5.16). The faradaic current is the sum of each elemental step and expresses as:

$$i_F = FA\left[K_1(1-\theta) + K_2\beta\theta - K_{-2}C_{Mg^{2+}}\right] \tag{5.7}$$

where F is the Faraday constant, and A is the electrode surface area.

At steady-state, $\frac{d\theta}{dt} = 0$, which leads to the determination of steady-state Mg^{2+} concentration and surface coverage as:

$$\theta_{stat} = \frac{K_1 + K_{-2}C_{Mg^{2+}}}{K_1 + K_2\beta + k_3\beta} \tag{5.8}$$

and

$$C_{Mg^{2+}} = \frac{(K_2 + k_3)\beta\theta_{stat}}{\frac{D}{\delta_{corr}} + K_{-2}} \tag{5.9}$$

Thus

$$\theta_{stat} = \frac{K_1\left(\frac{D}{\delta_{corr}} + K_{-2}\right)}{K_1\left(\frac{D}{\delta_{corr}} + K_{-2}\right) + (K_2 + k_3)\beta\frac{D}{\delta_{corr}}} \tag{5.10}$$

The linearization of the governing equations allows the calculation of the faradaic impedance as the solution of the linear system of equations Eqs. (5.11)-(5.13):

$$j\omega\beta\Delta\theta = -(K_1 + K_2\beta + k_3\beta)\Delta\theta + \left(K_1 b_1 - K_1 b_1\theta - K_2 b_2\beta\theta - K_{-2} b_{-2} C_{Mg^{2+}}\right)\Delta V + K_{-2}\Delta C_{Mg^{2+}} \tag{5.11}$$

$$\left(j\omega\beta + K_1 + \beta(K_2 + k_3)\right)\Delta\theta = \left(K_1 b_1(1-\theta) - K_2 b_2\beta\theta - K_{-2} b_{-2} C_{Mg^{2+}}\right)\Delta V + K_{-2}\Delta C_{Mg^{2+}} \tag{5.12}$$

$$\frac{\Delta i_F}{FA} = (K_2\beta - K_1)\Delta\theta + \left(K_1 b_1 - K_1 b_1\theta_1 + K_2 b_2\beta\theta + K_{-2} b_{-2} C_{Mg^{2+}}\right)\Delta V - K_{-2}\Delta C_{Mg^{2+}} \tag{5.13}$$

The concentration variation $\Delta C_{Mg^{2+}}$ inside a finite diffusion layer of thickness δ_{corr} is given by the solution of the second Fick's law using the Nernst hypothesis [56] through Eqs. (5.14) and (5.15):

$$\frac{\Delta C_{Mg^{2+}}}{\Delta i_F} = -\frac{1}{FAD}\frac{tanh\left\{\delta_{corr}\sqrt{\frac{j\omega}{D}}\right\}}{\sqrt{\frac{j\omega}{D}}} = -\frac{1}{FA}N(\omega) \tag{5.14}$$

with

$$N(\omega) = \frac{tanh\left\{\delta_{corr}\sqrt{\frac{j\omega}{D}}\right\}}{\sqrt{j\omega D}} \tag{5.15}$$

Then, the faradaic contribution to the impedance can be calculated as:

$$Z_F(\omega) = \frac{\Delta V}{\Delta i_F} \tag{5.16}$$

$$1 - FA(K_2\beta - K_1)\frac{\Delta\theta}{\Delta i_F} + FAK_{-2}\frac{\Delta C_{Mg^{2+}}}{\Delta i_F} = FA\left(K_1 b_1 - K_1 b_1 \theta_1 + K_2 b_2 \beta\theta + K_{-2} b_{-2} C_{Mg^{2+}}\right)\frac{\Delta V}{\Delta i_F} \tag{5.17}$$

$$\Delta\theta = \frac{\left(K_1 b_1(1-\theta) - K_2 b_2 \beta\theta - K_{-2} b_{-2} C_{Mg^{2+}}\right)}{\left(j\omega\beta + K_1 + \beta(K_2 + k_3)\right)}\Delta V + \frac{K_{-2}}{\left(j\omega\beta + K_1 + \beta(K_2 + k_3)\right)}\Delta C_{Mg^{2+}} \tag{5.18}$$

$$FA\left(K_1 b_1 - K_1 b_1 \theta_1 + K_2 b_2 \beta\theta + K_{-2} b_{-2} C_{Mg^{2+}}\right)\frac{\Delta V}{\Delta i_F} = 1 - FA(K_2\beta - K_1)\frac{\left(K_1 b_1(1-\theta) - K_2 b_2 \beta\theta - K_{-2} b_{-2} C_{Mg^{2+}}\right)}{\left(j\omega\beta + K_1 + \beta(K_2 + k_3)\right)}\frac{\Delta V}{\Delta i_F} + FA(K_2\beta - K_1)\frac{K_{-2}}{\left(j\omega\beta + K_1 + \beta(K_2 + k_3)\right)}\frac{\Delta C_{Mg^{2+}}}{\Delta i_F} - FAK_{-2}\frac{\Delta C_{Mg^{2+}}}{\Delta i_F} \tag{5.19}$$

$$FA\left\{\left(K_1 b_1(1-\theta) + K_2 b_2 \beta\theta + K_{-2} b_{-2} C_{Mg^{2+}}\right) + (K_2\beta - K_1)\frac{\left(K_1 b_1(1-\theta) - \left(K_2 b_2 \beta\theta + K_{-2} b_{-2} C_{Mg^{2+}}\right)\right)}{\left(j\omega\beta + K_1 + \beta(K_2 + k_3)\right)}\right\}\frac{\Delta V}{\Delta i_F} = 1 + K_{-2}N(\omega)\left\{1 - \frac{(K_2\beta - K_1)}{\left(j\omega\beta + K_1 + \beta(K_2 + k_3)\right)}\right\} \tag{5.20}$$

Assuming

$$r_1 = K_1 b_1(1-\theta) \tag{5.21}$$

and

$$r_2 = K_2 b_2 \beta\theta + K_{-2} b_{-2} C_{Mg^{2+}} \tag{5.22}$$

The faradaic impedance express as:

$$Z_F(\omega) = \frac{\Delta V}{\Delta i_F} = \frac{1 + K_{-2}N(\omega)\left\{1 - \frac{(K_2\beta - K_1)}{[j\omega\beta + K_1 + \beta(K_2 + k_3)]}\right\}}{FA\left\{(r_1 + r_2) + \frac{(K_2\beta - K_1)(r_1 - r_2)}{[j\omega\beta + K_1 + \beta(K_2 + k_3)]}\right\}} \quad (5.23)$$

The overall impedance is then obtained by taking into account the contribution of the interfacial capacitance, $Z_{oxide}(\omega)$, and the electrolyte resistance, R_e (Eq. (5.24)):

$$Z(\omega) = R_e + \frac{Z_F(\omega) \text{ x } Z_{oxide}(\omega)}{Z_F(\omega) + Z_{oxide}(\omega)} \quad (5.24)$$

5.2.2.3. Electrochemical impedance diagrams at low anodic over potentials

Figure 5.14a shows impedance diagrams of the Mg electrode after 12 h of immersion in 0.1 mol L^{-1} Na_2SO_4 solution (Ω = 1000 rpm) at E_{corr} for two low anodic overpotentials (blue squares and red triangles for E_{corr} + 10 mV and E_{corr} + 20 mV, respectively). These polarization potentials correspond to steady-state anodic current densities of 100 µA.cm^{-2} and 220 µA.cm^{-2}, respectively (Figure 5.10). It can be seen that the global shape of the two impedance diagrams is independent of the applied potential and shows the same time constants as those previously described, indicating that the same mechanism occurs at E_{corr} and for low anodic overpotentials.

Figure 5.14b shows the dimensionless representation of the EIS diagrams obtained from the normalization by the maximum value of the real part of each spectrum presented in Figure 5.14a. It can be seen that each time constant slightly depends on the potential. In particular, the amplitude of the low-frequency inductive loop increases with the potential, regardless of the variation of the active surface area. Such observation has been already reported for this inductive feature, but only to evaluate the Mg dissolution rate [54]. Indeed, this inductive contribution can be ascribed to an adsorbed intermediate relaxation and fulfill the hypothesis of the surface coverage relaxation with the potential.

In the present case, within the small anodic potential domain investigated, the Mg^+_{ads} surface coverage increases with the potential. it should also be mentioned that the existence of adsorbed intermediates has been proposed for many different systems, regardless of the used technique, impedance spectroscopy or polarization curves [174]–[176].

The high and intermediate frequency domain corresponding to the charge transfer resistance in parallel to the interfacial capacitance and diffusion of species through the $Mg(OH)_2$

layer, respectively, are slightly affected by the change in potential. For anodic overpotential, there was no significant variation of charge transfer or a clear tendency between the anodic potential and charge transfer. It was due to the influence of experimental time in the potential.

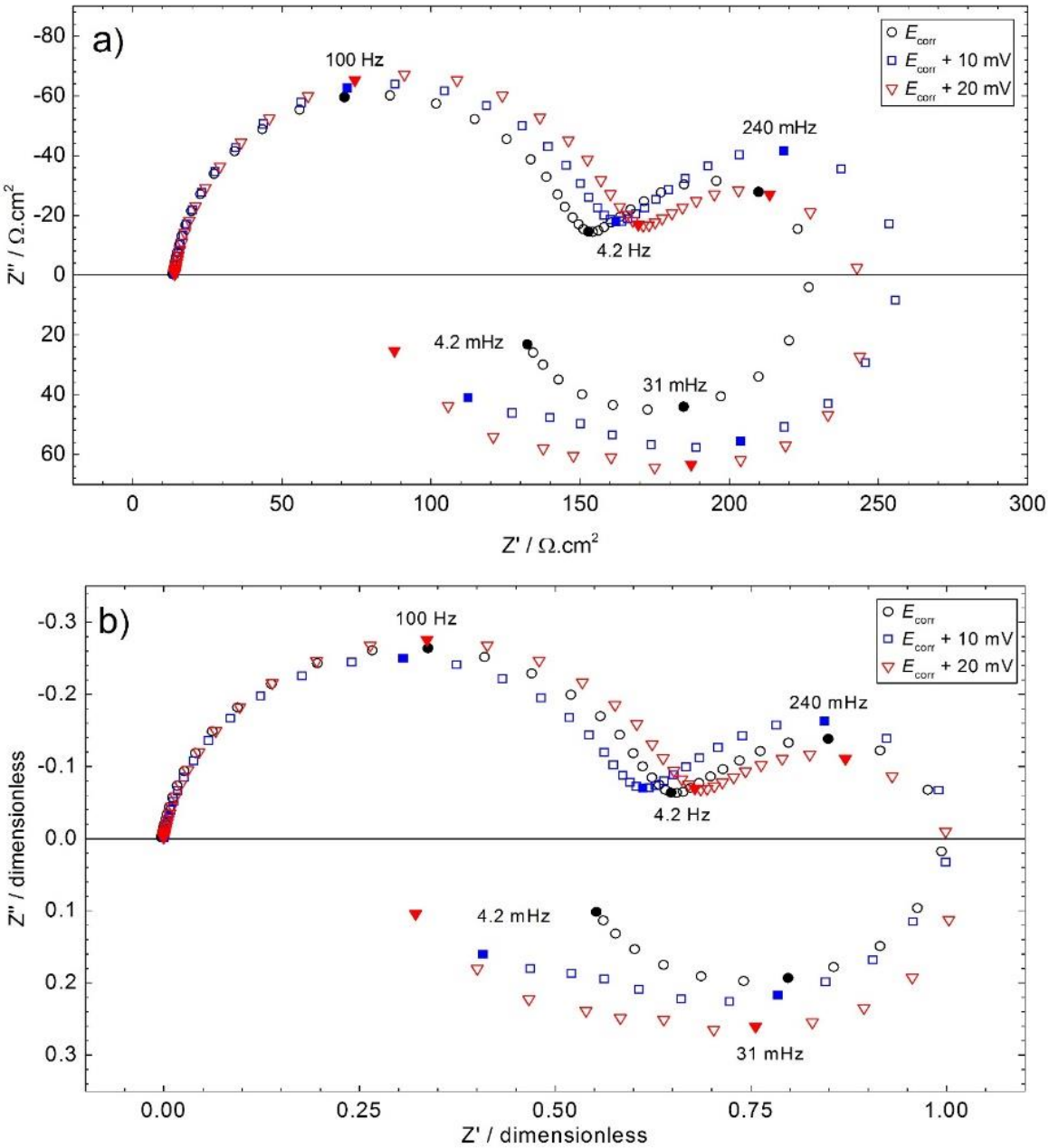

Figure 5.14 - Electrochemical impedance diagrams of pure Mg after 12 hours of immersion in 0.1 mol.L^{-1} Na_2SO_4 solution at E_{corr} (Ω = 1000 rpm) for two anodic overpotentials: a) raw impedance diagrams (Nyquist representation) and b) normalized impedance diagrams (each diagram was normalized by the maximum value of the real part of the impedance).

5.2.2.4. Interfacial capacitance

The impedance results presented in Figure 5.12 and Figure 5.14, show that the high-frequency response, corresponding to the charge transfer resistance in parallel with the interfacial capacitance, is characterized by a flattened capacitive loop, i.e., a non-ideal capacitive behavior.

Graphical analysis of the results allows a constant phase element (CPE) to be clearly evidenced in the high-frequency domain (Figure 5.15a) and the α parameter of the CPE can be determined from the variation of the imaginary part of the impedance (in absolute value) as a function of the frequency (Figure 5.15b) [56], [177]. The impedance of the CPE is given by Eq. (5.25).

$$Z_{CPE} = \frac{1}{Q(j\omega)^{\alpha}} \tag{5.25}$$

In Figure 5.15a, it can be seen that the phase angle value on the plateau, for the corrected curve, is -79°. Thus, the CPE parameter is equal to 79/90 = 0.88, in agreement with the value determined in Figure 5.15b from the variations of the imaginary part of the impedance as a function of the frequency. The plateau observed at high-frequency is characteristic of a pure CPE behavior which may be the consequence of a resistivity distribution along the thin oxide film thickness. This CPE behavior can be analysed by the power-law model [178], [179]. However, the use of the power-law model introduces a large number of parameters that can be difficult to obtain from the fit of experimental data. Thus, it was chosen another approach for evaluating the capacitance.

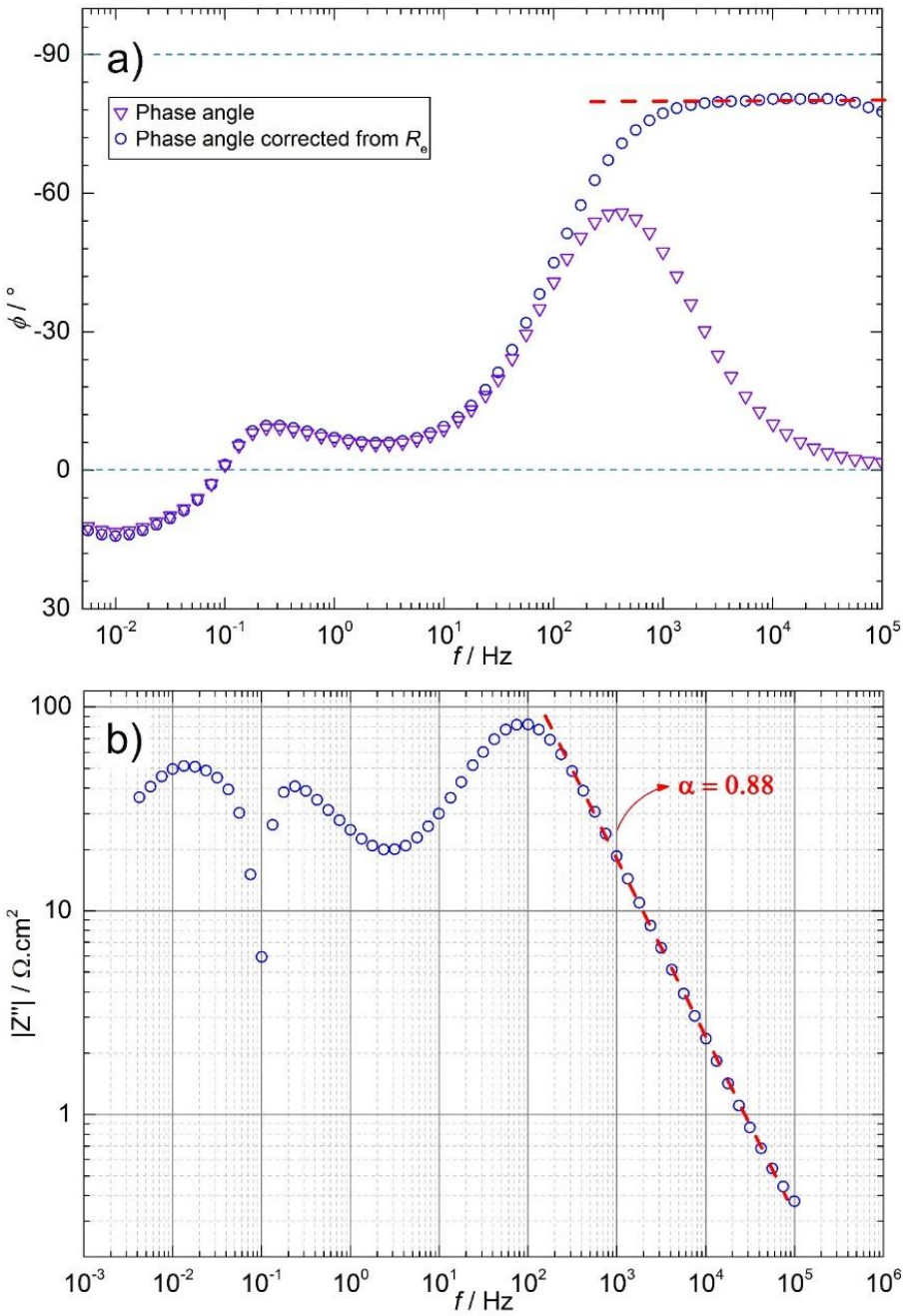

Figure 5.15 - Electrochemical impedance response of pure Mg after 35 hours of immersion in 0.1 mol.L^{-1} Na_2SO_4 solution at E_{corr} (Ω = 1000 rpm). a) Variations of the phase angle (circle) and corrected phase angle from the ohmic resistance (triangle) as a function of the frequency; b) variations of the absolute value of the imaginary part of the impedance as a function of the frequency.

The capacitance of the oxide film can be extracted from the impedance data by using the complex capacitance representation [119], [180] and then, the oxide film thickness can be calculated. It was shown that this methodology allows an easy determination of the oxide film thickness that agrees well with the results obtained with other techniques, such as XPS [57] or reflectometry [60]. A similar methodology has been recently used to investigate the stability of

the oxides film formed on a Mg alloy containing rare-earth elements [20]. Thus, in a first step, the film capacitance was graphically determined from the EIS response through the relationship (Eq. (5.26)):

$$C(\omega) = \frac{1}{j\omega[Z_F(\omega) - R_e]} \tag{5.26}$$

where Z_F is the impedance of the Mg electrode and R_e is the electrolyte resistance, which can be determined from the high-frequency limit of the impedance diagram.

The results presented in Figure 5.16 show an example of the complex-capacitance plot obtained from the impedance response of the Mg electrode after 35 h of immersion in 0.1 mol.L^{-1} Na_2SO_4 solution at E_{corr}.

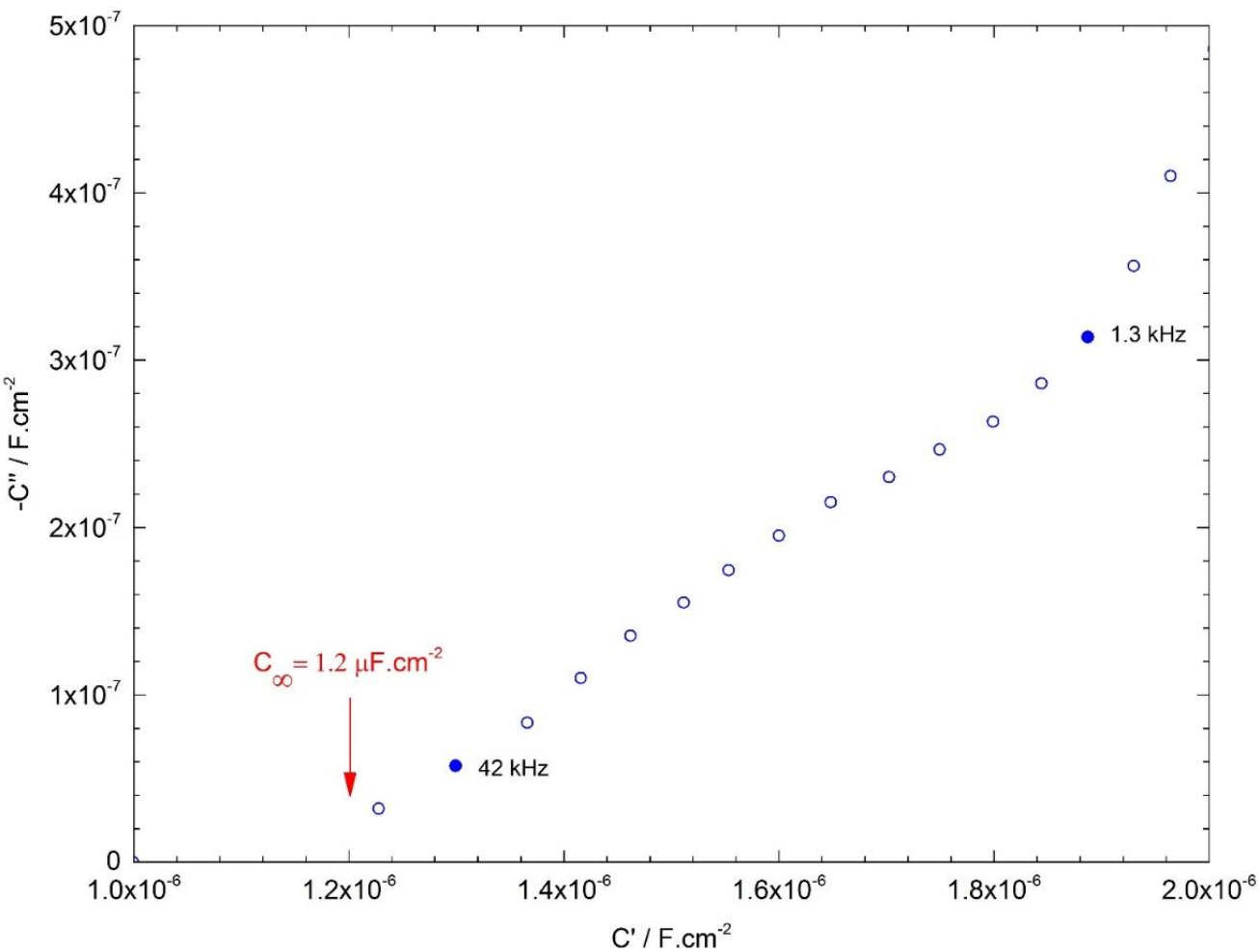

Figure 5.16 - Complex-capacitance plot obtained from the electrochemical impedance response of Mg after 35 h of immersion in a 0.1 mol.L^{-1} Na_2SO_4 solution (Ω = 1000 rpm) from the data presented in Figure 5.12 using Eq. (3). The axis is not orthonormal to make the extrapolation to the C_∞ axis better visible.

From the HF frequency limit of the impedance, C_∞, the dielectric capacitance of the thin MgO oxide film formed at the electrode surface can be determined. The thin oxide film thickness, δ_{ox}, was afterward calculated from the usual relationship assuming a parallel plate capacitor (Eq. (5.27)):

$$C_\infty = \frac{\varepsilon\varepsilon_0}{\delta_{ox}} \tag{5.27}$$

where ε and ε_0 are the relative permittivity of the thin oxide film and the vacuum permittivity (ε_0 = 8:85 x 10^{-14} F.cm^{-1}), respectively. Assuming a permittivity value of 9 for MgO [181], this leads to an oxide film thickness of 6.6 nm for the results presented in Figure 5.16. The oxide film thickness was calculated from all the impedance spectra obtained at E_{corr} as a function of the immersion time.

The δ_{ox} values are reported in Figure 5.17 as a function of the immersion time in the Na_2SO_4 solution. The film thickness slightly increases with time from an initial value of 5.4 nm up to 7 nm after 60 h of immersion.

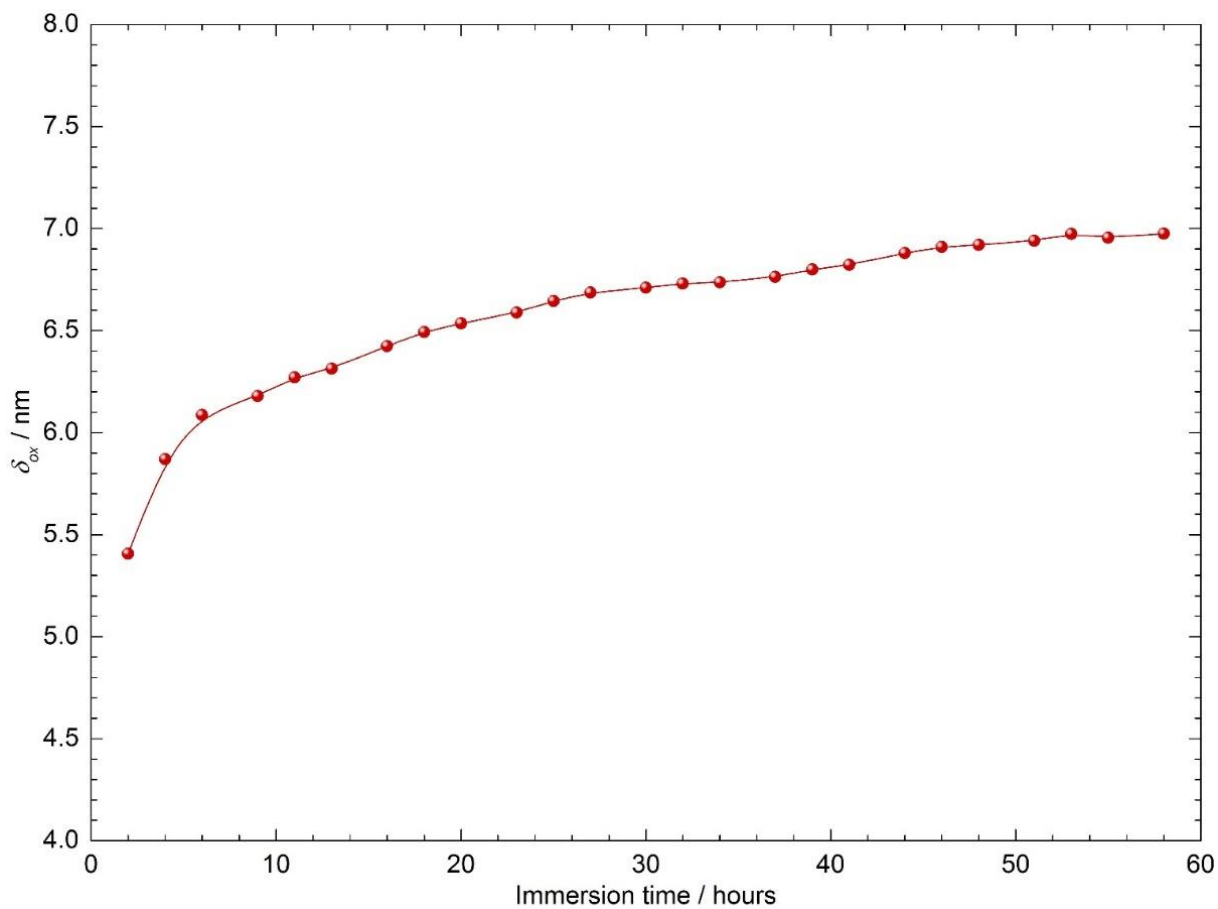

Figure 5.17 - Oxide film thickness formed on the Mg surface as a function of immersion time in 0.1 mol.L^{-1} Na_2SO_4 solution (Ω = 1000 rpm). Each point of this curve corresponds to the analysis of the complex-capacitance plot, as shown in Figure 5.16.

Then, the power-law model, previously introduced to account for a normal distribution of the time constants at an interface [178], [179], was used for describing the impedance contribution of the oxide film and is given by the general formula (Eq. (5.28)):

$$Z_{oxide}(\omega) = \int_0^{\delta_{ox}} \frac{\rho(x)}{1 + j\omega\varepsilon\varepsilon_0\rho(x)} dx \tag{5.28}$$

in which ω is the pulsation, j the imaginary number solution of $j^2 = -1$, and $\rho(x)$ the resistivity distribution inside the film, which is expressed as a function of the normal coordinate, x, to the film as (Eq. (5.29)):

$$\rho(x) = \rho_\delta \left[\frac{\rho_\delta}{\rho_0} + \left(1 - \frac{\rho_\delta}{\rho_0}\right)\left(\frac{x}{\delta_{ox}}\right)^\gamma\right]^{-1} \tag{5.29}$$

where ρ_0 and ρ_δ are the boundary values of the resistivity at the metal/oxide interface and the oxide/solution interface, respectively. It should be mentioned that the previous step using capacitive plot allowed to evaluate δ_{ox}, thus limiting the number of unknowns in the following analysis.

It has been previously shown that this impedance has an analytical solution in a restricted frequency domain depending on the value of ρ_0 and ρ_δ [178], [179]. In the present work, the non-linear regression analysis was performed with the integral formula, which is valid over the whole frequency domain.

The parameters, ρ_0 and ρ_δ, corresponding to the interfacial capacitances were determined and are reported as a function of the immersion time in Figure 5.18. Both resistivity values at the metal/oxide interface and at the oxide/solution interface remain relatively constant.

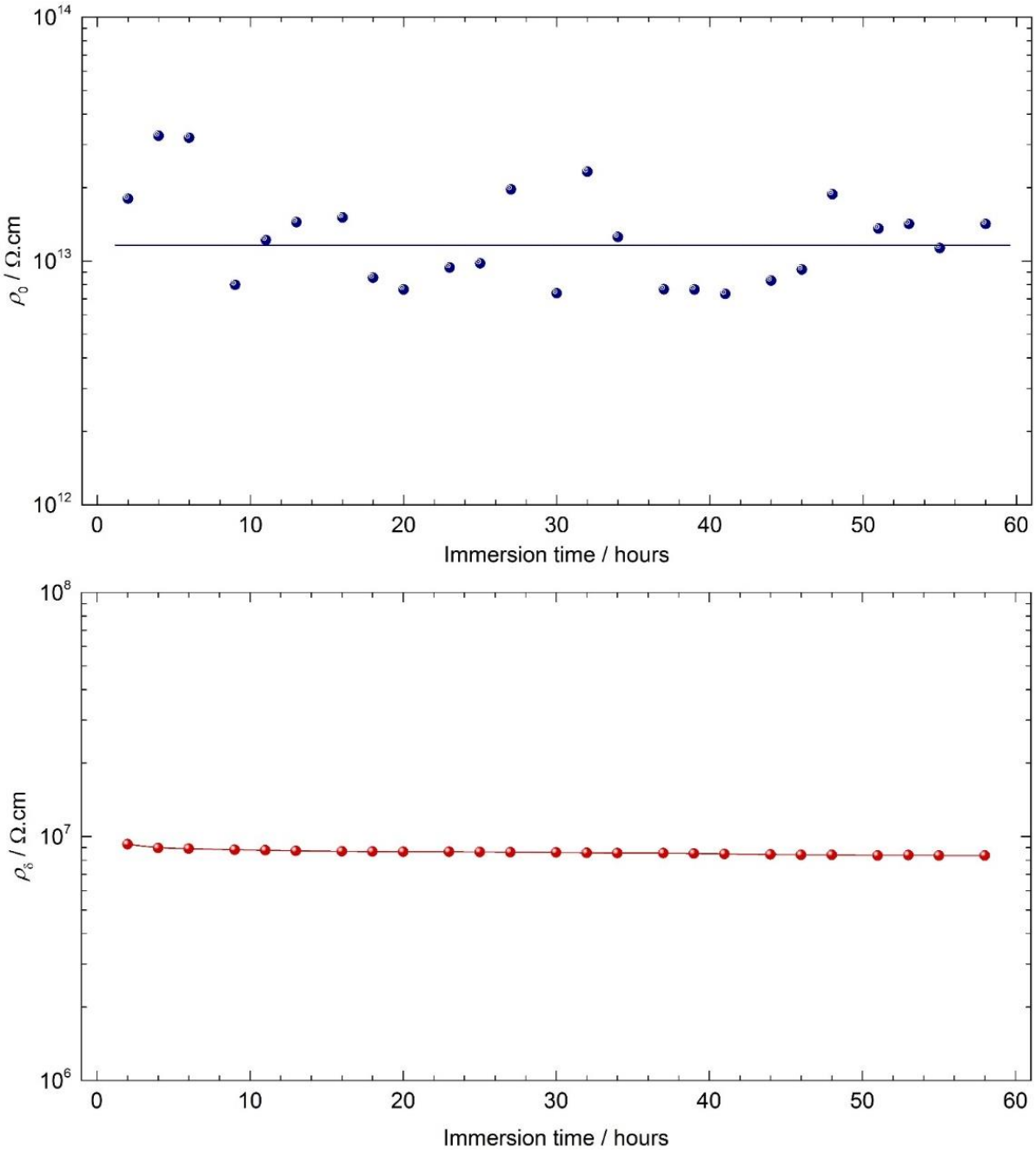

Figure 5.18 - (a) Resistivity at the metal/oxide interface and (b) at the oxide/solution interface of the MgO thin film as a function of immersion time for the corrosion of Mg in 0.1 mol.L^{-1} Na_2SO_4 solution (Ω = 1000 rpm). These data were obtained from the fitting procedure assuming a power-law model for the description of the interfacial capacitance (see text).

These values show that the MgO conductivity changes by about 6 orders of magnitude over a nanometric distance. This should be explained by the hydration of the layer that should decrease along with the thin film thickness. These constant values are also in agreement with the fact that the oxide film (MgO) mainly grows laterally over the electrode surface decreasing

the active surface area as it can be observed in the variation of the impedance diagrams with the immersion time.

Finally, it has been assumed that the thin MgO film dominates the capacitive response of the interface, that is, the surface area covered by the MgO is higher in comparison with the film-free area, and thus, the double layer capacitance is negligible. The mathematical description of this assumption is demonstrated as follows:

$$\frac{1}{C_{eq}} = \frac{1}{C_{dl}} + \frac{1}{C_{ox}} \tag{5.30}$$

if

$$C_{dl} \gg C_{ox} \Rightarrow \frac{1}{C_{dl}} \ll \frac{1}{C_{ox}} \tag{5.31}$$

In our case, C_{ox} is in the range of 1 µF.cm^{-2}, whereas C_{dl} is usually in the range of 10 - 50 µF.cm^{-2}. Thus, this approximation is valid and

$$\frac{1}{C_{dl}} + \frac{1}{C_{ox}} \cong \frac{1}{C_{ox}} \tag{5.32}$$

5.2.3. Modeling of the electrochemical response

Figure 5.19 shows the EIS diagram in Nyquist representation for the Mg electrode after 35 h immersion (blue circles). On the same graph, the result of the non-linear regression with the proposed model (Eqs. (5.23) and (5.24)) is reported (red crosses). This non-linear regression was performed with an in-house made software based on a simplex algorithm allowing analytical expression of the impedance and the conductivity to be used.

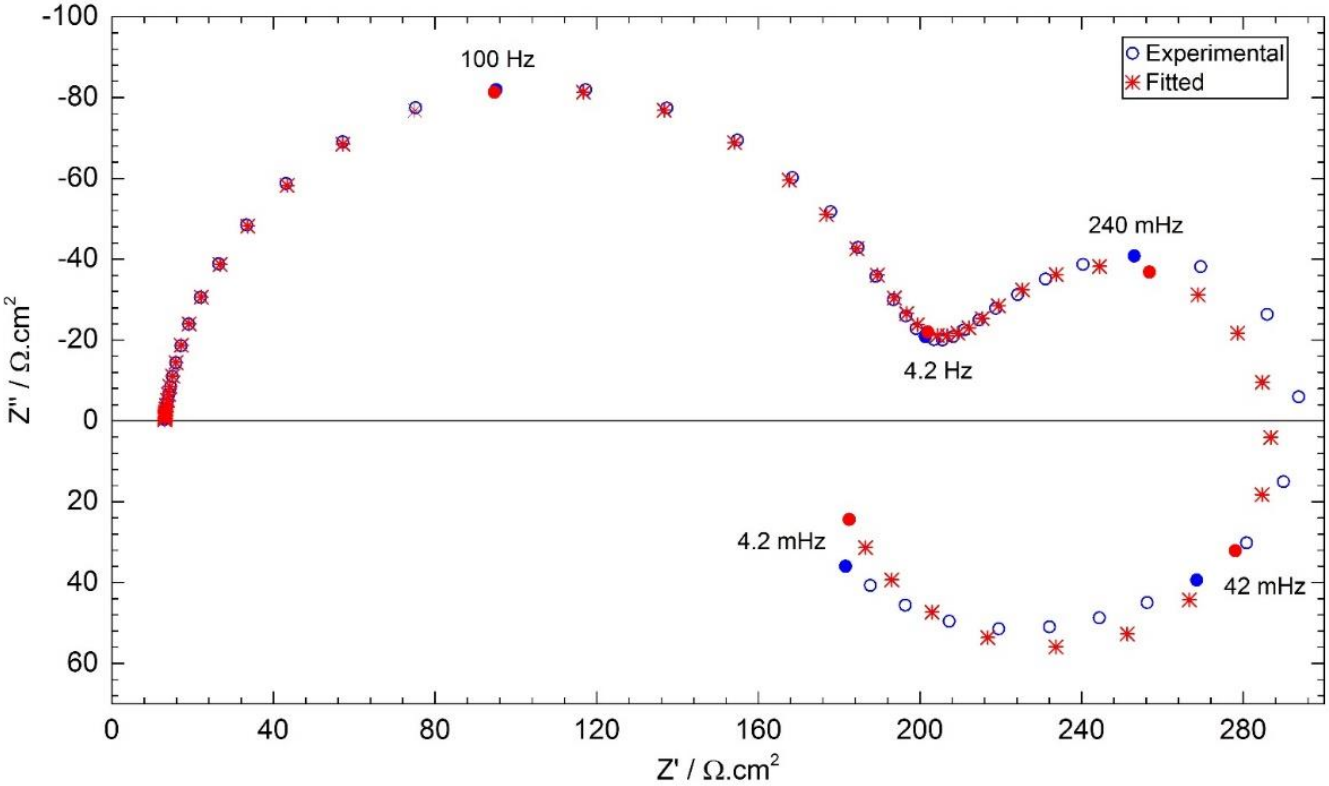

Figure 5.19 - Impedance response of Mg after 35 h of immersion in 0.1 mol.L^{-1} Na_2SO_4 solution (Ω = 1000 rpm) in a Nyquist representation (blue circles) and fitting of the EIS response with the model (Eqs. (22) and (25)) (red crosses). The fitted diagram corresponds to the following parameters: b_1 = 28.9 V^{-1}, b_2 = 11.8 V^{-1}, b_{-2} = 9.3 V^{-1}, k_1 = 2.32 x 10^{-10} cm^2.s^{-1}, k_2 = 9.35 x 10^{-2} cm^2.s^{-1}, k_{-2} = 7.58 x 10^{-4} cm^2.s^{-1}, k_3 = 8.16 x 10^{-3} cm^2.s^{-1}, δ_{corr} = 22.2 µm, δ_{ox} = 6.7 nm, D = 3 x 10^{-6} cm^2.s^{-1}, β = 10^{-6} mol.cm^{-2}.

A detailed analysis of the EIS diagrams presented in Figure 5.12 and Figure 5.14 was performed with the model, and in the following, the results of this analysis and the variations of the most significant parameters are presented and discussed. The electrolyte resistance remains constant as a function of immersion time. Such behavior is expected since R_e is measured in the high-frequency domain. It also only depends on the geometry of the electrochemical cell, and in particular of the electrode size. Thus, for the fitting procedure, the R_e value was graphically determined and then used as a constant. Similarly, the thin oxide film thicknesses (δ_{ox}) determined from the complex-capacitance diagrams (Figure 5.17) were also fixed in the fitting procedure.

Hence, the number of parameters to be adjusted was smaller, allowing a higher accuracy for the remaining parameters. It should also be underlined that this model enables to explain both, the dissolution kinetics of Mg with a two-elementary step reaction mechanism and the NDE phenomenon is in agreement with the experimental results of the literature [18], [22], [24]–[26].

From the fitting procedure, the thickness of the $Mg(OH)_2$ layer formed on the electrode surface during the corrosion process can be readily obtained. Its variation as a function of the immersion time in the Na_2SO_4 solution is presented in Figure 5.20.

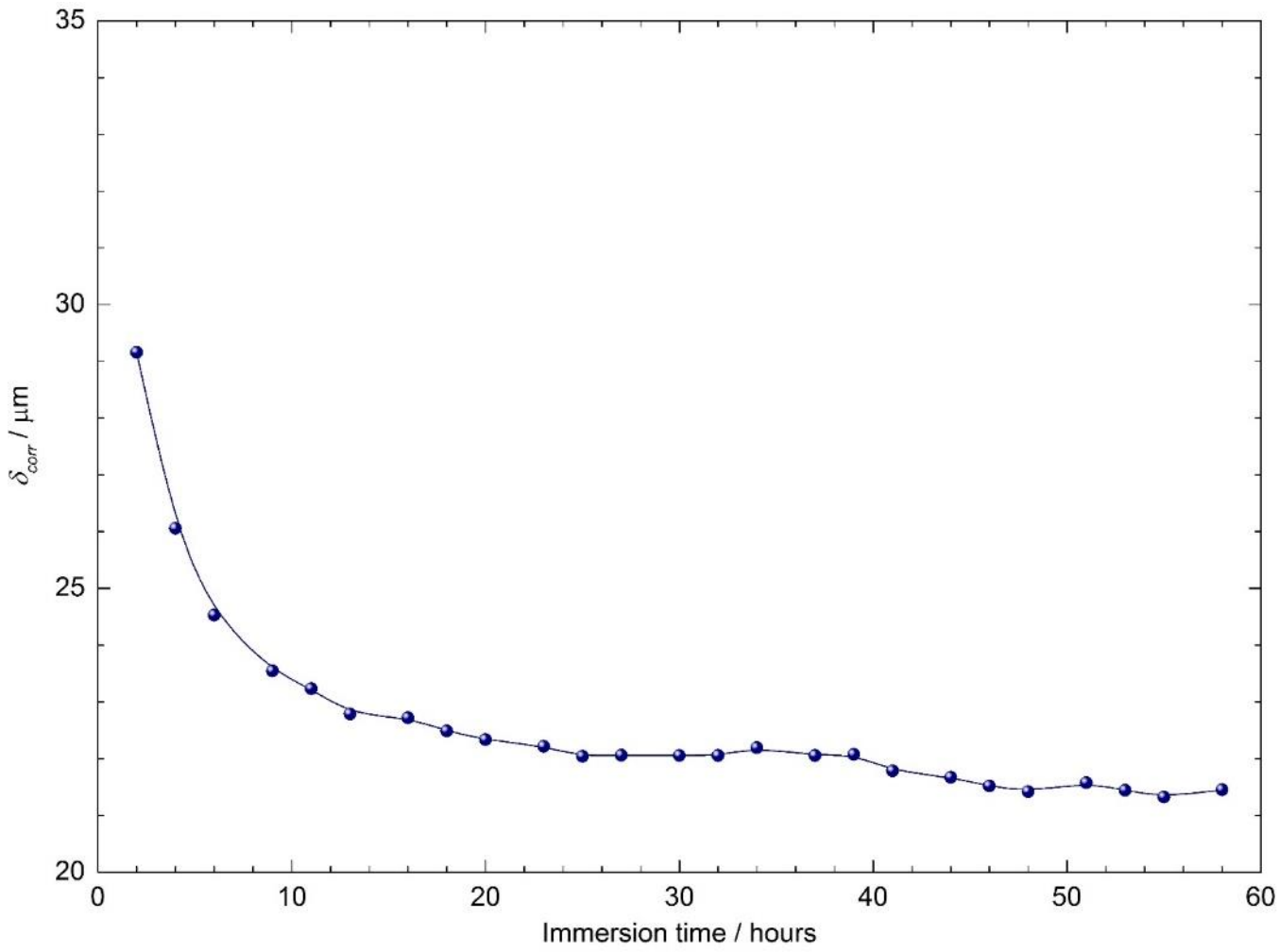

Figure 5.20 - Total thickness of the corrosion layer formed on Mg surface as a function of immersion time in 0.1 mol.L^{-1} Na_2SO_4 solution (Ω = 1000 rpm) obtained from the fitting of the impedance diagram, as exemplified in Figure 5.19.

It decreases from 29 µm to 21 µm from the first hours of immersion to about 60 h. A thickness, in the same order of magnitude (15 µm), has been measured from *ex situ* SEM examination of the cross section of the $Mg(OH)_2$ layer formed on a Mg sample after 21 h of immersion in a sodium sulfate solution [51]. Most of the variation of the layer thickness is observed during the first hours of immersion. Indeed, no corrosion product was initially present, and the thickness variation in the first hours is a result of two phenomena: the convective

diffusion of redox species in solution for short immersion time (i.e. during the formation of the corrosion layer, the thickness of the Nernst layer being in the range of 20 μm for a RDE at 1000 rpm), and then the diffusion inside the corrosion layer for longer immersion time. After 20 h, it is assumed that a steady-state is reached between the formation and the dissolution of the $Mg(OH)_2$ layer.

The calculation of the surface coverage by the adsorbate $\mathrm{Mg}^{+}_{\mathrm{ads}}$ with Eq. (5.10) and the regressed parameters showed a variation of θ_{stat} that increased during the 10 first hours from 2×10^{-3} to 4×10^{-3}. Then, it decreased down to 3×10^{-3}, in agreement with the progressive formation of the corrosion products layer that partially hindered the surface reactivity. Moreover, from Eq. (5.9), the interfacial concentration of Mg^{2+} was calculated. Values in the range of a few 10^{-7} mol.L^{-1} were obtained, that is, 2 - 3 orders of magnitude lower than the solubility limit of $Mg(OH)_2$ for a pH of about 10 [50], [51]. Such a value is in agreement with a local pH increase at the Mg surface and the presence of a concentration gradient in the close vicinity of the electrode.

In contrast, the variation of the different kinetic constants, which were obtained from the fitting of the different time constants, cannot be directly interpreted. Indeed, the evolution of the EIS diagrams as a function of the immersion time strongly depends on the variation of the active surface area, and thus the fitted parameters, obtained from the raw data, must be corrected from the surface area variation. The evolution of the active surface area was calculated from the charge transfer resistance, determined from the diameter of the first capacitive loop of the impedance diagram for each immersion time and by using the first measurement (after 2 h of immersion) as the reference value. The results are presented in Figure 5.21.

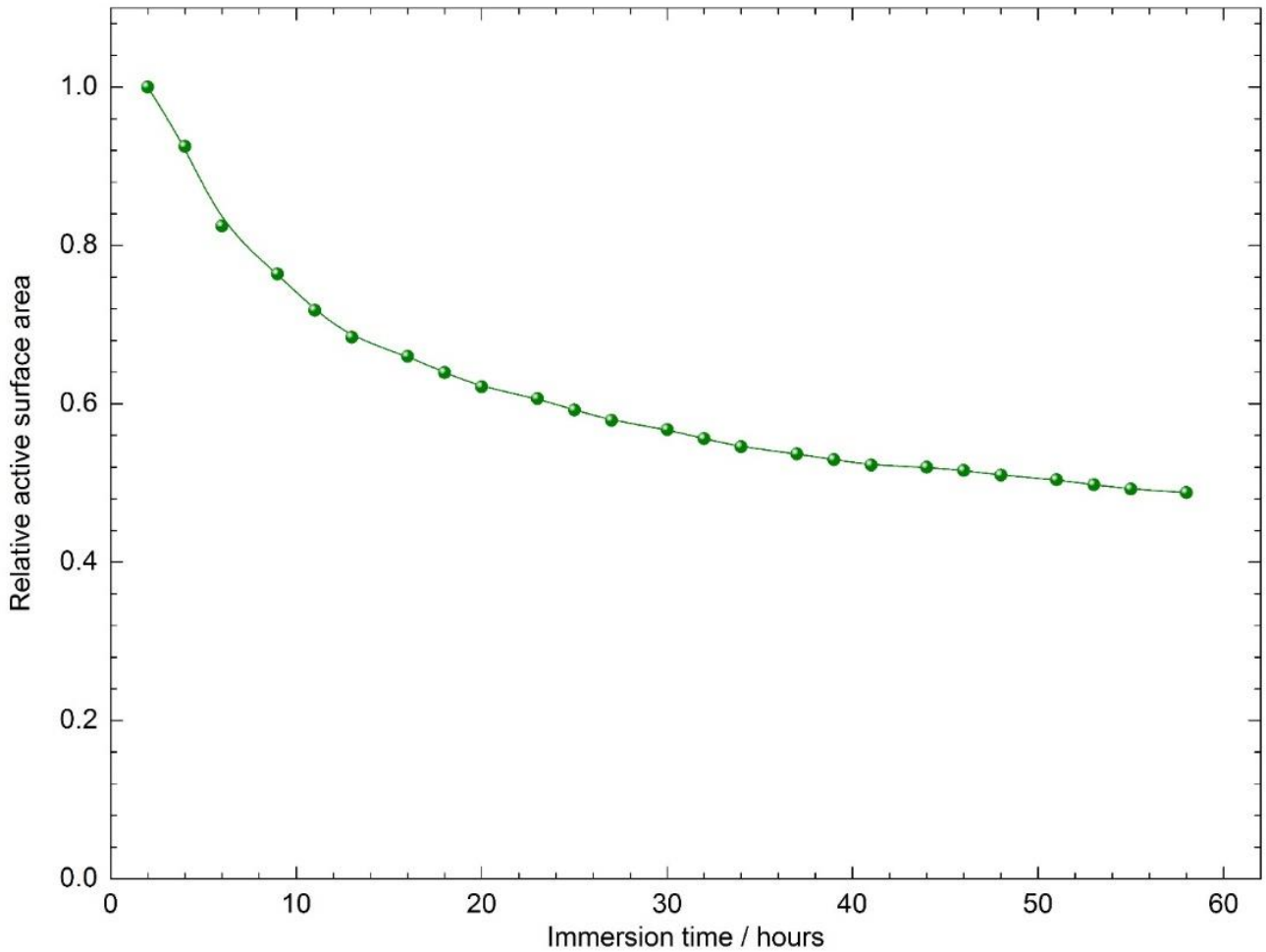

Figure 5.21 - Active surface area evolution as a function of the immersion time for Mg in 0.1 mol.L^{-1} Na_2SO_4 solution (Ω = 1000 rpm). The relative surface area was calculated from the charge transfer resistance, determined from the diameter of the first capacitive loop of the impedance diagram for each immersion time (Figure 5.12) and by using the first measurement performed, after 2 h of immersion, as the reference value.

It should be noted that the same result is obtained if the active surface area is calculated from the maximum value of the real part of the impedance diagrams as it was done for performing the normalization of the EIS spectra presented in Figure 5.12. A significant decrease of the active surface with time can be observed (in other words, an increase of the electrode surface area covered by the oxide layer), which is about half of the initially active surface, after 60 h of immersion.

Even if the active surface area cannot be accurately determined and should represent a small fraction of the whole electrode surface, the obtained variation underlines that the oxide film does not entirely cover the electrode surface, i.e., a free-film area remains present on the Mg surface. This is in agreement with the Pilling - Bedworth (PB) ratio. For pure MgO, the PB ratio is smaller than 1 (0.8) indicating that the MgO oxide film cannot fully cover the Mg surface [26], [182].

The fitting procedure allows all the parameters of the model to be determined. The variations of the kinetic constants, k_1 and k_2, and the related Tafel parameters, b_1 and b_2, are presented in Figure 5.22 as a function of time.

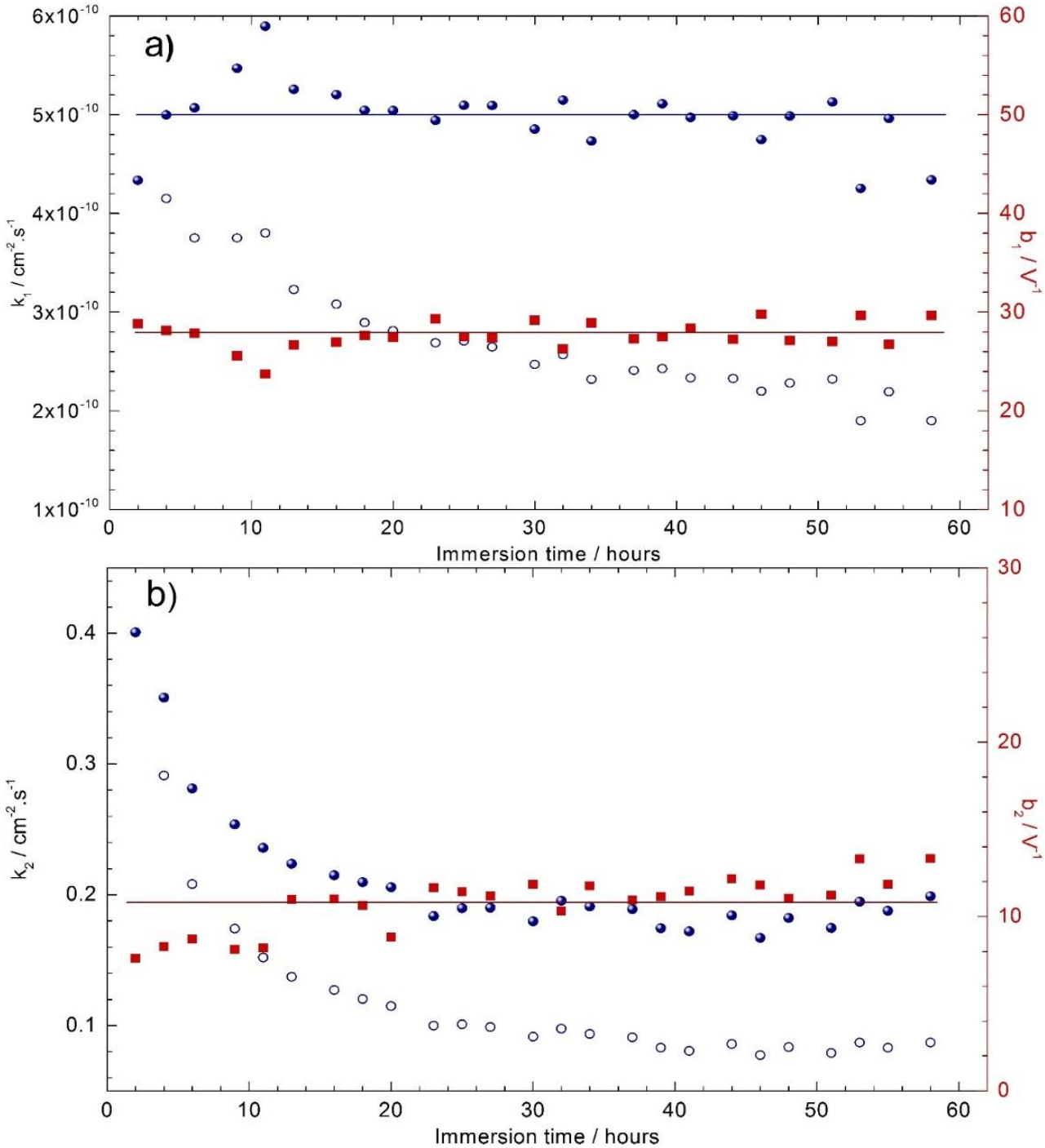

Figure 5.22 - Kinetic parameters evolution corresponding to a) k_1 related to reaction 5.6 and b) k_2 related to reaction 5.7 as a function of immersion time for the corrosion of Mg in 0.1 mol.L^{-1} Na_2SO_4 solution (Ω = 1000 rpm). The blue open circles correspond to the raw kinetic constant determined from the fitting procedure; the plain blue circles are the same data corrected from the surface variations (see text); the red squares correspond to the variation of the Tafel coefficient.

The variation of the raw values of k_1 (open blue circles - Figure 5.22a) shows a decrease of the kinetic constant with time. However, the active surface area also varies as a function of time (Figure 5.21), and the apparent kinetic parameters obtained from the impedance variations can be described as extensive parameters. The variations of k_1 have to be corrected from the active surface area variations (plain blue circles - Figure 5.22a), thus showing that this electrochemical kinetic parameter is time independent.

The Tafel's coefficient, b_1 (red squares - Figure 5.22a) is independent of the immersion time. It should be noted that this parameter, the units of which are V^{-1}, is to be seen as an intensive parameter, i.e., independent of the surface variation. It is thus concluded that the first step of the anodic dissolution is neither modified by the formation of the corrosion product nor by the minute change of the interface.

Conversely, the second kinetic constant k_2 (Figure 5.22b) varies whatever the representation, whereas b_2 remains constant. Thus, the second step (dissolution rate of Mg, from adsorbed species, Mg^{+}_{ads}, to Mg^{2+}) is governed by the immersion time. These kinetic parameters allowed the steady-state current to be calculated, using Eq. (5.7), which corresponds, in this case, to the corrosion current density. After 2 h of immersion, the value is about 115 $\mu A.cm^{-2}$, which is in agreement with the current densities measured on the current/potential curve (Figure 5.10). This value is close to that obtained in similar conditions (commercially pure Mg in Na_2SO_4 solution with a RDE) [183].

It can be concluded that the impedance measurements which allowed the evaluation of the corrosion rate from the charge transfer resistance, showed that the variation of the active surface area of the Mg electrode is mainly responsible for the apparent decrease of the corrosion rate as a function of time.

6. CONCLUSIONS

6.1. General conclusions

The overall objective of this work was to evaluate the effect of friction stir welding on the similar joining of aluminum alloy 2524-T3 and the influence of this welding process on the corrosion mechanisms of the alloy. In a second part, a detailed investigation of the corrosion mechanisms of pure magnesium was also performed.

Characterization techniques such as microstructural, electrochemical and corrosion tests allowed a better understanding of the effect of FSW in AA2524 alloy welding. It was possible to observe that due to microstructural modification introduced by FSW, each of the resulting zones, namely: base metal (BM), stir zone (SZ), heat affected zone (HAZ) and thermomechanically affected zone (TMAZ) on both sides (retreating and advancing); presented different behavior towards the corrosive process, including the formation of galvanic coupling between some of these zones. It was shown by all characterization techniques used that the contact region between the HAZ and TMAZ of the retreating side is the most susceptible to the corrosion process, i.e., more active anodically.

In relation to the study of the corrosion mechanism of pure magnesium, which relied on the use of electrochemical techniques, mathematical models, and computer simulation, it was possible to advance in the understanding of both its corrosive process and physical behavior. Moreover, it was also possible to extract several information about the evolution of the corrosion process. For instance, it was possible to determine the evolution with time of several parameters, such as total thickness of the corrosion products formed on the surface of pure Mg, the evolution of the active surface area and the variation of the time constants described in the corrosion mechanism.

6.2. Specific conclusions

- The influence of FSW on the microstructure, corrosion and electrochemical behavior of the 2524-T3 aluminum alloy was observed.
- Results from the agar-agar gel visualization test, open circuit potential measurements and impedance tests showed that the retreating side of the welding joint, in particular the TMAZ/HAZ, was the region most active electrochemically in relation to all other zones.

- Results from the intergranular corrosion test showed galvanic coupling between the base metal (BM) and the welded affected zones with the BM acting as cathode, being cathodically protected by the welded affected zone.
- A model was proposed to fully describe the three-time constants observed in the pure magnesium impedance diagrams as a function of immersion time in a sodium sulfate solution. The Mg dissolution was described by an elementary mechanism involving the exchange of two electrons in two steps and including an adsorbed intermediate (Mg^{+}_{ads}). The Mg^{+}_{ads} is involved in a chemical reaction to describe the NDE. All the impedance diagrams were correctly adjusted with the model.
- First, the increase of the impedance magnitude with time was ascribed to the decrease of the active surface area. In the high-frequency range, the charge transfer resistance in parallel with the interfacial capacitance, allowed a good description of the thin oxide MgO film formed on the Mg surface. Its thickness was obtained from the analysis of the complex capacitance plot, whereas the CPE behavior was explained and analysed by using the power-law model that describes the resistivity variations inside the film [178], [179].
- Second, the second time constant was attributed to the diffusion of electroactive species inside the thick-layer of corrosion products ($Mg(OH)_2$), as previously described in the literature [53].
- Finally, the inductive loop in the low-frequency domain was ascribed to the relaxation of the adsorbate on the Mg surface. It was shown that its magnitude increased with the anodic overpotentials, showing that the adsorbed intermediates can be specific sites on which the NDE occurs.

7. FUTURE WORKS

In the case of aluminum AA2524-T3, it would be of great interest to perform local analysis in the different zones resulting from the FSW-welding process by means of local electrochemical impedance spectroscopy (LEIS), scanning electrochemical microscopy (SECM), and scanning vibrating electrode (SVET). These technique should improve the characterization of the corrosion / degradation processes at different scales, down to the micrometer resolution.

In addition, to analyze the distribution of the nanometer hardening S' phase (Al_2CuMg) in the different welding zones can contribute to a better understanding of its concentration effect on microhardness and corrosion process.

Moreover, to perform differential scanning calorimetry (DSC) analysis can improve the understanding of dissolution, solubilization, and precipitation of the different phases existent along the weld zones.

For pure magnesium, it would be interesting to perform local analysis as LEIS and SECM, which can contribute to a better understanding of the active area evolution as a function of time. Also, provide specific information that can only be accessed by local techniques as the current/potential distribution over the sample surface.

8. REFERENCES

[1] W. A. Monteiro, “Light Metal Alloys Applications,” *Light Met. Alloy. Appl.*, Jun. 2014, doi: 10.5772/57069.

[2] ASM Metals Handbook, *Properties and selection: nonferrous alloys and special*, vol. 2. Ohio, 1990.

[3] R. Grilli, M. A. Baker, J. E. Castle, B. Dunn, and J. F. Watts, “Localized corrosion of a 2219 aluminium alloy exposed to a 3.5% NaCl solution,” *Corros. Sci.*, vol. 52, no. 9, pp. 2855-2866, Sep. 2010, doi: 10.1016/J.CORSCI.2010.04.035.

[4] M. Metikoš-Huković, R. Babić, Z. Grubač, and S. Brinć, “Impedance spectroscopic study of aluminium and Al-alloys in acid solution: inhibitory action of nitrogen containing compounds,” *J. Appl. Electrochem.*, vol. 24, no. 8, pp. 772-778, 1994.

[5] M. Garcia-Rubo *et al.*, “Influence of molybdate species on the tartaric acid/sulphuric acid anodic films grown on AA2024 T3 aerospace alloy,” *Influ. molybdate species tartaric acid/sulphuric acid anodic Film. grown AA2024 T3 Aerosp. Alloy*, vol. 51, no. 9, pp. 2034-2042, 2009, doi: 10.1016/J.CORSCI.2009.05.034.

[6] J. Staley, D. Lege, J. T. Staley, and D. J. Lege, “Advances in aluminium alloy products for structural applications in transportation,” *J. Phys. IV Proc.*, vol. 111, pp. 179-190, 1993, doi: 10.1051/jp4:1993728ï.

[7] S. C. Wang and M. J. Starink, “Two types of S phase precipitates in Al-Cu-Mg alloys,” *Acta Mater.*, vol. 55, no. 3, pp. 933-941, Feb. 2007, doi: 10.1016/J.ACTAMAT.2006.09.015.

[8] R. L. Cervantes, L. E. Murr, and R. M. Arrowood, “Copper nucleation and growth during the corrosion of aluminum alloy 2524 in sodium chloride solutions,” *J. Mater. Sci. 2001 3617*, vol. 36, no. 17, pp. 4079-4088, Sep. 2001, doi: 10.1023/A:1017975728838.

[9] Y. Q. Chen, S. P. Pan, M. Z. Zhou, D. Q. Yi, D. Z. Xu, and Y. F. Xu, “Effects of inclusions, grain boundaries and grain orientations on the fatigue crack initiation and propagation behavior of 2524-T3 Al alloy,” vol. 580, pp. 150-158, Sep. 2013.

[10] W. M. . THOMAS, E. D. . NICHOLAS, J. C. . NEEDHA, M. G. . MURCH, P. . TEMPLE-SMITH, and C. J. DAWES, “Friction stir butt welding,” PCT/GB92/02203, 1991.

[11] R. Nandan, T. DebRoy, and H. K. D. H. Bhadeshia, “Recent advances in friction-stir welding - Process, weldment structure and properties,” *Prog. Mater. Sci.*, pp. 980-1023, 2008, doi: doi:10.1016/j.pmatsci.2008.05.001.

[12] C. A. W. OLEA, “Influence of energy input in fiction stir welding on structure evolution and mechanical behaviour of precipitation-hardening in aluminium alloys (2024-T351, 6013-T6 and Al-Mg-Sc),” Helmholt - Gemeinschaft / Institute of Materials Research, 2008.

[13] T. T. Magazine, “A flying success story for friction stir welding,” *The TWI Magazine*, p. 1, 2003.

[14] P. L. Threadgill, A. J. Leonard, H. R. Shercliff, and P. J. Withers, “Friction stir welding of aluminium alloys,” *Int. Mater. Rev.*, vol. 54, no. 2, pp. 49-93, 2013, doi: 10.1179/174328009X411136.

[15] G. Song, A. Atrens, D. Stjohn, J. Nairn, and Y. Li, “The electrochemical corrosion of pure

magnesium in 1 N NaCl," *Corros. Sci.*, vol. 39, no. 5, pp. 855–875, 1997, doi: 10.1016/S0010-938X(96)00172-2.

[16] G. Song and A. Atrens, "Recent insights into the mechanism of magnesium corrosion and research suggestions," *Adv. Eng. Mater.*, vol. 9, no. 3, pp. 177–183, 2007, doi: 10.1002/adem.200600221.

[17] D. Orlov, V. Joshi, K. N. Solanki, and N. R. Neelameggham, *Magnesium technology*. Springer, New York, 2018.

[18] A. Atrens, G.-L. Song, M. Liu, Z. Shi, F. Cao, and M. S. Dargusch, "Review of recent developments in the field of magnesium corrosion," *Adv. Eng. Mater.*, vol. 17, no. 4, pp. 400–453, 2015, doi: 10.1002/adem.201400434.

[19] G. L. Song and Z. Shi, *Anodization and corrosion of magnesium (Mg) alloys*. Woodhead, 2013.

[20] S. Leleu, B. Rives, J. Bour, N. Causse, and N. Pébère, "On the stability of the oxides film formed on a magnesium alloy containing rare-earth elements," *Electrochim. Acta*, vol. 290, pp. 586–594, 2018, doi: 10.1016/j.electacta.2018.08.093.

[21] S. A. Salman and M. Okido, *Anodization of magnesium (Mg) alloys to improve corrosion resistance*. Woodhead, 2013.

[22] G. L. Makar and J. Kruger, "Corrosion of magnesium," *Int. Mater. Rev.*, vol. 38, no. 3, pp. 138–153, 1993, doi: 10.1179/imr.1993.38.3.138.

[23] G. L. Song and A. Atrens, "Corrosion mechanisms of magnesium alloys," *Adv. Eng. Mater.*, vol. 1, pp. 11–33, 1999, doi: 1https://doi.org/10.1002/(SICI)1527-2648(199909)1:1<11::AID-ADEM11>3.0.CO;2-N.

[24] G. Song and A. Atrens, "Understanding magnesium corrosion. A framework for improved alloy performance," *Adv. Eng. Mater.*, vol. 5, no. 12, pp. 837–858, 2003, doi: 10.1002/adem.200310405.

[25] S. Thomas, N. V. Medhekar, G. S. Frankel, and N. Birbilis, "Corrosion mechanism and hydrogen evolution on Mg," *Curr. Opin. Solid State Mater. Sci.*, vol. 19, no. 2, pp. 85–94, 2015.

[26] M. Esmaily *et al.*, "Fundamentals and advances in magnesium alloy corrosion," *Prog. Mater. Sci.*, vol. 89, pp. 92–193, 2017, doi: 10.1016/j.pmatsci.2017.04.011.

[27] G. S. Frankel, S. Fajardo, and B. M. Lynch, "Introductory lecture on corrosion chemistry: a focus on anodic hydrogen evolution on Al and Mg," *Faraday Discuss.*, vol. 180, pp. 11–33, 2015, doi: 10.1039/c5fd00066a.

[28] G. S. Frankel, A. Samaniego, and N. Birbilis, "Evolution of hydrogen at dissolving magnesium surfaces," *Corros. Sci.*, vol. 70, pp. 104–111, 2013, doi: 10.1016/j.corsci.2013.01.017.

[29] S. Fajardo and G. S. Frankel, "A kinetic model explaining the enhanced rates of hydrogen evolution on anodically polarized magnesium in aqueous environments," *Electrochem. commun.*, vol. 84, pp. 36–39, 2017, doi: 10.1016/j.elecom.2017.10.001.

[30] G. Williams, N. Birbilis, and H. N. Mcmurray, "The source of hydrogen evolved from a magnesium anode," *Electrochem. commun.*, vol. 36, pp. 1–5, 2013, doi: 10.1016/j.elecom.2013.08.023.

[31] S. Fajardo and G. S. Frankel, “Gravimetric method for hydrogen evolution measurements on dissolving magnesium,” *J. Electrochem. Soc.*, vol. 162, no. 14, pp. C693–C701, 2015, doi: 10.1149/2.0241514jes.

[32] J. Światowska, P. Volovitch, and K. Ogle, “The anodic dissolution of Mg in NaCl and Na2SO4 electrolytes by atomic emission spectroelectrochemistry,” *Corros. Sci.*, vol. 52, no. 7, pp. 2372–2378, 2010, doi: 10.1016/j.corsci.2010.02.038.

[33] V. Shkirskiy *et al.*, “Revisiting the electrochemical impedance spectroscopy of magnesium with online inductively coupled plasma atomic emission spectroscopy,” *ChemPhysChem*, vol. 16, no. 3, pp. 536–539, 2015, doi: 10.1002/cphc.201402666.

[34] J. A. Yuwono, N. Birbilis, R. Liu, Q. Ou, Q. Bao, and N. V. Medhekar, “Aqueous electrochemical activity of the Mg surface: the role of group 14 and 15 microalloying elements,” *J. Electrochem. Soc.*, vol. 164, no. 13, pp. C918–C929, 2017, doi: 10.1149/2.0071714jes.

[35] S. Fajardo, O. Gharbi, N. Birbilis, and G. S. Frankel, “Investigating the effect of ferrous ions on the anomalous hydrogen evolution on magnesium in acidic ferrous chloride solution,” *J. Electrochem. Soc.*, vol. 165, no. 13, pp. C916–C925, 2018, doi: 10.1149/2.0951813jes.

[36] O. Gharbi and N. Birbilis, “Clarifying the dissolution mechanisms and electrochemistry of Mg2Si as a function of solution pH,” *J. Electrochem. Soc.*, vol. 165, no. 9, pp. C497–C501, 2018, doi: 10.1149/2.1061809jes.

[37] S. Fajardo and G. S. Frankel, “Effect of impurities on the enhanced catalytic activity for hydrogen evolution in high purity magnesium,” *Electrochim. Acta*, vol. 165, pp. 255–267, 2015, doi: 10.1016/j.electacta.2015.03.021.

[38] A. Samaniego, N. Birbilis, X. Xia, and G. S. Frankel, “Hydrogen evolution during anodic polarization of Mg alloyed with Li, Ca, or Fe,” *Corrosion*, vol. 71, no. 2, pp. 224–233, 2015, doi: 10.5006/1367.

[39] S. Fajardo, J. Bosch, and G. S. Frankel, “Anomalous hydrogen evolution on AZ31, AZ61 and AZ91 magnesium alloys in unbuffered sodium chloride solution,” *Corros. Sci.*, vol. 146, pp. 163–171, 2019, doi: 10.1016/j.corsci.2018.10.039.

[40] J. L. Robinson and P. F. King, “Electrochemical behavior of the magnesium anode,” *J. Electrochem. Soc.*, vol. 108, no. 1, pp. 36–41, 1961, doi: 10.1149/1.2428007.

[41] G. G. Perrault, “Potentiostatic study of the magnesium electrode in aqueous solution,” *J. Electroanal. Chem.*, vol. 27, no. 1, pp. 47–58, 1970, doi: 10.1016/S0022-0728(70)80201-7.

[42] E. Gulbrandsen, J. Taftø, and A. Olsen, “The passive behaviour of Mg in alkaline fluoride solutions. Electrochemical and electron microscopical investigations,” *Corros. Sci.*, vol. 34, no. 9, pp. 1423–1440, 1993, doi: 10.1016/0010-938X(93)90238-C.

[43] Z. Shi, J. X. Jia, and A. Atrens, “Galvanostatic anodic polarisation curves and galvanic corrosion of high purity Mg in 3.5% NaCl saturated with $Mg(OH)_2$,” *Corros. Sci.*, vol. 60, pp. 296–308, 2012, doi: 10.1016/j.corsci.2011.12.002.

[44] Z. Shi, F. Cao, G. L. Song, and A. Atrens, “Low apparent valence of Mg during corrosion,” *Corros. Sci.*, vol. 88, pp. 434–443, 2014, doi: 10.1016/j.corsci.2014.07.060.

[45] A. D. Atrens, I. Gentle, and A. Atrens, “Possible dissolution pathways participating in the Mg corrosion reaction,” *Corros. Sci.*, vol. 92, pp. 173–181, 2015, doi: 10.1016/j.corsci.2014.12.004.

[46] H. B. Yao, Y. Li, and A. T. S. Wee, “XPS investigation of the oxidation/corrosion of melt-spun Mg,” *Appl. Surf. Sci.*, vol. 158, no. 1–2, pp. 112–119, 2000, doi: 10.1016/S0169-4332(99)00593-0.

[47] M. Santamaria, F. Di Quarto, S. Zanna, and P. Marcus, “Initial surface film on magnesium metal: A characterization by X-ray photoelectron spectroscopy (XPS) and photocurrent spectroscopy (PCS),” *Electrochim. Acta*, vol. 53, pp. 1314–1324, 2007, doi: 10.1016/j.electacta.2007.03.019.

[48] A. Seyeux, M. Liu, P. Schmutz, G. Song, A. Atrens, and P. Marcus, “ToF-SIMS depth profile of the surface film on pure magnesium formed by immersion in pure water and the identification of magnesium hydride,” *Corros. Sci.*, vol. 51, no. 9, pp. 1883–1886, 2009, doi: 10.1016/j.corsci.2009.06.002.

[49] D. Mercier, J. Światowska, S. Zanna, A. Seyeux, and P. Marcus, “Role of segregated iron at grain boundaries on Mg corrosion,” *J. Electrochem. Soc.*, vol. 165, no. 2, pp. C42–C49, 2018, doi: 10.1149/2.0621802jes.

[50] N. Pebere, C. Riera, and F. Dabosi, “Investigation of magnesium corrosion in aerated sodium sulfate solution by electrochemical impedance spectroscopy,” *Electrochim. Acta*, vol. 35, pp. 555–561, 1990, doi: 10.1016/0013-4686(90)87043-2.

[51] G. Baril and N. Pébère, “Corrosion of pure magnesium in aerated and deaerated sodium sulphate solutions,” *Corros. Sci.*, vol. 43, no. 3, pp. 471–484, 2001, doi: 10.1016/S0010-938X(00)00095-0.

[52] G. Baril, C. Blanc, M. Keddam, and N. Pébère, “Local electrochemical impedance spectroscopy applied to the corrosion behavior of an AZ91 magnesium alloy,” *J. Electrochem. Soc.*, vol. 150, no. 10, pp. B488–B493, 2003, doi: 10.1149/1.1602080.

[53] G. Baril, G. Galicia, C. Deslouis, N. Pébère, B. Tribollet, and V. Vivier, “An impedance investigation of the mechanism of pure magnesium corrosion in sodium sulfate solutions,” *J. Electrochem. Soc.*, vol. 154, no. 2, pp. C108–C113, 2007, doi: 10.1149/1.2401056.

[54] A. D. King, N. Birbilis, and J. R. Scully, “Accurate electrochemical measurement of magnesium corrosion rates; A combined impedance, mass-loss and hydrogen collection study,” *Electrochim. Acta*, vol. 121, pp. 394–406, 2014, doi: 10.1016/j.electacta.2013.12.124.

[55] M. Curioni, L. Salamone, F. Scenini, M. Santamaria, and M. Di Natale, “A mathematical description accounting for the superfluous hydrogen evolution and the inductive behaviour observed during electrochemical measurements on magnesium,” *Electrochim. Acta*, vol. 274, pp. 343–352, 2018, doi: 10.1016/j.electacta.2018.04.116.

[56] M. Orazem and B. Tribollet, *Electrochemical impedance spectroscopy*, 2nd ed. New Jersey: John Wiley & Sons, Inc., 2017.

[57] M. Benoit *et al.*, “Comparison of different methods for measuring the passive film thickness on metals,” *Electrochim. Acta*, vol. 201, no. 2015, pp. 340–347, 2016, doi: 10.1016/j.electacta.2015.12.173.

[58] T. T. M. Tran, B. Tribollet, and E. M. M. Sutter, “New insights into the cathodic dissolution

of aluminium using electrochemical methods," *Electrochim. Acta*, vol. 216, pp. 58–67, 2016, doi: 10.1016/j.electacta.2016.09.011.

[59] S. Chakri *et al.*, "Improved EIS analysis of the electrochemical behaviour of carbon steel in alkaline solution," *Electrochim. Acta*, vol. 246, pp. 924–930, 2017, doi: 10.1016/j.electacta.2017.06.096.

[60] S. Chakri *et al.*, "Imaging of a thin oxide film formation from the combination of surface reflectivity and electrochemical methods," *Anal. Chem.*, vol. 89, pp. 5303–5310, 2017, doi: 10.1021/acs.analchem.6b04921.

[61] J. R. DAVIS, "Alloying: understanding the basics," in *Aluminum and aluminum alloys*, ASM International, 2001, pp. 351–416.

[62] W. D. Callister, *Materials science and engineering: an introduction*. LTC, 2006.

[63] C. VARGEL, *Corrosion of aluminium*. Elsevier Amsterdam, 2004.

[64] J. DWIGHT, *Aluminium design and construction*. Routledge, 1999.

[65] A. B. D. A. (ABAL), *Fundamentos e aplicações do alumínio*. Editora ABAL, 2007.

[66] Z. Q. Zheng, B. Cai, T. Zhai, and S. C. Li, "The behavior of fatigue crack initiation and propagation in AA2524-T34 alloy," *Mater. Sci. Eng. A*, vol. 528, no. 4–5, pp. 2017–2022, Feb. 2011, doi: 10.1016/j.msea.2010.10.085.

[67] F. Shen, B. Wang, D. Yi, H. Liu, C. Tang, and W. Shou, "Effects of heating rate during solid-solution treatment on microstructure and fatigue properties of AA2524 T3 Al-Cu-Mg sheet," *Mater. Des.*, vol. 104, pp. 116–125, Aug. 2016, doi: 10.1016/j.matdes.2016.05.002.

[68] S. C. Wang and M. J. Starink, "Two types of S phase precipitates in Al-Cu-Mg alloys," *Acta Mater.*, vol. 55, pp. 933–941, 2007, doi: doi.org/10.1016/j.actamat.2006.09.015.

[69] S. N. Grieshop and R. G. Buchheit, "Comparison of the Corrosion Behavior of High Strength Aluminum Alloys after Exposure to ASTM B117 Environment," 2014. Accessed: Feb. 17, 2021. [Online]. Available: https://kb.osu.edu/handle/1811/60362.

[70] Y. L. Yang, L. H. Zhan, and J. Li, "Constitutive modeling and springback simulation for 2524 aluminum alloy in creep age forming," *Trans. Nonferrous Met. Soc. China (English Ed.*, vol. 25, no. 9, pp. 3048–3055, Sep. 2015, doi: 10.1016/S1003-6326(15)63932-2.

[71] E. A. DeBartolo and B. M. Hillberry, "A model of initial flaw sizes in aluminum alloys," *Int. J. Fatigue*, vol. 23, no. SUPPL. 1, pp. 79–86, Jan. 2001, doi: 10.1016/s0142-1123(01)00122-0.

[72] T. S. Srivatsan, D. Kolar, and P. Magnusen, "The cyclic fatigue and final fracture behavior of aluminum alloy 2524," *Mater. Des.*, vol. 23, no. 2, pp. 129–139, Apr. 2002, doi: 10.1016/S0261-3069(01)00070-X.

[73] T. aluminum Association, "International Alloy Designations and Chemical Composition Limits for Wrought Aluminum and Wrought Aluminum Alloys," 2018. Accessed: Feb. 05, 2021. [Online]. Available: www.aluminum.org/tealsheets.

[74] A. Barbucci, P. L. Cabot, G. Bruzzone, and G. Cerisola, "Role of intermetallics in the activation of Al-Mg-Zn alloys," *J. Alloys Compd.*, vol. 268, no. 1–2, pp. 295–301, Mar. 1998, doi: 10.1016/S0925-8388(97)00605-1.

[75] F. M. Queiroz, M. Magnani, I. Costa, and H. G. de Melo, “Investigation of the corrosion behaviour of AA 2024-T3 in low concentrated chloride media,” *Corros. Sci.*, vol. 50, no. 9, pp. 2646–2657, Sep. 2008, doi: 10.1016/j.corsci.2008.06.041.

[76] F. C. Campbell, *Aluminum*. Elsevier Science, 2006.

[77] J. R. Kissell, S. G. Pantelakis, and G. N. Haidemenopoulos, *Aluminum and Aluminum Alloys*. John Wiley & Sons, Ltd, 2004.

[78] J. L. Trompette, L. Arurault, S. Fontorbes, and L. Massot, “Influence of the anion specificity on the electrochemical corrosion of anodized aluminum substrates,” *Electrochim. Acta*, vol. 55, no. 8, pp. 2901–2910, Mar. 2010, doi: 10.1016/J.ELECTACTA.2009.12.063.

[79] K. Shimizu, R. C. Furneaux, G. E. Thompson, G. C. Wood, A. Gotoh, and K. Kobayashi, “On the nature of ‘easy paths’ for the diffusion of oxygen in thermal oxide films on aluminum,” *Oxid. Met. 1991 355*, vol. 35, no. 5, pp. 427–439, Jun. 1991, doi: 10.1007/BF00664713.

[80] M. Pourbaix, *Atlas of electrochemical equilibria in aqueous solutions*, 2nd ed., vol. 1, no. 2. Brussels: National Association of Corrosion Engineers, 1974.

[81] S. Wolynec, *Técnicas Eletroquímicas em Corrosão*. Edusp, 2013.

[82] S. Xu and Y. Wang, “Estimating the effects of corrosion pits on the fatigue life of steel plate based on the 3D profile,” *Int. J. Fatigue*, vol. Complete, no. 72, pp. 27–41, 2015, doi: 10.1016/J.IJFATIGUE.2014.11.003.

[83] L. V. Ramanathan, *Corrosão e Seu Controle*. São Paulo: Hemus, 1996.

[84] R. L. Twite and G. P. Bierwagen, “Review of alternatives to chromate for corrosion protection of aluminum aerospace alloys,” *Prog. Org. Coatings*, vol. 33, no. 2, pp. 91–100, Feb. 1998, doi: 10.1016/S0300-9440(98)00015-0.

[85] E. Bousquet, “Durabilité des assemblages soudés stir welding (FSW) : corrélation entre microstructure et sensibilité à la corrosion,” Bordeaux 1, Bordeaux, 2011.

[86] X. Zhou, C. Luo, T. Hashimoto, A. E. Hughes, and G. E. Thompson, “Study of localized corrosion in AA2024 aluminium alloy using electron tomography,” *Corros. Sci.*, vol. 58, pp. 299–306, May 2012, doi: 10.1016/J.CORSCI.2012.02.001.

[87] A. E. Hughes *et al.*, “Corrosion of AA2024-T3 Part II: Co-operative corrosion,” *Corros. Sci.*, vol. 53, no. 1, pp. 27–39, Jan. 2011, doi: 10.1016/J.CORSCI.2010.09.030.

[88] N. Birbilis and R. G. Buchheit, “Electrochemical Characteristics of Intermetallic Phases in Aluminum Alloys: An Experimental Survey and Discussion,” *J. Electrochem. Soc.*, vol. 152, no. 4, pp. B140–B151, Mar. 2005, doi: 10.1149/1.1869984.

[89] R. G. Buchheit, R. P. Grant, P. F. Hlava, B. Mckenzie, and G. L. Zender, “Local Dissolution Phenomena Associated with S Phase (Al_2CuMg) Particles in Aluminum Alloy 2024- T3,” *J. Electrochem. Soc.*, vol. 144, no. 8, pp. 2621–2628, 1997, doi: 10.1149/1.1837874.

[90] A. Boag, A. E. Hughes, A. M. Glenn, T. H. Muster, and D. McCulloch, “Corrosion of AA2024-T3 Part I: Localised corrosion of isolated IM particles,” *Corros. Sci.*, vol. 53, no. 1, pp. 17–26, Jan. 2011, doi: 10.1016/J.CORSCI.2010.09.009.

[91] Z. Szklarska-Smialowska, “Pitting corrosion of aluminum,” *Corros. Sci.*, vol. 41, no. 9, pp. 1743–1767, Aug. 1999, doi: 10.1016/S0010-938X(99)00012-8.

[92] Z. Szklarska-Smialowska, “Insight into the pitting corrosion behavior of aluminum alloys,” *Corros. Sci.*, vol. 33, no. 8, pp. 1193–1202, Aug. 1992, doi: 10.1016/0010-938X(92)90130-U.

[93] E. McCafferty, “Sequence of steps in the pitting of aluminum by chloride ions,” *Corros. Sci.*, vol. 45, no. 7, pp. 1421–1438, Jul. 2003, doi: 10.1016/S0010-938X(02)00231-7.

[94] M. X. Milagre *et al.*, “Comparison of the corrosion resistance of an Al–Cu alloy and an Al–Cu–Li alloy,” *https://doi.org/10.1080/1478422X.2019.1605472*, vol. 54, no. 5, pp. 402–412, Jul. 2019, doi: 10.1080/1478422X.2019.1605472.

[95] C. Luo *et al.*, “Continuous and discontinuous localized corrosion of a 2xxx aluminium–copper–lithium alloy in sodium chloride solution,” *J. Alloys Compd.*, vol. 658, pp. 61–70, Feb. 2016, doi: 10.1016/J.JALLCOM.2015.10.185.

[96] M. Dhondt, I. Aubert, N. Saintier, and J. M. Olive, “Effects of microstructure and local mechanical fields on intergranular stress corrosion cracking of a friction stir welded aluminum–copper–lithium 2050 nugget,” *Corros. Sci.*, vol. 86, pp. 123–130, Sep. 2014, doi: 10.1016/J.CORSCI.2014.05.001.

[97] X. Zhang *et al.*, “Corrosion Behavior of Friction Stir Welded 2A97 Al-Cu-Li alloy,” *Corrosion*, vol. 73, no. 8, pp. 988–997, Aug. 2017, doi: 10.5006/2418.

[98] A. Astarita, C. Bitondo, A. Squillace, E. Armentani, and F. Bellucci, “Stress corrosion cracking behaviour of conventional and innovative aluminium alloys for aeronautic applications,” *Surf. Interface Anal.*, vol. 45, no. 10, pp. 1610–1618, Oct. 2013, doi: 10.1002/SIA.5234.

[99] J. Corral, E. Trillo, Y. Li, and L. Murr, “Corrosion of friction-stir welded aluminum alloys 2024 and 2195,” *J. Mater. Sci. Lett.*, vol. 19, no. 23, pp. 2117–2122, Oct. 2004, doi: 10.1023/A:1026710422951.

[100] E. G. Cole, A. Fehrenbacher, N. A. Duffie, M. R. Zinn, F. E. Pfefferkorn, and N. J. Ferrier, “Weld temperature effects during friction stir welding of dissimilar aluminum alloys 6061-T6 and 7075-T6,” *Adv. Manuf. Technol.*, vol. 71, pp. 643–652, 2014, doi: 10.1007/s00170-013-5485-9.

[101] Y. G. Kim, H. Fujii, T. Tsumura, T. Komazaki, and K. Nakata, “Three defect types in friction stir welding of aluminum die casting alloy,” *Mater. Sci. Eng. A*, vol. 415, no. 1–2, pp. 250–254, Jan. 2006, doi: 10.1016/j.msea.2005.09.072.

[102] F. J. HUMPHREYS and M. HATHERLY, *Recrystallization and Related Annealing Phenomena - 1st Edition*. Oxford: Pergamon Press, 1995.

[103] E. Bousquet, A. Poulon-Quintin, M. Puiggali, O. Devos, and M. Touzet, “Relationship between microstructure, microhardness and corrosion sensitivity of an AA 2024-T3 friction stir welded joint,” *Corros. Sci.*, vol. 53, no. 9, pp. 3026–3034, Sep. 2011, doi: 10.1016/j.corsci.2011.05.049.

[104] R. W. Fonda, P. S. Pao, H. N. Jones, C. R. Feng, B. J. Connolly, and A. J. Davenport, “Microstructure, mechanical properties, and corrosion of friction stir welded Al 5456,” *Mater. Sci. Eng. A*, vol. 519, pp. 1–8, Aug. 2009, doi: 10.1016/j.msea.2009.04.034.

[105] W. Hu and E. I. Meletis, “Corrosion and environment-assisted cracking behavior of friction stir welded Al 2195 and Al 2219 alloys,” *Mater. Sci. Forum*, vol. 331, pp. 1683–1688, 2000, doi: 10.4028/www.scientific.net/msf.331-337.1683.

[106] M. Jariyaboon, A. J. Davenport, R. Ambat, B. J. Connolly, S. W. Williams, and D. A. Price, “The effect of cryogenic CO_2 cooling on corrosion behaviour of friction stir welded AA2024-T351,” *Corros. Eng. Sci. Technol.*, vol. 44, no. 6, pp. 425–432, Dec. 2013, doi: 10.1179/147842208X373173.

[107] Y. Xu, X. Wang, Z. Yan, and J. Li, “Corrosion Properties of Light-weight and High-strength 2195 Al-Li Alloy,” *Chinese J. Aeronaut.*, vol. 24, no. 5, pp. 681–686, Oct. 2011, doi: 10.1016/S1000-9361(11)60080-0.

[108] V. Proton *et al.*, “Influence of Post-Welding Heat Treatment on the Corrosion Behavior of a 2050-T3 Aluminum-Copper-Lithium Alloy Friction Stir Welding Joint,” *J. Electrochem. Soc.*, vol. 158, no. 5, pp. C139–C148, Mar. 2011, doi: 10.1149/1.3562206.

[109] J. Q. Su, T. W. Nelson, R. Mishra, and M. Mahoney, “Microstructural investigation of friction stir welded 7050-T651 aluminium,” *Acta Mater.*, vol. 51, no. 3, pp. 713–729, Feb. 2003, doi: 10.1016/S1359-6454(02)00449-4.

[110] B. Heinz and B. Skrotzki, “Characterization of a friction-stir-welded aluminum alloy 6013,” *Metall. Mater. Trans. B 2002 333*, vol. 33, no. 3, pp. 489–498, 2002, doi: 10.1007/S11663-002-0059-5.

[111] V. Proton, J. Alexis, E. Andrieu, J. Delfosse, M. C. Lafont, and C. Blanc, “Characterisation and understanding of the corrosion behaviour of the nugget in a 2050 aluminium alloy Friction Stir Welding joint,” *Corros. Sci.*, vol. 73, pp. 130–142, Aug. 2013, doi: 10.1016/J.CORSCI.2013.04.001.

[112] V. Fahimpour, S. K. Sadrnezhaad, and F. Karimzadeh, “Corrosion behavior of aluminum 6061 alloy joined by friction stir welding and gas tungsten arc welding methods,” *Mater. Des.*, vol. 39, pp. 329–333, Aug. 2012, doi: 10.1016/J.MATDES.2012.02.043.

[113] ASTM, “Standard Practice for Evaluating Intergranular Corrosion Resistance of Heat Treatable Aluminum Alloys by Immersion in Sodium Chloride + Hydrogen Peroxide Solution 1.” pp. 92–94, 2003.

[114] A. Squillace, A. De Fenzo, G. Giorleo, and F. Bellucci, “A comparison between FSW and TIG welding techniques: modifications of microstructure and pitting corrosion resistance in AA 2024-T3 butt joints,” *J. Mater. Process. Technol.*, vol. 152, no. 1, pp. 97–105, Oct. 2004, doi: 10.1016/J.JMATPROTEC.2004.03.022.

[115] M. Jariyaboon, A. J. Davenport, R. Ambat, B. J. Connolly, S. W. Williams, and D. A. Price, “The effect of welding parameters on the corrosion behaviour of friction stir welded AA2024-T351,” *Corros. Sci.*, vol. 49, no. 2, pp. 877–909, Feb. 2007, doi: 10.1016/j.corsci.2006.05.038.

[116] J. A. BOYER, “The corrosion of magnesium and of the magnesium aluminum alloys containing manganese,” *NACA Tech. Reports*, pp. 1–41, 1927, doi: 10.15713/ins.mmj.3.

[117] R. Tunold, H. Holtan, M. B. H. Berge, A. Lasson, and R. Steen-Hansen, “The corrosion of magnesium in aqueous solution containing chloride ions,” *Corros. Sci.*, vol. 17, no. 4, pp. 353–365, 1977, doi: 10.1016/0010-938X(77)90059-2.

[118] G. Song, D. S. T. John, and J. Nairn, “The anodic dissolution of magnesium in chloride

and sulphate solutions," *Corros. Sci.*, vol. 39, no. 10–11, pp. 1981–2004, 1997, doi: http://dx.doi.org/10.1016/S0010-938X(97)00090-5.

[119] A. K. Jonscher, "Dielectric relaxation in solids," *J. Phys. D. Appl. Phys.*, vol. 32, pp. R57–R70, 1999, doi: 10.1088/0022-3727/32/14/201.

[120] P. F. King, "The role of the anion in the anodic dissolution of magnesium," *J. Electrochem. Soc.*, vol. 113, no. 6, pp. 536–539, 1966.

[121] R. L. Petty, A. W. Davidson, and J. Kleinberg, "The Anodic Oxidation of Magnesium Metal: Evidence for the Existence of Unipositive Magnesium," *J. Am. Chem. Soc.*, vol. 76, no. 2, pp. 363–366, 1954, doi: 10.1021/ja01631a013.

[122] A. Samaniego, B. L. Hurley, and G. S. Frankel, "On the evidence for univalent Mg," *J. Electroanal. Chem.*, vol. 737, pp. 123–128, 2014, doi: 10.1016/j.jelechem.2014.04.013.

[123] K. S. Williams, V. Rodriguez-Santiago, and J. W. Andzelm, "Modeling reaction pathways for hydrogen evolution and water dissociation on magnesium," *Electrochim. Acta*, vol. 210, pp. 261–270, 2016, doi: 10.1016/j.electacta.2016.04.128.

[124] J. A. Yuwono, N. Birbilis, K. S. Williams, and N. V. Medhekar, "Electrochemical stability of magnesium surfaces in an aqueous environment," *J. Phys. Chem. C*, vol. 120, no. 47, pp. 26922–26933, 2016, doi: 10.1021/acs.jpcc.6b09232.

[125] G. Williams, N. Birbilis, and H. N. McMurray, "Controlling factors in localised corrosion morphologies observed for magnesium immersed in chloride containing electrolyte," *Faraday Discuss.*, vol. 180, pp. 313–330, 2015, doi: 10.1039/c4fd00268g.

[126] T. Cain, S. B. Madden, N. Birbilis, and J. R. Scully, "Evidence of the enrichment of transition metal elements on corroding magnesium surfaces using rutherford backscattering spectrometry," *J. Electrochem. Soc.*, vol. 162, no. 6, pp. C228–C237, 2015, doi: 10.1149/2.0541506jes.

[127] T. W. Cain, I. Gonzalez-Afanador, N. Birbilis, and J. R. Scully, "The role of surface films and dissolution products on the negative difference effect for magnesium: comparison of Cl^- versus Cl^- free solutions," *J. Electrochem. Soc.*, vol. 164, no. 6, pp. C300–C311, 2017, doi: 10.1149/2.1371706jes.

[128] D. Lysne, S. Thomas, M. F. Hurley, and N. Birbilis, "On the Fe enrichment during anodic polarization of Mg and its impact on hydrogen evolution," *J. Electrochem. Soc.*, vol. 162, no. 8, pp. C396–C402, 2015, doi: 10.1149/2.0251508jes.

[129] S. Fajardo, C. F. Glover, G. Williams, and G. S. Frankel, "The source of anodic hydrogen evolution on ultra high purity magnesium," *Electrochim. Acta*, vol. 212, pp. 510–521, 2016, doi: 10.1016/j.electacta.2016.07.018.

[130] M. Taheri, M. Danaie, and J. R. Kish, "TEM examination of the film formed on corroding Mg prior to breakdown," *J. Electrochem. Soc.*, vol. 161, no. 3, pp. C89–C94, 2014, doi: 10.1149/2.017403jes.

[131] J. H. Nordlien, S. Ono, N. Masuko, and K. Nisancioglu, "A tem investigation of naturally formed oxide films on pure magnesium," *Corros. Sci.*, vol. 39, no. 8, pp. 1397–1414, 1997, doi: 10.1016/S0010-938X(97)00037-1.

[132] M. P. Brady *et al.*, "Film breakdown and nano-porous $Mg(OH)_2$ formation from corrosion of magnesium alloys in salt solutions," *J. Electrochem. Soc.*, vol. 162, no. 4, pp. C140–

C149, 2015, doi: 10.1149/2.0171504jes.

[133] M. Stern, “Electrochemical polarization,” *J. Electrochem. Soc.*, vol. 104, no. 9, pp. 56–63, 1957, doi: 10.1149/1.2428653.

[134] M. Keddam, “2006 W.R. Whitney Award Lecture: Application of Advanced Electrochemical Techniques and Concepts to Corrosion Phenomena,” *Corrosion*, vol. 62, no. 12, pp. 1056–1066, Dec. 2006, doi: 10.5006/1.3278239.

[135] Z. Shi, M. Liu, and A. Atrens, “Measurement of the corrosion rate of magnesium alloys using Tafel extrapolation,” *Corros. Sci.*, vol. 52, no. 2, pp. 579–588, 2010, doi: 10.1016/j.corsci.2009.10.016.

[136] A. Pardo, S. Feliu, M. C. Merino, R. Arrabal, and E. Matykina, “Electrochemical estimation of the corrosion rate of magnesium/aluminium alloys,” *Int. J. Corros.*, vol. 2010, pp. 7–13, 2010, doi: 10.1155/2010/953850.

[137] Z. Qiao, Z. Shi, N. Hort, N. I. Zainal Abidin, and A. Atrens, “Corrosion behaviour of a nominally high purity Mg ingot produced by permanent mould direct chill casting,” *Corros. Sci.*, vol. 61, pp. 185–207, 2012, doi: 10.1016/j.corsci.2012.04.030.

[138] L. G. Bland, A. D. King, N. Birbilis, and J. R. Scully, “Assessing the corrosion of commercially pure magnesium and commercial AZ31B by electrochemical impedance, mass-loss, hydrogen collection, and inductively coupled plasma optical emission spectrometry solution analysis,” *Corrosion*, vol. 71, no. 2, pp. 128–145, 2015, doi: 10.5006/1419.

[139] D. C. Silverman, “Corrosion rate estimation from pseudo-inductive electrochemical impedance response,” *Corrosion*, vol. 45, no. 10, pp. 824–830, 1989, doi: 10.5006/1.3584989.

[140] ASTM, “Standard Test Method for Exfoliation Corrosion Susceptibility in 2xxx and 7xxx Aluminium Alloys.” p. 99, 1974.

[141] C. S. Isaacs, H. S.; Adzic, G.; Jeffcoate, “2000 W.R. Whitney award lecture: Visualizing corrosion,” *Corrosion*, vol. 56, no. 10, pp. 971–978, 2000, doi: 10.5006/1.3294386.

[142] J. R. Macdonald, “Some new directions in impedance spectroscopy data analysis,” *Electrochim. Acta*, vol. 38, no. 14, pp. 1883–1890, 1993, doi: 10.1016/0013-4686(93)80310-V.

[143] C. Gabrielli, M. Keddam, and H. Takenouti, “Kramers-Kronig transformation in relation to the interface regulating device,” *ASTM Spec. Tech. Publ.*, vol. 1188, pp. 140–153, 1993.

[144] R. S. Mishra and Z. Y. Ma, “Friction stir welding and processing,” *Materials Science and Engineering R: Reports*, vol. 50, no. 1–2. Elsevier, pp. 1–78, Aug. 31, 2005, doi: 10.1016/j.mser.2005.07.001.

[145] X. He, F. Gu, and A. Ball, “A review of numerical analysis of friction stir welding,” *Prog. Mater. Sci.*, vol. 65, pp. 1–66, Aug. 2014, doi: 10.1016/j.pmatsci.2014.03.003.

[146] W. Li, R. Jiang, Z. Zhang, and Y. Ma, “Effect of Rotation Speed to Welding Speed Ratio on Microstructure and Mechanical Behavior of Friction Stir Welded Aluminum–Lithium Alloy Joints,” *Adv. Eng. Mater.*, vol. 15, no. 11, pp. 1051–1058, Nov. 2013, doi: 10.1002/ADEM.201300147.

[147] P. Cavaliere, M. Cabibbo, F. Panella, and A. Squillace, “2198 Al–Li plates joined by

Friction Stir Welding: Mechanical and microstructural behavior," *Mater. Des.*, vol. 30, pp. 3622–3631, 2009, doi: 10.1016/J.MATDES.2009.02.021.

[148] X. Y. Liu, M. J. Li, F. Gao, S. X. Liang, X. L. Zhang, and H. X. Cui, "Effects of aging treatment on the intergranular corrosion behavior of Al–Cu–Mg–Ag alloy," *J. Alloys Compd.*, vol. 639, pp. 263–267, 2015, doi: 10.1016/J.JALLCOM.2015.03.174.

[149] R. W. Fonda and J. F. Bingert, "Precipitation and grain refinement in a 2195 Al friction stir weld," *Metall. Mater. Trans. A 2006 3712*, vol. 37, no. 12, pp. 3593–3604, Dec. 2006, doi: 10.1007/S11661-006-1054-2.

[150] F. M. Queiroz *et al.*, "Effect of unequal levels of deformation and fragmentation on the electrochemical response of friction stir welded AA2024-T3 alloy," *Electrochim. Acta*, vol. 313, pp. 271–281, Aug. 2019, doi: 10.1016/j.electacta.2019.04.137.

[151] C. Blanc and G. Mankowski, "Susceptibility to pitting corrosion of 6056 aluminium alloy," *Corros. Sci.*, vol. 39, pp. 949–959, 1997.

[152] C. Blanc, B. Lavelle, and G. Mankowski, "The role of precipitates enriched with copper on the susceptibility to pitting corrosion of the 2024 aluminium alloy," *Corros. Sci.*, vol. 39, pp. 495–510, 1997.

[153] A. J. Bard and L. R. Faulkner, *Electrochemical methods, fundamentals and applications*, 2nd ed., no. 2. John Wiley & Sons, 2001.

[154] A. Boag *et al.*, "Stable pit formation on AA2024-T3 in a NaCl environment," *Corros. Sci.*, vol. 52, no. 1, pp. 90–103, Jan. 2010, doi: 10.1016/J.CORSCI.2009.08.043.

[155] A. Aballe, M. Bethencourt, F. J. Botana, M. J. Cano, and M. Marcos, "Localized alkaline corrosion of alloy AA5083 in neutral 3.5% NaCl solution," *Corros. Sci.*, vol. 43, no. 9, pp. 1657–1674, Sep. 2001, doi: 10.1016/S0010-938X(00)00166-9.

[156] T. Hagyard and J. R. Williams, "Potential of aluminium in aqueous chloride solutions. Part 1," *Trans. Faraday Soc.*, vol. 57, no. 0, pp. 2288–2294, Jan. 1961, doi: 10.1039/TF9615702288.

[157] G. S. Peng, K. H. Chen, H. C. Fang, H. Chao, and S. Y. Chen, "EIS study on pitting corrosion of 7150 aluminum alloy in sodium chloride and hydrochloric acid solution," *Mater. Corros.*, vol. 61, no. 9, pp. 783–789, Sep. 2010, doi: 10.1002/MACO.200905413/FORMAT/PDF.

[158] F. H. Cao, Z. Zhang, J. F. Li, Y. L. Cheng, J. Q. Zhang, and C. N. Cao, "Exfoliation corrosion of aluminum alloy AA7075 examined by electrochemical impedance spectroscopy," *Mater. Corros.*, vol. 55, no. 1, pp. 18–23, 2004, doi: 10.1002/MACO.200303691/FORMAT/PDF.

[159] A. Conde and J. de Damborenea, "Electrochemical modelling of exfoliationcorrosion behaviour of 8090 alloy," *Electrochim. Acta*, vol. 43, no. 8, pp. 849–860, 1998.

[160] T. Valand and K. E. Heusler, "Reactions at the oxide-electrolyte interface of anodic oxide films on aluminum," *J. Electroanal. Chem.*, pp. 71–82, 1983.

[161] I. V. Aoki *et al.*, "Ac-impedance and Raman spectroscopy study of the electrochemical behaviour of pure aluminium in citric acid media," *Electrochim. Acta*, vol. 46, no. 12, pp. 1871–1878, Mar. 2001, doi: 10.1016/S0013-4686(01)00431-5.

[162] J. B. Bessone, D. R. Salinas, C. E. Mayer, M. Ebert, and W. J. Lorenz, "An EIS study of

aluminium barrier-type oxide films formed in different media," *Electrochim. Acta*, vol. 37, no. 12, pp. 2283–2290, 1992, doi: 10.1016/0013-4686(92)85124-4.

[163] J. A. Moreto *et al.*, "On the global and localised corrosion behaviour of the AA2524-T3 aluminium alloy used as aircraft fuselage skin," *Mater. Res.*, vol. 22, no. 2, pp. 1–8, 2019, doi: 10.1590/1980-5373-MR-2018-0280.

[164] H. Bo, Y. Kyoung, J. Hui, I. Song, T. Sung, and M. Ho, "Surface modification of anodized Mg in ammonium hydrogen fluoride by various voltages," *Surf. Coat. Technol.*, vol. 259, no. November, pp. 310–317, 2014, doi: 10.1016/j.surfcoat.2014.03.032.

[165] I. Epelboin, C. Gabrielli, M. Keddam, and H. Takenouti, "A model of the anodic behaviour of iron in sulphuric acid medium," *Electrochim. Acta*, vol. 20, no. 11, pp. 913–916, 1975, doi: 10.1016/0013-4686(75)87017-4.

[166] I. Epelboin, M. Keddam, O. R. Mattos, and H. Takenouti, "The dissolution and passivation of Fe and Fe-Cr alloys in acidified sulphate medium: influences of pH and Cr content," *Corros. Sci.*, vol. 19, pp. 1105–1112, 1979.

[167] J. H. . W. de Dobbelaar, J. A. L.; Wit, "Impedance measurements and analysis of the corrosion of chromium," *J. Electrochem. Soc.*, vol. 137, no. 7, pp. 2038–2046, 1990, doi: 10.1149/1.2086861.

[168] C. Cachet, F. Ganne, G. Maurin, J. Petitjean, V. Vivier, and R. Wiart, "EIS investigation of zinc dissolution in aerated sulfate medium. Part I: bulk zinc," *Electrochim. Acta*, vol. 47, pp. 509–518, 2001.

[169] C. Cachet *et al.*, "EIS investigation of zinc dissolution in aerated sulphate medium. Part II: zinc coatings," *Electrochim. Acta*, vol. 47, pp. 3409–3422, 2002.

[170] D. Klotz, "Negative capacitance or inductive loop? A general assessment of a common low frequency impedance feature," *Electrochem. commun.*, vol. 98, pp. 58–62, 2019.

[171] I. Epelboin, M. Keddam, and J. C. Lestrade, "Faradaic impedances and intermediates in electrochemical reactions," *Faraday Discuss. Chem. Soc.*, vol. 56, pp. 264–275, 1973, doi: 10.1039/DC9735600264.

[172] C. D. Taylor, "A first-principles surface reaction kinetic model for hydrogen evolution under cathodic and anodic conditions on magnesium," *J. Electrochem. Soc.*, vol. 163, no. 9, pp. C602–C608, 2016, doi: 10.1149/2.1171609jes.

[173] R. Antaño-López, M. Keddam, M. Turmine, and V. Vivier, "The impedance response of a passive film revisited by a double modulation technique," *ChemElectroChem*, vol. 6, pp. 202–210, 2019, doi: 10.1002/celc.201800737.

[174] J. O. M. Bockris, D. Drazic, and A. R. Despic, "The electrode kinetics of the deposition and dissolution of iron," *Electrochim. Acta*, vol. 4, pp. 325–361, 1961.

[175] W. J. Lorenz and J. R. Vilche, "Zur kinetik der anodischen eisenauflosung im neutralen medium," *Corros. Sci.*, vol. 12, pp. 785–798, 1972.

[176] K. E. Heusler and R. Knödler, "Die kinetik der zinkelektrode in wassrigen malo natlosungen," *Electrochim. Acta*, vol. 18, pp. 855–861, 1973.

[177] M. E. Orazem, N. Pébère, and B. Tribollet, "Enhanced graphical representation of electrochemical impedance data," *J. Electrochem. Soc.*, vol. 153, no. 4, pp. B129–B136, 2006, doi: 10.1149/1.2168377.

[178] B. Hirschorn, M. E. Orazem, B. Tribollet, V. Vivier, I. Frateur, and M. Musiani, “Constant-Phase-Element behavior caused by resistivity distributions in films. I: theory,” *J. Electrochem. Soc.*, vol. 157, no. 12, pp. C452–C457, 2010, doi: 10.1149/1.3499564.

[179] B. Hirschorn, M. E. Orazem, B. Tribollet, V. Vivier, I. Frateur, and M. Musiani, “Constant-Phase-Element behavior caused by resistivity distributions in films. II: applications,” *J. Electrochem. Soc.*, vol. 157, no. 12, pp. C458–C463, 2010, doi: 10.1149/1.3499565.

[180] A. K. Jonscher, “Dielectric characterisation of semiconductors,” *Solid State Electron.*, vol. 33, no. 6, pp. 737–742, 1990, doi: 10.1016/0038-1101(90)90187-J.

[181] N. Damak, A. Kallel, and Z. Fakhfakh, “Space charge characterization of MgO by coupling cavity resonator and mirror method,” *Ann. Chim. Sci. Mat.*, vol. 23, no. 1–2, pp. 255–258, 1998, doi: doi.org/10.1016/S0151-9107(98)80068-8.

[182] F. Cao, G. L. Song, and A. Atrens, “Corrosion and passivation of magnesium alloys,” *Corros. Sci.*, vol. 111, pp. 835–845, 2016, doi: 10.1016/j.corsci.2016.05.041.

[183] S. Leleu, B. Rives, N. Causse, and N. Pébère, “Corrosion rate determination of rare-earth Mg alloys in a Na_2SO_4 solution by electrochemical measurements and inductive coupled plasma-optical emission spectroscopy,” *J. Magnes. Alloy.*, vol. 7, pp. 47–57, 2019, doi: 10.1016/j.jma.2018.12.002.